Doctoral Dissertation

Crystallographic Analysis on Initiation of Intergranular Stress Corrosion Cracking of Alloy 600 in Simulated PWR Primary Water Environment

**(模擬 PWR 1 次冷却水環境における Alloy600 の
粒界応力腐食割れ発生の結晶学的検討)**

Ki-Taek Jung

鄭　起宅

September 2022

Division of Materials and Manufacturing Science

Graduate School of Engineering,

Osaka University

Contents

Chapter 1 General introduction

1.1 Ni based alloy

Ni based alloys are widely used in various fields such as aircraft gas turbines[1,2], steam turbine power plants[3-5], nuclear power systems[6-10] and chemical and petrochemical plants[11-13] due to their excellent strength and corrosion resistance at elevated temperatures[14-16]. Ni based alloys are classified into Ni-Cr alloy (Inconel), Ni-Cu alloy (Monel), Ni-Mo alloy (Hastelloy) and Ni-Cr-Fe alloy (Incoloy) depending on alloying constituents[17]. Among the alloys, Ni-Cr alloys possess superior oxidation and corrosion resistance[18]. The chemical composition of some Ni-Cr alloys is listed in **Table 1-1**. In general, Cr addition to Ni increases corrosion resistance, which is attributed to the formation of highly protective films as Cr_2O_3 and/or $NiCr_2O_4$ on Ni-Cr alloys. However, it has been reported that stress corrosion cracking (SCC) occurred in high temperature and high pressure water environments although Ni-Cr alloys exhibit excellent corrosion resistance at elevated temperatures[7, 19, 20]. SCC has been found particularly on Alloy 600 that was used as structural materials and steam generator tubes of commercial pressurized water reactors (PWRs) in nuclear power system[7, 19-25]. **Figure 1-1** presents an example of the primary water stress corrosion cracking (PWSCC) on Alloy 600 at a part of steam generator tubes reported by Hwang[26]. As this is strongly related to the safe operation of PWRs, SCC on Alloy 600 has been recognized as an urgent problem to be solved in the field of nuclear industries. Alloy 600 has been replaced by Alloy 690 that contains more Cr to improve corrosion resistance, but PWSCC appeared also on the alloy[27-31]. Although extensive studies have been performed, PWSCC mechanism still remains unclear.

Table 1-1 Chemical composition of Ni-Cr alloys

Alloy	Elements														
	Ni	**Cr**	**Fe**	**Mo**	**Nb**	**Co**	**Mn**	**Cu**	**Al**	**Ti**	**Si**	**C**	**S**	**P**	**B**
600	72.0	14.0-17.0	6.0-10.0	-	-	-	1.0	0.5	-	-	0.5	0.15	0.015	-	-
617	44.2-56.0	20.0-24.0	3.0	8.0-10.0	-	10.0-15.0	0.5	0.5	0.8-1.5	0.6	0.5	0.15	0.015	0.015	0.006
625	58.0	20.0-23.0	5.0	8.0-10.0	3.15-4.15	1.0	0.5	-	0.4	0.4	0.5	0.1	0.015	0.015	-
690	59.5	30	9.2	-	-	-	0.35	0.01	0.02	-	0.35	0.019	0.03	-	-
718	50.0-55.0	17.0-21.0	bal.	2.8-3.3	4.75-5.5	1.0	0.35	0.2-0.8	0.65-1.15	0.3	0.35	0.08	0.015	0.015	0.006

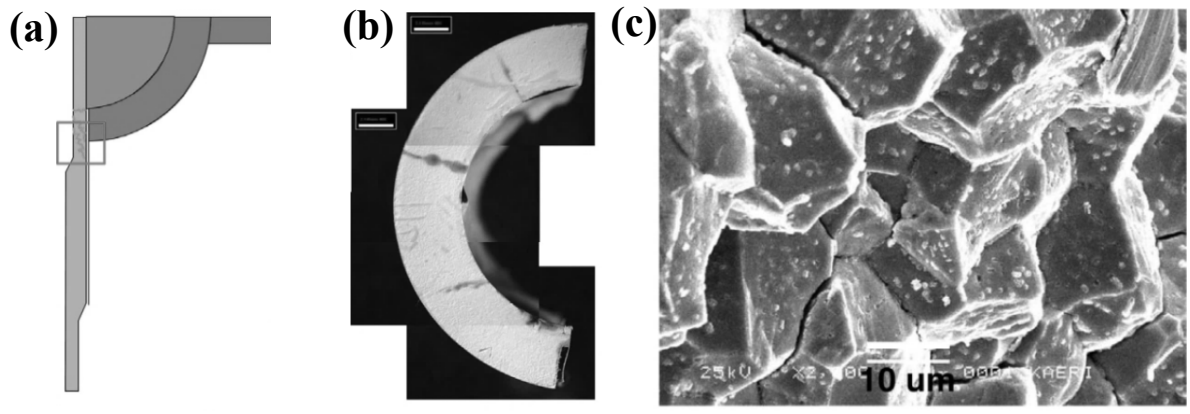

Fig. 1-1 (a) Crack location on the drain nozzle, (b) top view of the through wall crack confirmed by dye penetrant test, (c) PWSCC fracture surface[26].

1.2 Intergranular Stress Corrosion Cracking (IGSCC)

It is well-known that SCC is caused by the superimposed effects of susceptible material, stress and corrosive environment as shown in **Fig. 1-2**. SCC are generally characterized into two types; intergranular stress corrosion cracking (IGSCC) and

transgranular stress corrosion cracking (TGSCC). Among these two types of SCC, the IGSCC on Alloy 600 has been experienced in PWR primary water environments. On the other hand, experimental observation of IGSCC on Alloy 600 was for the first time reported by Coriou et al[32, 33].

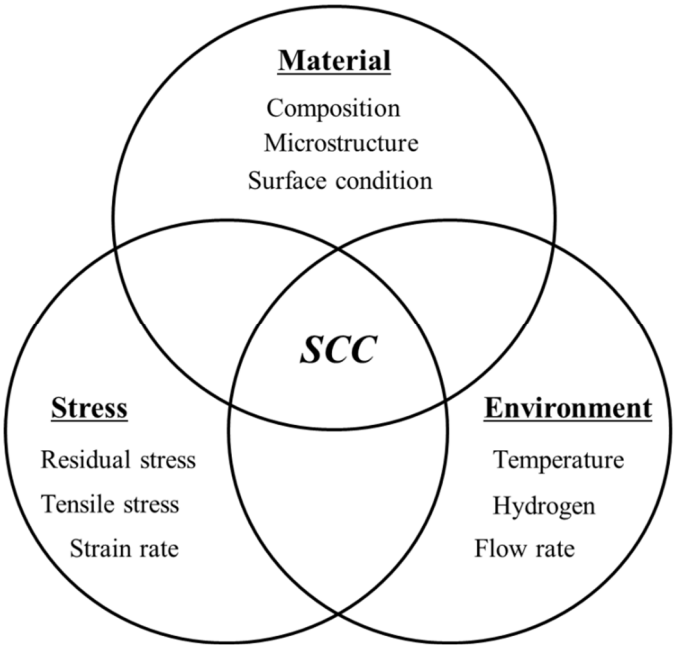

Fig. 1-2 Influencing factors of stress corrosion cracking.

Figures 1-3 (a) and **(b)** show cross-sectional SEM images of Alloy 600 specimens immersed in pure water at 350 ºC for 5 months, then exposed to steam at 650 ºC for 4 months under constant stress of 8.5 kg / mm^2. As apparent from the images, a lot of fine cracks initiated and propagated at grain boundaries. Coriou et al. discussed that IGSCC was influenced by temperature, stress and the microstructure of the alloy. Since the first report of IGSCC on Alloy 600 by Coriou et al., this phenomenon has been experienced in commercialized PWRs.

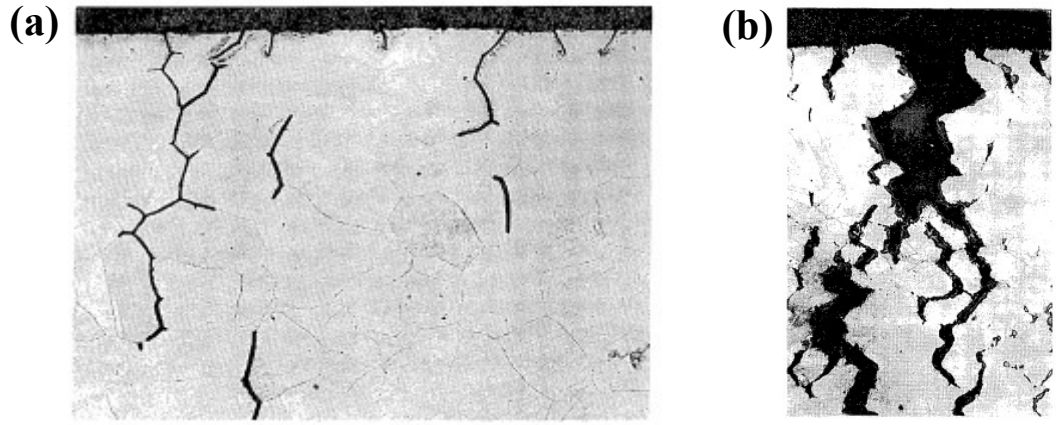

Fig. 1-3 (a) Intergranular cracking of an Inconel – type alloy (ARC 7915) after a 5 – month stress – test in water at 350 ˚C and (b) intergranular cracking of Inconel 600 – type alloy after 4 – month test under constant stress of 8, 5 kg/ mm^2 in steam at 650 ˚C[33].

SCC has been discussed in terms of the crack initiation stage and the subsequent crack propagation stage as shown in **Fig. 1-4**. Cracks grow slowly up to a depth of approximately 500 μm in the crack initiation stage, then grow at relatively fast rates in the propagation stage. So far studies have focused on the crack propagation rather than the initiation although the initiation stage accounts for most of the expected life time until failure due to the relatively fast growth rate of cracks in the propagation stage.

Many models have been reported to explain the mechanism and process of the crack propagation. On the other hand, models for the crack initiation are quite limited. This is because the mechanism of crack initiation is not clear and also it is difficult to analyze crack initiation as compared with crack propagation process. In the following subsections, the major three models of IGSCC is summarized; slip dissolution, internal oxidation and hydrogen embrittlement.

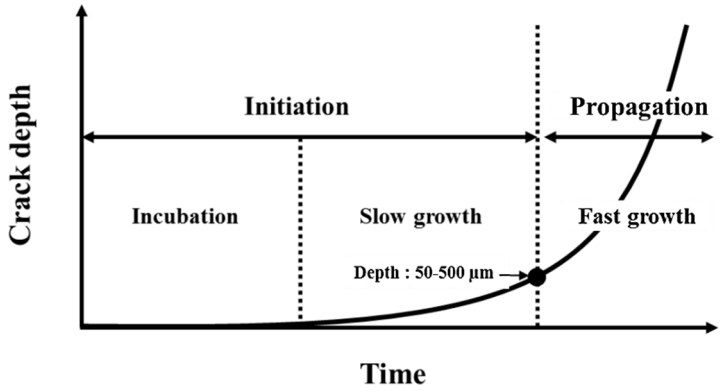

Fig. 1-4 Crack initiation and propagation stages of stress corrosion cracking.

1.2.1 Slip dissolution

Figure 1-5 shows a typical SEM image of a IGSCC crack formed by slip dissolution[34]. In the model, crack is considered to grow at a grain boundary as a consequence of a competition between the dissolution of substrate metal and the repassivation of the metal. The breakdown of passive film is occurred at grain boundary by slip step induced by an applied stress. A crack initiates due to the local dissolution at grain boundary. The slip dissolution model has been studied for years since Mears et al. proposed[35] and Parkins experimentally demonstrated[36]. At present, the model proposed by Andresen and Ford is widely applied to consider the process of commercialized reactors[37]. The slip dissolution model was originally proposed to understand the mechanism of TGSCC. However, it is reported that grain boundary deformation inducing the IGSCC is possible to occur as the dislocation mobility has an influence on the IGSCC[38]. Paraventi has investigated the effect of hydrogen on dislocation motion in the grain boundaries[39]. As a result, it is demonstrated that the introduction of hydrogen leads to decomposition of dislocation pile. The decomposed dislocation might be adsorbed to the grain boundaries or grain boundary deformation. Therefore, it is important to comprehensively understand the

slip dissolution model for the mechanism of IGSCC.

Figure 1-6 explains that the propagation of crack was governed by the 2nd Faraday's Law that is applied to oxidation reactions such as dissolution and repassivaiton at a crack tip when a protective surface oxide film was broken by the increasing deformation of the metal substrate in the model of Andresen and Ford. This rupture was assumed to occur with a certain periodicity, t_f, which was calculated from the rupture strain of the oxide film and the strain rate at the crack tip.

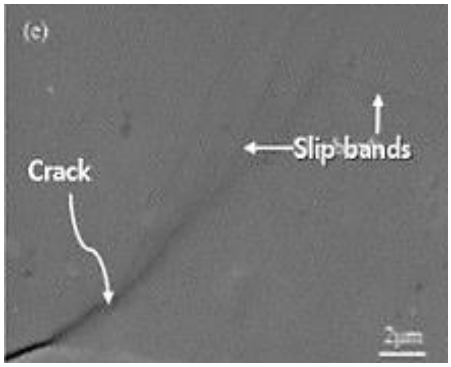

Fig. 1-5 (a) SEM image of IGSCC by slip dissolution[34].

Furthermore, it was also considered that after each period of t_f, the repassivation process occurred. This behavior was found to vary in a complex manner depending on environment as well as materials chemistry. The time dependence of oxidation charge was expressed as following;

$$\left(\frac{da}{dt}\right)_{scc} = f(n)\left(\frac{d\varepsilon}{dt}\right)_{ct}^{n} \tag{1-1}$$

where $(da/dt)_{scc}$ was the crack growth rate and $(d\varepsilon/dt)_{ct}$ was the strain rate at crack tip. In addition, $f(n)$ was a function regarding environmental and material factors that assisted the crack growth and was formulated as the equation (1-2).

$$f(n) = \left(\frac{M}{z\rho F}\right) i(n)dt \tag{1-2}$$

in the equation, M, z, ρ and F were expressed as the atomic weight of the metal, the valence state, density and Faraday's constant. The repassivation current density of $i(n)$ was supposed to decay exponentially with time, t. However, Hall presented the following criticism for this model[40-42]. For examples, some doubts existed about the role of creep in the crack growth rate and the discussion focused mainly on the fracture mechanics. Furthermore, the lack of formalization in the mechano-chemical roles, insufficient understanding on electrochemical behavior at crack tip and a mathematical fault in the formula of the model were also pointed out. Hau and Rebak were also doubtful of the slip dissolution and film rupture in Andresen and Ford's model, especially the effect of Cr depletion on IGSCC of Alloy 600 in the high temperature and high pressure water environment of primary side of PWR[43]. As mentioned above, there are various approaches to explain the slip dissolution model. Recently alternative theoretical modeling has been carried out to improve this model related to slip dissolution.

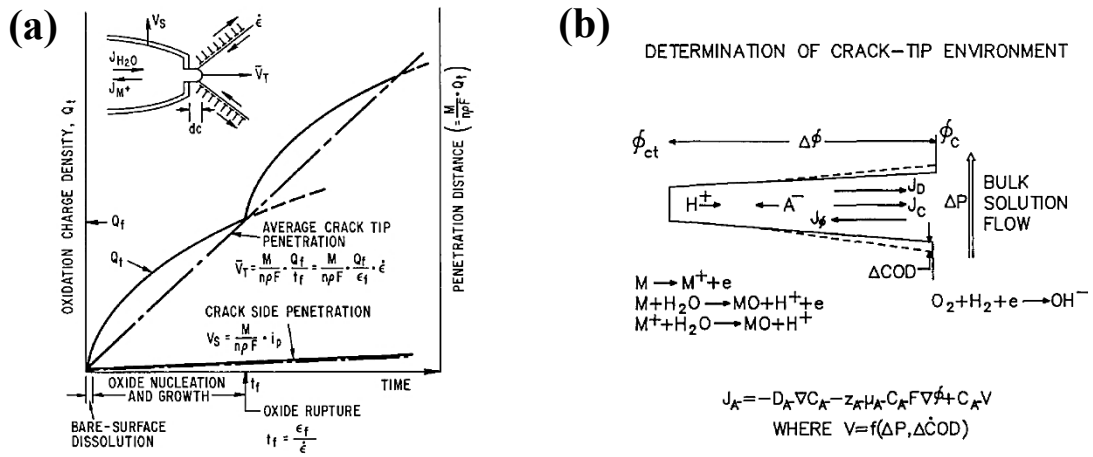

Fig. 1-6 (a) Schematic oxidation charge density vs time relationships for a strained crack tip and the unstrained crack sides and (b) schematic diagram of mass transport and thermodynamic criteria which govern the crack tip environment[37].

IGSCC proceeds by the repeated process of film rupture, dissolution and repassivation in the slip dissolution model. Therefore, it is important to decrease the rate of the crack initiation and propagation by increasing the repassivation rate. Kwon et al. investigated the relationship between repassivation kinetics and SCC susceptibility, and proposed a new approach to predict SCC susceptibility in terms of repassivation kinetics[44]. **Figure 1-7(a)** shows log$I(t)$ vs. $1/q(t)$ plots obtained by scratching the surface of type 304 stainless steel polarized at -200 mV in deaerated 4M NaCl. In the figure, I(t) presents anodic current generated during the scratch test while q(t) is charge that flowed during the repassivation. Schematic log$I(t)$ vs. $1/q(t)$ in **Fig. 1-7(b)** explains the correlation between the slop of the log$I(t)$ vs. $1/q(t)$ plot, *cBV* and the SCC susceptibility. As the value of *cBV* increases, the repassivation rate becomes low and the resulting probability of SCC initiation increases. From **Fig. 1-7(a)**, it is found that type 304 stainless steel exhibited higher resistance in 0.2M and 0.02M NaCl solution to SCC due to the lower *cBV* values. On the other hand, the *cBV* value increased with increasing Cl^- concentration. Based on these results, the effect of Cl^- concentration on *cBV* and resulting SCC susceptibility could be predicted in terms of repassivation kinetics.

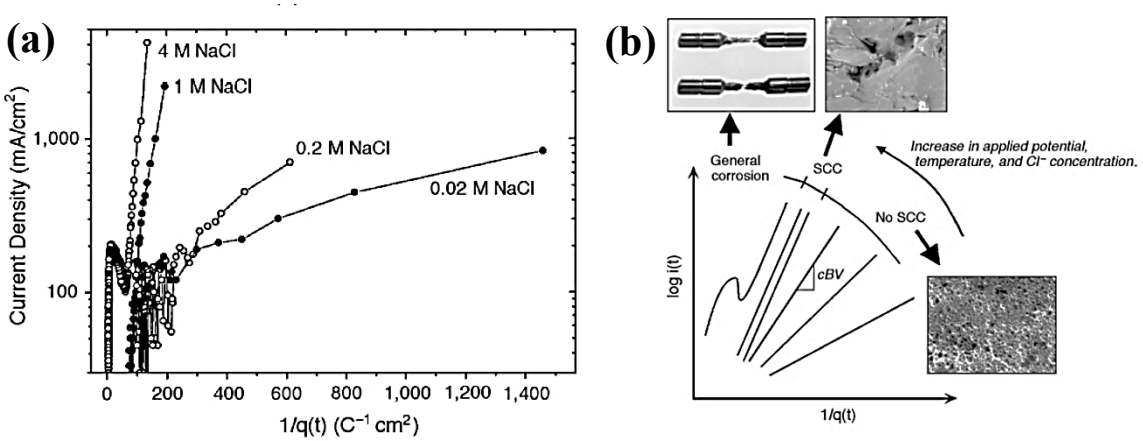

Fig. 1-7 (a) log$I(t)$ vs. $1/q(t)$ plots of type 304 SS polarized at –110 mV in deaerated NaCl solutions at 50 ˚C and (b) schematic log$I(t)$ vs. $1/q(t)$ plots representing the relationship between the change in *cBV* and SCC susceptibility[44].

1.2.2 Internal oxidation

The internal oxidation model was proposed by Scott et al. in 1993 to complement the slip dissolution model[45]. **Figure 1-8** shows a typical STEM-HAADF image of IGSCC caused by the internal oxidation[46]. In the model, oxygen ions are considered to diffuse along weak grain boundary in the vicinity of crack tip and then, the crack propagates due to the continuous diffusion of oxygen ions. It is well-known that the internal oxidation occurs at the temperature range of 500 ~ 1200 ºC, but the intergranular internal oxidation preferentially takes place at 500 ~ 800 ºC[47]. However, the key issue, which is still under discussion, of SCC in PWR environment is whether the internal oxidation occurs at temperature as low as 300 ºC in atmospheres such as water, hydrogen or vapor.

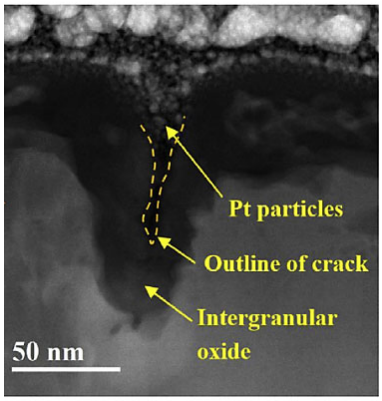

Fig. 1-8 STEM-HAADF image of IGSCC by internal oxidation[46].

Gendron et al. conducted an experimental study of the internal oxidation by using secondary ion mass spectrometry (SIMS) and analytical transmission electron microscopy (ATEM) to demonstrate hypotheses related to the IGSCC initiation on Alloy 600 under water or vapor at the temperature of 300 ~ 400 ºC[48]. **Figure 1-9** shows TEM images of a IGSCC crack tip on Alloy 600 formed in PWR primary environment (1200 ppm B as H_3BO_3, 2 ppm Li as LiOH and 25-35 ml H_2). Schematic illustrations of cross-sectional ATEM observations of IG penetration as well as IGSCC crack tip are presented in **Fig. 1-10**. The results revealed that a narrow porous region with the width of 2 nm was formed at the crack tip. Furthermore, the diffraction pattern shown in **Fig. 1-9(b)** indicated the formation of a thin film of polycrystalline, Cr- and Fe-rich oxides with NiO on the SCC crack walls in the vicinity of the crack tip. These evidenced the internal oxidation model.

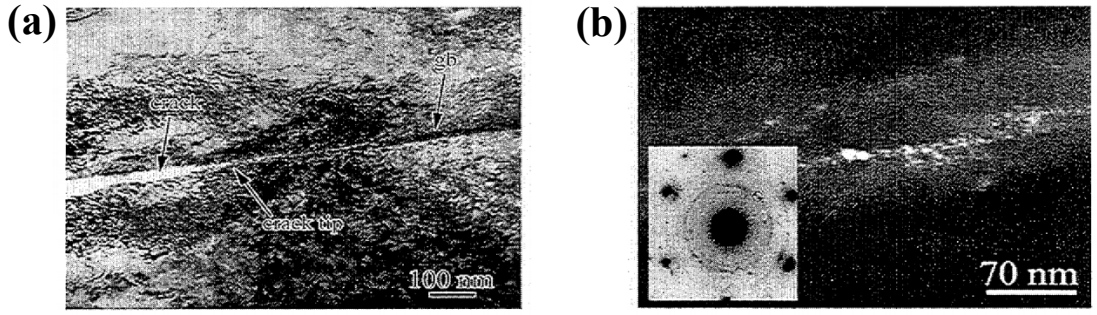

Fig. 1-9 (a) Bright-field TEM image of a sharp IGSCC crack tip in Alloy 600 and (b) Dark-field TEM image of the grain boundary region ahead of the crack tip shown in (a)[48].

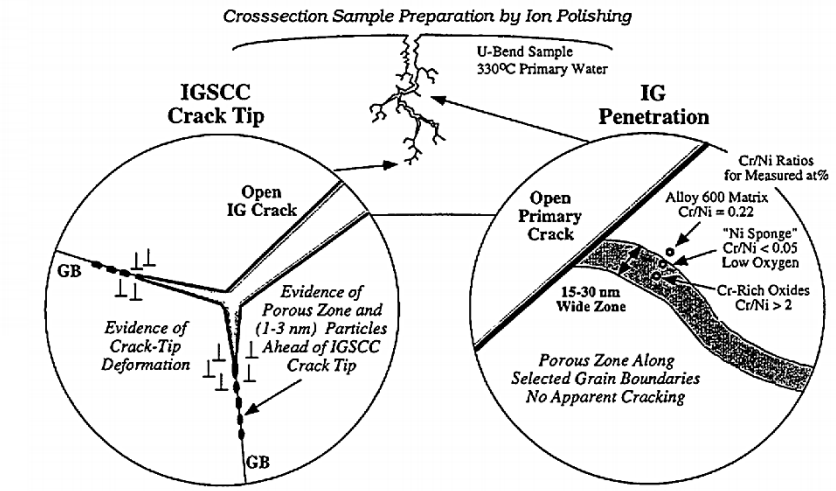

Fig. 1-10 Schematic illustration of cross-sectional ATEM observations of intergranular penetration and IGSCC crack tip regions in an Alloy 600 after U-bend testing in primary water at temperature of 330 °C[48].

Persaud et al. evaluated the PWSCC susceptibility based on the internal oxidation model[49]. In this work, solution annealed and thermally treated Alloy 600 specimens were exposed to simulated PWR primary water. **Figure 1-11** shows STEM-HAADF image taken at a grain boundary of the thermally treated Alloy 600 and corresponding EDS elemental

maps. After the exposure test, Fe- and Cr-rich oxides were observed at the top surface of the specimen. The internal oxidation propagated into the inside of specimen up to approximately 700 nm. The authors mentioned that the heat treatment of Alloy 600 prevented the progress of the internal oxidation because Cr was concentrated at the oxidized grain boundaries.

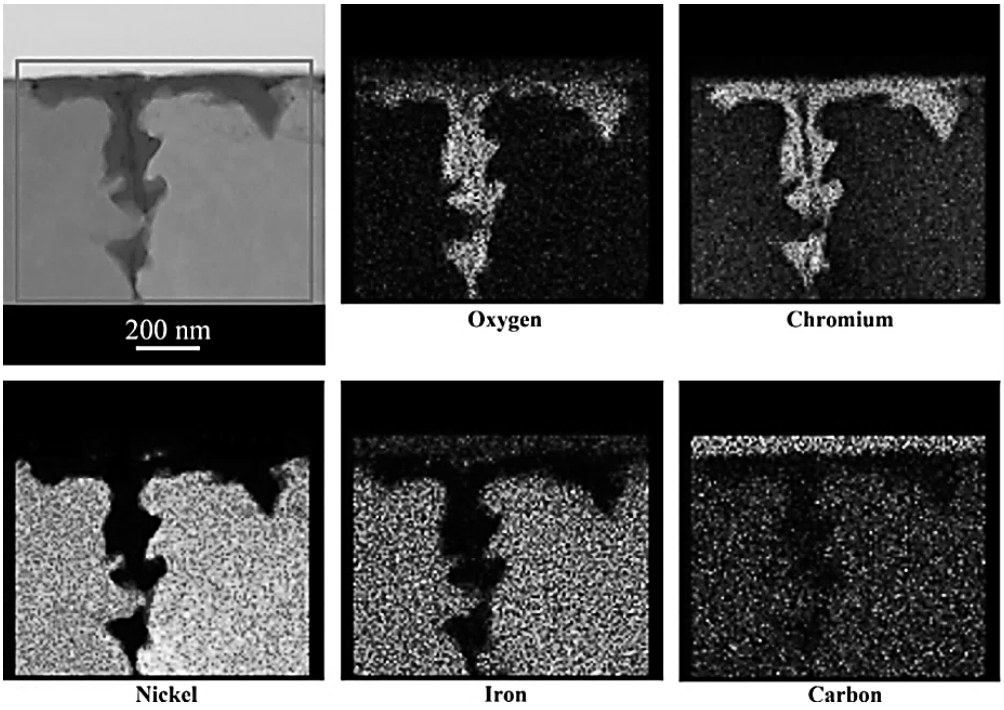

Fig.1-11 STEM-HAADF and EDS elemental map taken along a grain boundary of the Alloy 600TT FIB at cross-section[49].

1.2.3 Hydrogen embrittlement

As mentioned above, there are major three models for stress corrosion cracking. In the previous subsections, the slip dissolution model and the internal oxidation model were focused. In the present subsection, the hydrogen embrittlement model is summarized and discussed. **Figure 1-12** shows an SEM image of a crack that was presented as an example in the hydrogen embrittlement model[50]. Hydrogen embrittlement is a phenomenon where

hydrogen present in metallic materials causes the degradation of the mechanical properties, such as strength, ductility and toughness. It is well-known that hydrogens generated in the vicinity of a crack of a metallic material and/or ones present in the material diffuse to the crack tip, leading to its degradation[50-55]. Hydrogens diffusion causes further propagation of the crack, accompanied with the local stress concentration at the crack tip. Extensive studies have revealed that the hydrogen diffusion occurs in loading stress and the hydrogen transfer takes place at dislocations during plastic deformation in Ni based alloys[56-60]. The hydrogen transfer leads to the local enrichment of hydrogen which causes crack.

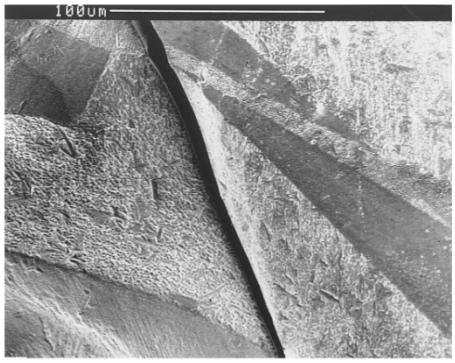

Fig. 1-12 SEM image of crack by hydrogen embrittlement[50].

Fournier et al. examined the susceptibility of hydrogen embrittlement on Alloy 718 at room temperature[60]. They suggested that hydrogen embrittlement occurred due to strong hydrogen-deformation interactions, based on observations of the fracture surfaces of hydrogen embrittled specimens. On the other hand, Lynch reported that the atomic bonds were weakened by hydrogen adsorbed on cracks and the adsorption affected the nucleation of dislocations at crack tips[61]. **Figure 1-13** presents schematic illustration of the hydrogen embrittlement model proposed by Lynch. The model reported that hydrogen atoms between atomic layers weakened interatomic bonds and as a result facilitated the shear movement of atoms, that is, the nucleation of dislocation, at crack tips. The injection of

dislocations from the crack tip first on plane D1 and then on plane D2 caused the crack propagation into the material as shown in **Fig. 1-13(b)**. Some activity of dislocations could occur in front of crack, leading to the production of voids. Cracks grew by alternate-slip coalesce with the voids that were formed along the crack extension line. In addition to the hydrogen accumulation model proposed by Beachem[62], the localized plastic deformation and hydrogen induction model were reported by Onyewuenyi and Hirth[63]. However, no consensus on how hydrogen contributes to the hydrogen embrittlement has been obtained so far.

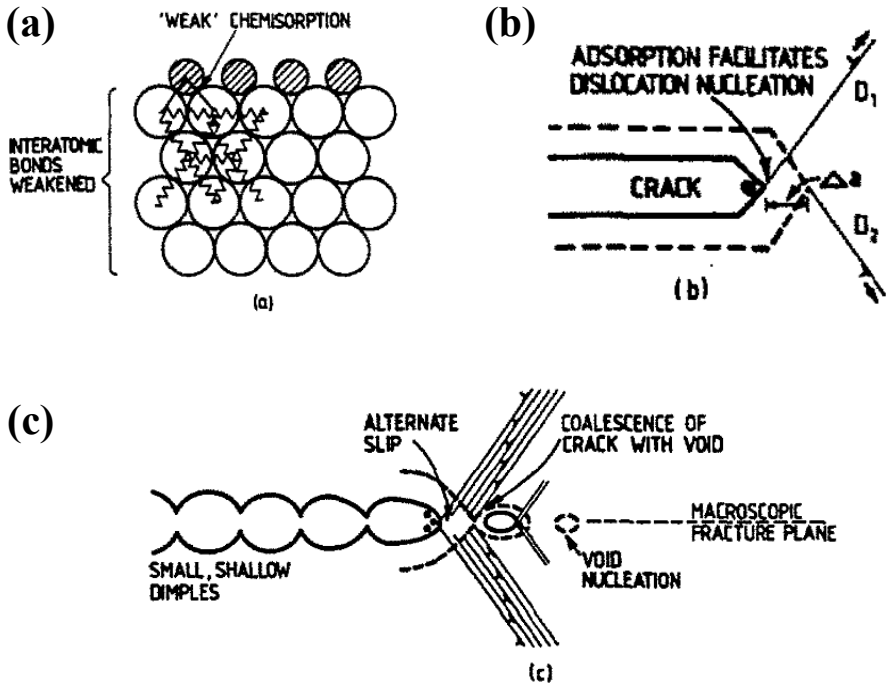

Fig. 1-13 Schematic illustration the adsorption-induced localized-slip process for environmentally assisted cracking[61].

1.3 Grain boundary characteristics

Among the factors affecting the initiation of IGSCC, grain boundary characteristics are especially important as it has been reported that the crack initiation depends on the characteristics of individual grain boundaries[64-68]. Grain boundaries are categorized as high angle grain boundary (HAGB) or low angle grain boundary (LAGB) according to the extent of misorientaion between adjacent grains. In general, HAGB is defined as the grain boundary whose misorientation is greater than 15º while LAGB is the grain boundary with a misorientation less than 15º. HAGB is further categorized as random boundary or coincidence site lattice (CSL) boundary. The concept of CSL boundary was introduced by Kronberg and Wilson in 1949[69]. On CSL boundary, the lattices of adjacent grains are coincidence with a certain range of rotation axis/angle. The fraction of atoms in coincidence at a CSL boundary is generally known as the density of coincidence sites. The reciprocal densities are more common as a parameter to describe a CSL boundary, designated by Σ. For an example, the twin boundary with the misorientaion angle of 60º is categorized as a CSL boundary and its Σ value is 3. On the other hand, random boundary is defined as disordered boundary where the lattice coincidence is lower. IGSCC resistance increases with increasing the lattice coincidence of adjacent grains. Therefore, it is well-known that IGSCC mainly occurs at random boundary rather than at CSL boundary[70].

Crawford and Was investigated the role of grain boundary misorientation in intergranular of Alloy 600 at the temperature of 360 ºC in Ar and high purity water environment[71]. The number of characterized boundaries as well as that of cracked boundaries on annealed and coincidence site lattice boundary (CSLB)-enhanced specimens after constant extension rate tensile test are summarized in **Table 1-2**. Obtained results indicated that the IGSCC initiation on Alloy 600 was affected by misorientation angle, that

is, CSL boundaries were more resistant against cracking than random boundaries in both Ar and high purity water environment. Furthermore, their work demonstrated that the crack initiation on Alloy 600 can be reduced by increasing the proportion of coincident boundaries. In other words, the initiation of IGSCC can be controlled by optimizations of grain boundary characteristics. Therefore, grain boundary engineering (GBE) has attracted attention for improvements of IGSCC resistance.

Table 1-2 Numbers of characterized and cracked boundaries of annealed and CSLB-enhanced specimen tested in high-purity water and Argon[71)]

	High-Purity Water				Argon			
	Number of Type	Pct of Total*	Number Cracked	Pct of Type**	Number of Type	Pct of Total*	Number Cracked	Pct of Type**
				Annealed Samples				
CSLBs	119	18	8	6.7	67	13	1	1.5
LABs	29	4	0	0	35	7	0	0
GHABs	526	78	49	9.3	396	80	26	6.6
Total	674	—	57	8.5	498	—	27	5.4
				CSLB-Enhanced Samples				
CSLBs	228	37	4	1.8	119	33	2	1.7
LABs	33	5	0	0	22	6	0	0
GHABs	356	58	19	5.3	225	61	1	0.4
Total	617	—	23	3.7	366	—	3	0.8

*Percentage of total characterized boundaries.
**Percentage of boundary type that is cracked.

Since the concept of grain boundary design and control was introduced by Watanabe in 1984, GBE has been successfully applied for various materials to improve their strength, ductility and IGSCC resistance[19, 73, 74)], and has been realized by annealing[75, 76)], unidirectional solidification[77)] and thermo-mechanical treatment[65-68, 72)]. Among these approaches, the thermo-mechanical treatment is well-known to be an effective and economical approach. Therefore, treatment has been extensively attempted. Tan et al. reported that GBE contributed to improved strength, creep strength as well as superior resistance to stress corrosion cracking and oxidation of austenitic stainless steel and Ni-based alloy that are used as structural materials of nuclear reactors[74)]. Bi et al. analyzed

grain boundaries of thermo-mechanically treated type 304 stainless steel by an analytical transmission electron microscope. **Figure 1-14** shows SEM image of an example of twin emission from a random boundary in the thermo-mechanically treated stainless steel and corresponding grain boundary map obtained by orientation imaging microscopy. The authors indicated that the twin emission segment was transformed from a random boundary to a Σ17a CSL boundary. After the sensitization and etching of the thermo-mechanically treated steel, only random boundaries were deeply grooved as shown in **Fig. 1-14(a)**. They concluded that low energy boundary segment suppressed chromium carbide precipitation and subsequent chromium depletion along the segment, based on TEM study of the steel. This resulted in the higher resistance against intergranular corrosion at lower energy grain boundaries of Σ17a and Σ3.

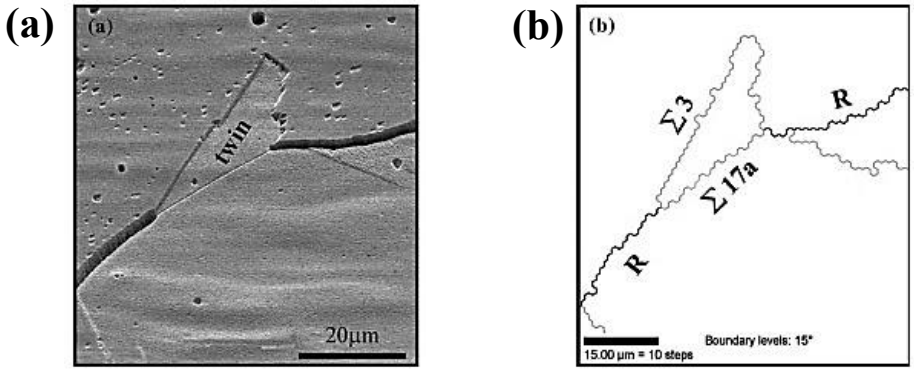

Fig. 1-14 SEM micrograph (a) showing an example of twin emission from a random grain boundary and an OIM image map (b) showing a twin-emitted segment transformed from the random boundary structure (R) to a low-energy Σ 17a CSL boundary structure in the thermomechanical treated specimen after sensitization[78)].

1.4 Analytical techniques of IGSCC

The various analytical techniques such as electron backscatter diffraction (EBSD)[79, 80], X-ray diffraction (XRD)[81,83], scanning electron microscope (SEM)[84-86], transmission electron microscope (TEM)[46, 78], Auger electron spectroscopy (AES)[87], energy dispersive spectroscopy (EDS)[88] and secondary ion mass spectroscopy (SIMS)[89, 90] have been utilized for materials characterization. As the analysis of microstructure and crystallographic characterization of specimens are very important for the understanding of IGSCC, such studies were performed by using an optical microscope and a TEM. Observations using an optical microscope provide information on grain size and grain distribution in a wide area. However, it is difficult to analyze the surface of materials on sub-micrometer scale due to the resolution of the system and in addition, no crystallographic information can be obtained. On the other hand, TEM can observe grains with a resolution of 1 nm as well as analyze the crystal orientation of grains and grain boundary characteristics with the accuracy of 0.1º or less. However, Parkins and Shibata reported that crack initiation and propagation can be stochastically marshaled[91, 92], that is, cracks of IGSCC do not initiate simultaneously and cracks do not necessarily initiate at all grain boundaries. Therefore, a sufficient number of grains should be analyzed to perform reliable analysis of IGSCC[93]. For this purpose, TEM is not suitable for statistical analysis of crystallographic features of IGSCC because it takes extremely long time to acquire enough data due to the limitation of its analyzed area.

EBSD also provides crystallographic information of crystalline materials and can target a wide range of material surface, different from TEM. In EBSD, crystallographic analysis is carried out based on Kikuchi patterns of backscattered electrons. Recently, this technique has been used to examine the stress corrosion cracking of Alloy 600 in high-temperature water. Young et al. showed the grain boundary map, Euler angle image

and misorientation map around an SCC crack generated on Alloy 600 in hydrogen deaerated water at 360 ºC[94]. Hou also presented the grain boundary map and kernel average misorientation map near an SCC crack on Alloy 600 exposed to a corrosive aqueous solution containing sodium hydroxide and lead oxide at 330 ºC and explained that the high dislocation density and strain concentration induced by cold work promoted the crack propagation[95]. Both works focused on crack propagation rather than crack initiation. Although the initiation stage accounts for most of the expected life time as described in the section 1.2, the crack initiation has not been crystallographically examined.

1.5 The purpose and structure of this thesis

In the present work, the author crystallographically examined the initiation of IGSCC on Alloy 600 in simulated PWR primary water environments. The present thesis consists of the following 5 chapters.

Chapter 1 gives the background and purpose of this work.

Chapter 2 provides an approach to facilitate IGSCC initiation of Alloy 600 during SSRT in a simulated PWR environment. Furthermore, an EBSD-based methodology to examine grain boundary planes on cracked grain boundaries is suggested.

Chapter 3 shows effects of the cold work ratio of Alloy 600 specimen and the dissolved hydrogen concentration on the IGSCC initiation. The IGSCC initiation is discussed in terms of misorientation angle, kernel average misorientation and stress loaded on grain boundary during SSRT.

Chapter 4 presents the three-dimensional characterization of IGSCC crack by EBSD measurements. Cracks are characterized from top-view as well as from the side-view enabling the three-dimensional characterization.

Chapter 5 summarizes the findings of this thesis.

References

1) D. Furrer, H. Fecht, Jom. 51 (1999) 14–17.

2) P. Caron, T. Khan, Aerosp. Sci. Technol. 3 (1999) 513–523.

3) I. Choudhury, M.J. El-Baradie, Mater. Process. Technol. 77 (1998) 278–284.

4) J. Rösler, M. Götting, D. Del Genovese, B. Böttger, R. Kopp, M. Wolske, F. Schubert, H.-J. Penkalla, T. Seliga, A. Thoma, A. Scholz, C. Berger, Adv. Eng. Mater. 5 (2003) 469–483.

5) R.W. Swindeman, M.J. Swindeman, Int. J. Press. Vessel. Pip. 85 (2008) 72–79.

6) L. Tan, X. Ren, K. Sridharan, T.R. Allen, Corros. Sci. 50 (2008) 3056–3062.

7) M. Sennour, L. Marchetti, F. Martin, S. Perrin, R. Molins, M.J. Pijolat, Nucl. Mater. 402 (2010) 147–156.

8) P. Yvon, F.J. Carré, Nucl. Mater. 385 (2009) 217–222.

9) D.B. Mitton, J.H. Yoon, J.A. Cline, H.S. Kim, N. Eliaz, R.M. Latanision, Ind. Eng. Chem. Res. 39 (2000) 4689–4696.

10) K. Ehrlich, J. Konys, L.J. Heikinheimo, Nucl. Mater. 327 (2004) 140–147.

11) D.J. Tillack, J.E. Guthrie, Nickel Dev. Inst. (1998) 1–16.

12) Y. Wang, W. Chen, Surf. Coatings Technol. 183 (2004) 18–28.

13) Z. Zeng, K. Natesan, Int. J. Hydrogen Energy. 32 (2007) 3640–3647.

14) A. Kawashima, H. Habazaki, K. Hashimoto, Mater. Sci. Eng. A 304 (2001) 753–757.

15) G. Lu, G. Zangari, Electrochim. Acta. 47 (2002) 2969–2979.

16) E.G. Richards, R.M. Cook, Proceedings of the International Symposium on Structural Stability in Superalloys. (1968) 1–24.

17) E.O. Ezugwu, Z.M. Wang, A.R. Machado, J. Mater. Process. Technol. 86 (1999) 1–16.

18) G.C. Wood, I.G. Wright, T. Hodgkiess, D.P. Whittle, Mater. Corros. 21 (1970)

900–910.

19) V.Y. Gertsman, S.M. Bruemmer, Acta Mater. 49 (2001) 1589–1598.

20) L. Marchetti, S. Perrin, Y. Wouters, F. Martin, M. Pijolat, Electrochim. Acta. 55 (2010) 5384–5392.

21) I.G. Park, Nucl. Eng. Des. 212 (2002) 395–399.

22) V.N. Shah, D.B. Lowenstein, A.P.L. Turner, S.R. Ward, J.A. Gorman, P.E. MacDonald, G.H. Weidenhamer, Nucl. Eng. Des. 134 (1992) 199–215.

23) Y.S. Lim, H.P. Kim, S.S. Hwang, J. Nucl. Mater. 440 (2013) 46–54.

24) J. Panter, B. Viguier, J.M. Cloué, M. Foucault, P. Combrade, E.J. Andrieu, Nucl. Mater. 348 (2006) 213–221.

25) R.B. Rebak, Z. Szklarska-Smialowska, Corros. Sci. 38 (1996) 971–988.

26) S.S. Hwang, J. Nucl. Mater. 443 (2013) 321–330.

27) J.D. Hong, J. Lee, C. Jang, T.S. Kim, Mater. Sci. Eng. A 611 (2014) 37–44.

28) J. Xiao, S.Y. Qiu, Y. Chen, Z.H. Fu, Z.X. Lin, Q. Xu, J. Nucl. Mater. 456 (2015) 120–124.

29) B.A. Young, X. Gao, T.S. Srivatsan, P.J. King, Mater. Des. 28 (2007) 373–379.

30) B.A. Young, X. Gao, T.S. Srivatsan, P.J. King, Mater. Sci. Eng. A. 416 (2006) 187–191.

31) Z. Lu, J. Chen, T. Shoji, Y. Takeda, S. Yamazaki, J. Nucl. Mater. 465 (2015) 471–481.

32) H. Coriou, L. Grall, Y.S. Vettier, Colloque de Metallurgie Corrosion, Centre d'Etudes Nucleaires de Saclay, North Holland Publishing Co., Amsterdam, Holland, 161 (1959).

33) H. Coriou, L. Grall, C. Mahieu, M. Pelas, Corrosion. 22 (1966) 280–290.

34) L. Zhu, Y. Yan, J. Li, L. Qiao, Z. Li, A.A. Volinsky, Corros. Sci. 100 (2015)

619–626.

35) R.B. Mears, R.H. Brown, E.H. Dix Jr, In Symposium on Stress–Corrosion Cracking of Metals, Am. Soc. Testing and Materials, Inst. Mining Engineers. (1944) 329–323.

36) R.N Parkins, Corros. Sci. 20 (1980) 147–166.

37) P.L. Andresen, F. Peter Ford, Mater. Sci. Eng. 103 (1988) 167–184.

38) B. Alexandreanu, G.S. Was, Corrosion. 59 (2003) 705–720.

39) D.J. Paraventi, T.M. Angeliu, G.S. Was, Corrosion. 58 (2002) 675–686.

40) M.M. Hall, Corros. Sci. 51 (2009) 1103–1106.

41) M.M. Hall, Corros. Sci. 51 (2009) 225–233.

42) M.M. Hall, Corros. Sci. 50 (2008) 2902–2905.

43) F.H. Hua, R.B. Rebak, Environ. Crack. Mater. (2008) 123–141.

44) H.S. Kwon, Corrosion. 56 (2000) 32–40.

45) P.M. Scott, M. Le Calvar. Proceedings of the 12th International Conference on Environmental Degradation of Materials in Nuclear Power System – Water Reactor – (1993) 657–665.

46) W. Kuang, M. Song, G.S. Was, Acta Mater. 151 (2018) 321–333.

47) P.M. Scott, Proceedings of the 9th International Conference on Environmental Degradation of Materials in Nuclear Power System – Water Reactor – (1999) 1–14.

48) T.S. Gendron, P.M. Scott, S.M. Bruemmer, L.E. Thomas. Proceedings of the 3rd International Steam Generator and Heat Exchanger Conference. (1998) 389–406.

49) S.Y. Persaud, A. Korinek, J. Huang, G.A. Botton, R.C. Newman, Corros. Sci. 86 (2014) 108–122.

50) F. Lecoester, J. Chêne, D. Noel, Mater. Sci. Eng. A 262 (1999) 173–183.

51) D. Eliezer, D.G. Chakrapani, C.J. Altstetter, E.N. Pugh, Metall. Trans. A 10 (1979) 935–941.

52) D. Symons, Metall. Mater. Trans. A 28 (1997) 655–663.

53) R.J. Gest. A.R. Troiano, Corrosion. 30 (1974) 274–279.

54) ASM International. ASM Handbook, Hydrogen Embrittlement of Aluminum Alloys, Hydrogen in Metals, (1974).

55) Y. Murakami, T. Kanezaki, Y. Mine, S. Matsuoka, Metall. Mater. Trans. A Phys. Metall. Mater. Sci. A 39 (2008) 1327–1339.

56) J. Chêne, A.M. Brass, Metall. Mater. Trans. A 35 (2004) 457–464.

57) P.D. Hicks, C.J. Altstetter, Metall. Trans. A 21 (1990) 365–372.

58) P.D. Hicks, C.J. Altstetter, Metall. Trans. A 23 (1992) 237–249.

59) L. Liu, C. Zhai, C. Lu, W. Ding, A. Hirose, K.F. Kobayashi, Corros. Sci. 47 (2005) 355–367.

60) L. Fournier, D. Delafosse, T. Magnin, Mater. Sci. Eng. A 269 (1999) 111–119.

61) S.P. Lynch, Acta Met. 20 (1988) 2639–2661.

62) C.D. Beachem, Metall. Trans. 3 (1972) 441–455.

63) O.A. Onyewuenyi, J.P. Hirth, Metall. Trans. A 14 (1983) 259–269.

64) D. McLean, Oxford University Press (1957).

65) T. Watanabe, Mater. Sci. Eng. A 166 (1993) 11–28.

66) T. Watanabe, S. Tsurekawa, S. Kobayashi, S.I. Yamaura, Mater. Sci. Eng. A 410 (2005) 140–147.

67) T. Watanabe, Mater. Sci. Eng. A 176 (1994) 39–49.

68) T. Watanabe, S. Tsurekawa, Acta Mater. 47 (1999) 4171–4185.

69) M.L. Kronberg, F.H. Wilson, Trans. Met. Soc. AIME 1947 (1949) 501–514.

70) D.G. Brandon, Acta Mater. 14 (1966) 1479-1484.

71) D.C. Crawford, G.S. Was, Metall. Trans. A 23 (1992) 1195–1206.

72) T. Watanabe. Res Mechanica. 11 (1984) 47–84.

73) M. Shimada, H. Kokawa, Z.J. Wang, Y.S. Sato, I. Karibe, Acta Mater. 50 (2002) 2331–2341.

74) L. Tan, T.R. Allen, J.T. Busby, J. Nucl. Mater. 441 (2013) 661–666.

75) V. Randle, Acta Mater. 47 (1999) 4187–4196.

76) V. Randle, M. Coleman, Acta Mater. 57 (2009) 3410–3421.

77) T. Hirano, Acta Metall. Mater. 38 (1990) 2667–2671.

78) H.Y. Bi, H. Kokawa, Z.J. Wang, M. Shimada, Y.S. Sato, Scr. Mater. 49 (2003) 219–223.

79) D. Stojakovic, Process. Appl. Ceram. 6 (2012) 1–13.

80) A.J. Wilkinson, T. Britton, Ben. Mater. Today. 15 (2012) 366–376.

81) W. Ludwig, A. King, M. Herbig, P. Reischig, J. Marrow, L. Babout, E.M. Lauridsen, H. Proudhon, J.Y. Buffière, J. Miner. Met. Mater. Soc. 62 (2010) 22–28.

82) A. King, M. Herbig, W. Ludwig, P. Reischig, E.M. Lauridsen, T. Marrow, J.Y. Buffière, Nucl. Instruments Methods Phys. Res. Sect. B Beam Interact. with Mater. Atoms. 268 (2010) 291–296.

83) W. Liu, G.E. Ice, B.C. Larson, W. Yang, J.Z. Tischler, Ultramicroscopy. 103 (2005) 199–204.

84) G.S. Was, S. Teysseyre, Z. Jiao, Corrosion. 62 (2006) 989–1005.

85) B. Sunil Kumar, B.S. Prasad, V. Kain, J. Reddy, Corros. Sci. 70 (2013) 55–61.

86) M.A. Groeber, B.K. Haley, M.D. Uchic, D.M. Dimiduk, S. Ghosh, Mater. Charact. 57 (2006) 259–273.

87) J.M. Sanz, C. Palacio, Y. Casas, J.M. Martinez‐Duart, Surf. Interface Anal. 10 (1987) 177–183.

88) J.J. Kai, C.H. Tsai, G.P. Yu, Nucl. Eng. Des. 144 (1993) 449–457.

89) H. Francois-Saint-Cyr, E. Anoshkina, F. Stevie, L. Chow, K. Richardson, D. Zhou, J.

Vac. Sci. Technol. B Microelectron. Nanom. Struct. 19 (2001) 1769.

90) J. Rand, G. Rozgonyi, J. Lu, R. Reedy, N. Carolina, Small (2002) 98–101.

91) R.N. Parkins, Jom. 44 (1992) 12–19.

92) T. Shibata, Iron Steel Inst. Japan. 31 (1991) 115–121.

93) O. Engler, V. Randle, CRC press. (2009).

94) S. Kikuchi, Proceedings of the Imperial Academy. 4 (1928) 271–274.

95) J.A. Venables, C.J. Harland, Phil. Mag. 27 (1973) 1193–1200.

Chapter 2 Mechano-chemical polishing of Alloy 600 for accelerated crack initiation in simulated PWR primary water environment and three-dimensional crystallographic characterization

2.1 Introduction

Alloy 600 is employed in pressurized water reactors (PWRs) for steam generator tubing and other structural materials. However, the alloy suffers from intergranular stress corrosion cracking (IGSCC). Therefore, the initiation and propagation of IGSCC in PWR primary environments have been investigated extensively[1–18]. In addition, the effects of the microstructure, precipitate, and dislocation on the initiation and propagation of cracks have been studied by characterizing the alloy surface or substrate where cracks initiate and/or propagate using scanning electron microscopy (SEM), transmission electron microscopy (TEM), Auger electron spectroscopy (AES), energy dispersive X-ray spectroscopy (EDS), atom probe tomography (APT) and secondary ion mass spectroscopy (SIMS)[1, 2, 5-7, 10, 16, 18].

Electron backscatter diffraction (EBSD) is an SEM-based diffraction technique that provides crystallographic information of grains in crystalline materials. Thus, the technique has been widely applied to characterize, for example, the plastic strain of stainless steel and nickel-based alloys[19–21]. It also has been recently adopted to characterize stress corrosion cracking of Alloy 600 in high–temperature water. Young et al. successfully obtained the grain boundary map, Euler angle image, and misorientation map around a stress corrosion cracking (SCC) crack generated on Alloy 600 in hydrogenated water at 360 °C[11]. Hou et al. also investigated the grain boundary map and Kernel average misorientation map near an SCC crack on Alloy 600 exposed to a corrosive solution consisting of sodium hydroxide, lead oxide, and pure water at 330 °C. They explained that the high dislocation density and strain concentration induced by cold work promoted crack propagation[14]. Both studies

examined the cross-sections of the specimens and focused on crack propagation rather than on crack initiation. Although the SCC of Alloy 600 has been studied according to various aspects such as slip dissolution, internal oxidation and hydrogen embrittlement, the initiation of cracks has not been crystallographically examined. To the best of the author knowledge, crystallographic evaluation of crack initiation on nickel-based alloys in high–temperature and high–pressure water environments has not been reported. In order to characterize the crystallographic features of the initiated crack, top-view observation is required. However, simulating IGSCC of Ni-based alloys such as Alloy 600 on the plane surface of a specimen is not easy. Furthermore, as the exposure of Alloy 600 to high–temperature water leads to the formation of relatively thick oxide layers on the alloy surface[22, 23], clear diffraction patterns of the underlying substrate alloy can not be acquired EBSD measurements. The author previously proposed a procedure to initiate intergranular cracks on the plane surfaces of Type 316L stainless steel and Alloy 600, and demonstrated that EBSD analysis could be performed on the surfaces[24].

Herein, the crystallographic approach based on EBSD measurements is presented in greater detail for Alloy 600 exposed to a simulated PWR primary water environment.

2.2 Experimental

The material examined was a 2 –mm-thick Alloy 600 sheet, the chemical composition of which is listed in **Table 2-1**. The mill-annealed Alloy 600 sheet was cold-worked with a reduction rate of 10%. A tensile specimen was cut from the sheet by using an electric discharge machine, and the specimen was mechanically ground with SiC abrasive papers up to #2000. This was followed by successive polishing with 9–and 1/4–μm diamond paste and mechano-chemical polishing with colloidal silica suspension for 20 min.

Table 2-1 Chemical composition of Alloy 600 (mass %)

Element	C	Si	Mn	Ni	Cr	Fe	P	S
mass %	0.01	0.31	0.36	75.01	15.71	7.35	0.009	< 0.001

A slow strain rate test (SSRT) was performed on the Alloy 600 specimen in a simulated PWR primary water environment. A solution containing 500 ppm B and 2 ppm Li as H_3BO_3 and LiOH, respectively was controlled at a temperature of 633 K with a dissolved oxygen concentration of less than 1 ppb and dissolved hydrogen concentration of 0.5 ppm. Furthermore, the pressure of the solution was controlled at 20 MPa during the SSRT. This environment is often used to simulate a PWR primary side water. The tensile specimen was elongated in the environment up to a strain of 10% at a rate of 5×10^{-7} s^{-1} and was held under this strain for 50 h.

After the SSRT, the specimen was characterized by FE-SEM and EBSD. Prior to EBSD characterization, the surfaces of the specimens were sputtered by Ar+ ions to remove the thick oxide films formed in the PWR primary environment. An EBSD measurement was performed for an area of 250×250 μm^2 with a step size of 1 μm on five locations at an acceleration voltage of 25 kV. In this work, the grain boundaries, where cracks initiated during the SSRT, were crystallographically analyzed. In order to perform the analysis, SEM images were captured at the same location at which EBSD was conducted. In the analysis, locations with misorientations greater than 15° (high–angle grain boundary) were defined as the grain boundary. In general, as cracks initiate and propagate inside a material along the grain boundary in IGSCC, crystallographic information of the grain boundary inside the material is required to better understand IGSCC. Therefore, three-dimensional characterization of crack initiation based on EBSD

was conducted in this study. Recently, the serial sectioning approach has been applied to three-dimensional analysis of the microstructures of polycrystalline materials and of surface oxidation[25–29]. In this study, gentle polishing with colloidal silica suspension and subsequent EBSD characterization were repeated at the same locations, which enabled us to obtain crystallographic data at different depths. In addition, triangular pyramidal indentations were introduced on the specimen surface and used as markers to estimate the displacement of grain boundaries by overlapping the grain boundary maps obtained by EBSD at different depths.

2.3 Results and discussion

Figure 2-1 shows typical SEM images of Alloy 600 surfaces after SSRTs were conducted in the simulated PWR primary environment. The alloy specimen shown in the images was cold-worked with a reduction rate of 20% prior to the SSRTs. In the SSRTs, the specimens were elongated once up to the tensile strain of 10% and then the strain was released. In other words, the specimen was not held under the strain for 50 h in this case. As shown in **Fig. 2-1(a)**, practically no cracks were observed for the specimen polished without colloidal silica suspension. By contrast, as shown in **Fig. 2-1(b)**, many cracks were formed on the specimen polished with colloidal silica suspension. To the best of the author knowledge, this study is the first case in which the initiation of IGSCC was realized by SSRT on a flat tensile specimen of Alloy 600, excepting the pioneer work by Totsuka et al. [28]. They used a tensile specimen with a ridge on the center of the gauge section to enhance on SCC. Fujimoto et al. previously reported that intergranular cracks were initiated on a non-sensitized Type 316L stainless steel during an SSRT in a dilute sodium sulfate solution at 561 K[30]. The surface of the stainless steel was also polished with colloidal silica suspension prior to the SSRT. This indicates that polishing with colloidal silica suspension

facilitates the initiation of IGSCC. By contrast, the transgranular stress corrosion cracking (TGSCC) occurred on the non-sensitized stainless steel polished without colloidal silica suspension under the same condition[30].

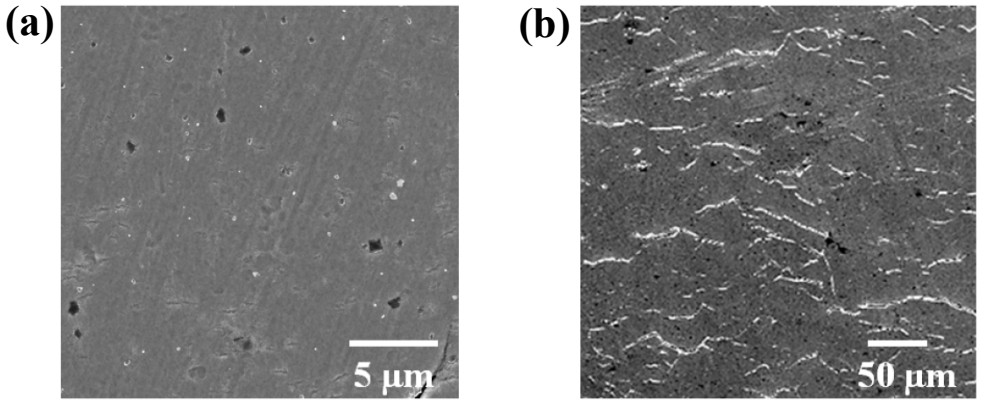

Fig. 2-1 SEM images of Alloy 600 surface after an SSRT in the simulated PWR primary environment: (a) without polishing by colloidal silica suspension, (b) with polishing by colloidal silica suspension.

Figure 2-2(a) presents an atomic force microscopy (AFM) image of the surface of Alloy 600 specimen prior to the SSRT. The image reveals an uneven textured surface of the alloy. However, no trenches were formed at the grain boundaries. The back scattered electron (BSE) image and inverse pole figure (IPF) map obtained at an identical location are shown in **Figs. 2-2(b)** and **2-2(c)**, respectively. The images clearly show that the surface asperity reflects crystallographic orientation, which is consistent with the observation for Alloy 22[31]. It was found that crystallographic orientation causes different dissolution rates of the alloy substrate during its mechano-chemical polishing with colloidal silica suspension, which results in this asperity. The asperity indicates that small steps are present at the grain boundary as schematically shown in **Fig. 2-2(d)**. These small

steps cause stress concentration at the grain boundary, leading to crack initiation. Therefore, it can be concluded that the microscopic asperity as shown in **Fig. 2-2(a)** facilitates the initiation of IGSCC. From these results, one can deduce that the initiation of IGSCC of Alloy 600 under practical operation might be attributed to the asperity generated as general corrosion by the long-term exposure to a PWR primary environment because of the difference in the dissolution rate based on the crystallographic orientation of grain.

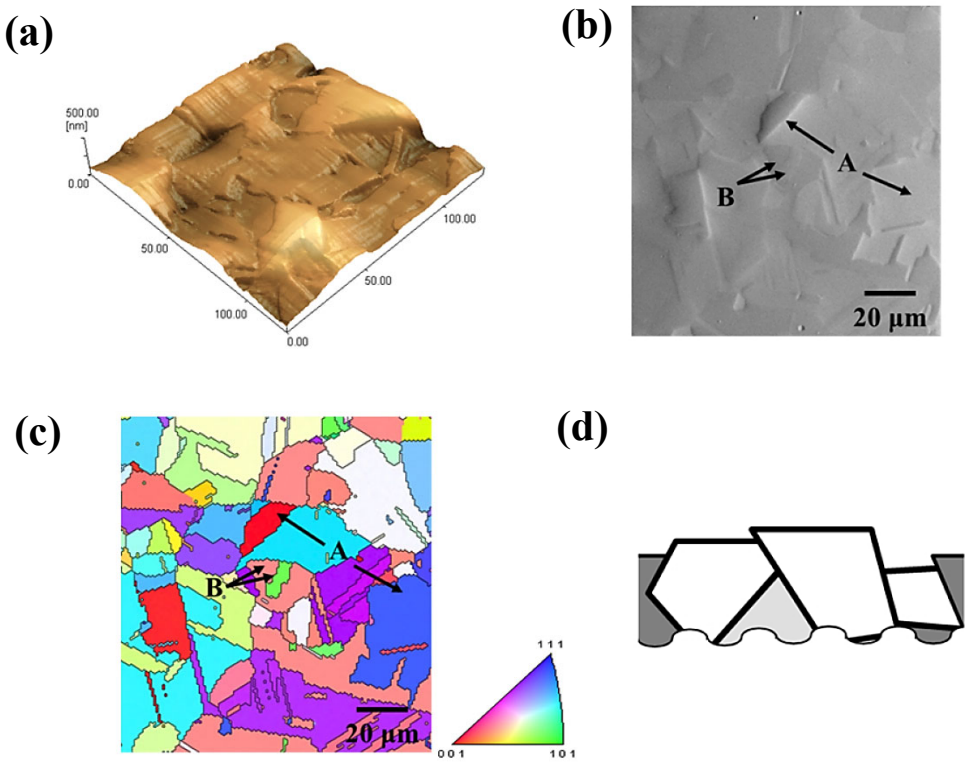

Fig. 2-2 (a) AFM image of Alloy 600 surface prior to the SSRT, (b) topography and (c) IPF map obtained at the same location, (d) schematic drawing of cross-view of grains near the alloy surface.

Although this work was conducted to examine the crack initiation on Alloy 600 in a simulated PWR primary environment based on crystallographic information, this type of information could not be obtained from the specimen immediately following the SSRT. As shown in **Fig. 2-3**, the specimen surface was covered with an oxide film and many corrosion products. Based on previous study of the author[23], a relatively thick oxide film was formed on the mill-annealed Alloy 600 during 24-h immersion in a similar PWR primary water environment. In the study, the thickness of the oxide film was estimated to be approximately 24 nm from the intensity attenuation of the Ni metallic peak of the substrate in the hard X-ray photoelectron spectra. The oxide film formed during the SSRT in this study was thicker than the previously reported oxide film on the mill-annealed Alloy 600. This was because the exposure time of Alloy 600 to the simulated PWR primary environment in this work was much longer than that in the previous work. The thick oxide film on the Alloy 600 surface prevented the measurement of electron–backscatter patterns from the underlying substrate. Therefore, the oxide film formed under the high–temperature and high–pressure water environment was removed by Ar+ ion sputtering.

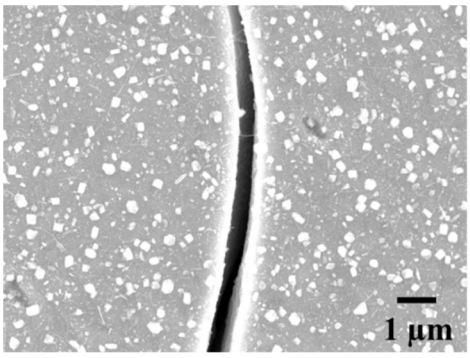

Fig. 2-3 SEM image of a crack formed on the Alloy 600 surface following an SSRT in the simulated PWR primary environment.

Figure 2-4(a) shows the SEM image of the Alloy 600 specimen after sputtering. Note that the horizontal direction of the images is parallel to the loading axis of the SSRT. It was evident that the thick oxide film and corrosion products were removed by sputtering, and cracks were clearly observed on the surface after sputtering. More importantly, all cracks were observed at the grain boundaries, indicating that IGSCC occurred on the alloy. Furthermore, many of the cracks initiated approximately perpendicular to the stress axis. **Fig. 2-4(b)** shows the IPF map of the same location shown in **Fig. 2-4(a)**. A clear IPF was obtained for the surface of the Alloy 600 specimen after the SSRT. Analysis of crystallographic data with the corresponding SEM image reveals the crystallographic features of IGSCC.

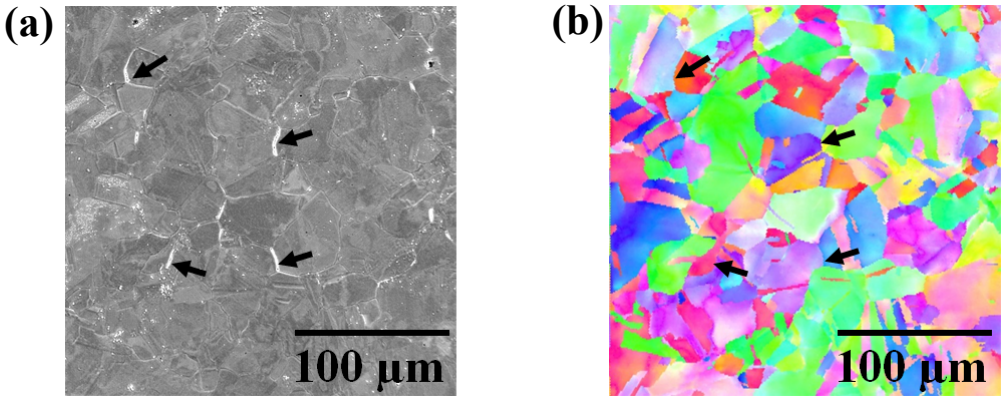

Fig. 2-4 (a) SEM image of the Alloy 600 surface after corrosion products formed during the SSRT were removed by sputtering, (b) IPF map obtained at the same location shown in (a).

Figure 2-5 shows the number fraction of CSL boundaries on 10% cold-worked specimen after SSRT in PWR primary water environment. The CSL grain boundaries were analyzed from Σ3 to 49. As a result, most of the CSL boundaries were Σ3, Σ9 and Σ27 in

the specimen. The other CSL boundaries were negligible because it exhibited significantly low distributions. Therefore, the investigation of IGSCC was conducted with emphasis on Σ3, Σ9 and Σ27 boundaries.

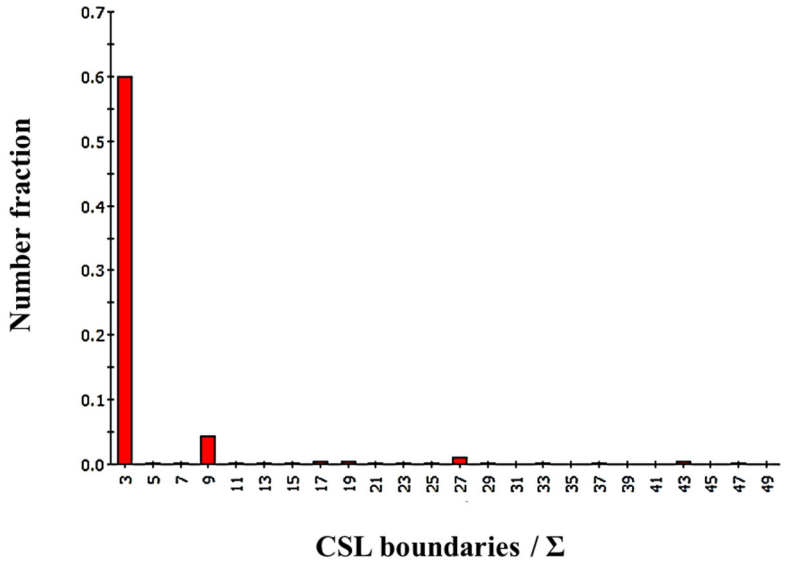

Fig. 2-5 Number fraction of CSL boundaries on 10% cold-worked specimen after SSRT in PWR primary water environment.

Figure 2-6 summarizes the probability of crack initiation calculated for the grain boundary with respect to the misorientation angle at the grain boundary. The probability of crack initiation was defined as the ratio of the number of cracked grain boundaries to the total number of grain boundaries for each range of misorientation angle. Furthermore, the probability can be summarized for the two categories of grain boundaries, that is, the random and coincidence site lattice (CSL) boundaries. On the alloy used in this work, three types of CSL boundaries as mentioned above, namely Σ3, Σ9, and Σ27, were recognized, with the calculated misorientation angles of 60°, 38.9°, and 31.6°, respectively. The figure indicates that the probability of crack initiation strongly depends on the type of grain

boundary. In other words, cracks initiate more readily at the random grain boundary than at the CSL boundary. In addition, for the random boundary, the probability of crack initiation is higher for the misorientation angles ranging from 30° to 40° as compared to the other ranges of misorientation angles. By contrast, the probability of crack initiation at CSL boundary was the highest in Σ27 boundary, and cracks did not initiate in Σ3 boundary.

Since the IGSCC cracks initiated and propagated along a grain boundary, gaining information about the grain boundary plane is important to understand the initiation and propagation of cracks.

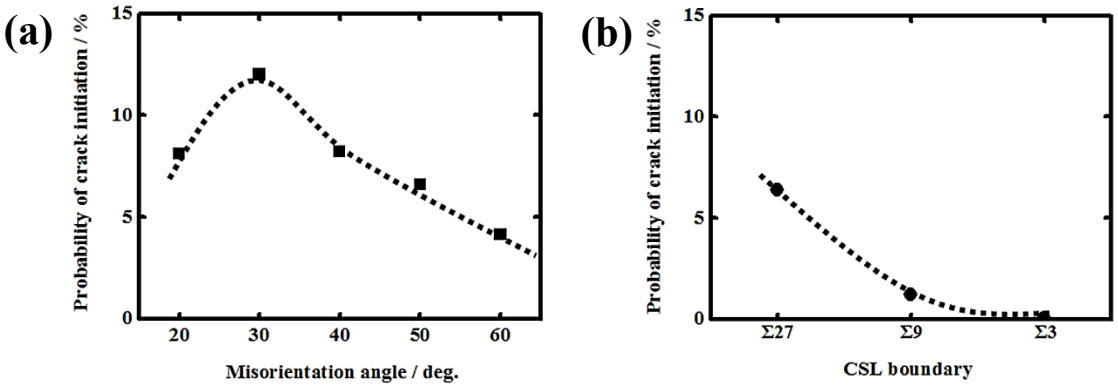

Fig. 2-6 Probability of crack initiation calculated for random and CSL boundaries against various misorientation angle ranges estimated with EBSD.

In this study, as illustrated in **Fig. 2-7**, the angle between a grain boundary plane and the stress axis was defined as grain-boundary-plane angle, θ, assuming that a grain boundary was flat. However, the direction of the crack could not be determined by an SEM observation, as it was performed only for the upmost surface of the specimen. Therefore, the author proposed a three-dimensional characterization of crack initiation, which was realized by repeated polishing and EBSD measurements. First, an EBSD measurement was conducted for the topmost surface after the sputtering as previously mentioned. Then, the

surface was gently polished with colloidal silica suspension to remove a layer of approximately 1-μm-in thickness from the specimen surface. This resulted in the displacement of the grain boundary based on the angle of the grain boundary plane to the surface. From the displacement of the grain boundary and the thickness of the removed specimen surface, the grain-boundary-plane angle was computed using a trigonometric function. In order to measure the displacement of the grain boundary, IPFs obtained at two different heights were used. Triangular pyramidal indentations were introduced as markers to perform EBSD measurement at the same locations after gentle polishing of the specimen and to estimate the thickness of the specimen removed during the polishing. **Fig. 2-8** presents the microscopic images of a triangular pyramidal indentation before and after gentle polishing as well as the corresponding depth profiles measured along the dotted lines shown in the microscopic images. It is clear that the indention mark remained after the gentle polishing. The depth profiles reveal that 1.08 μm of the specimen surface was removed in this case.

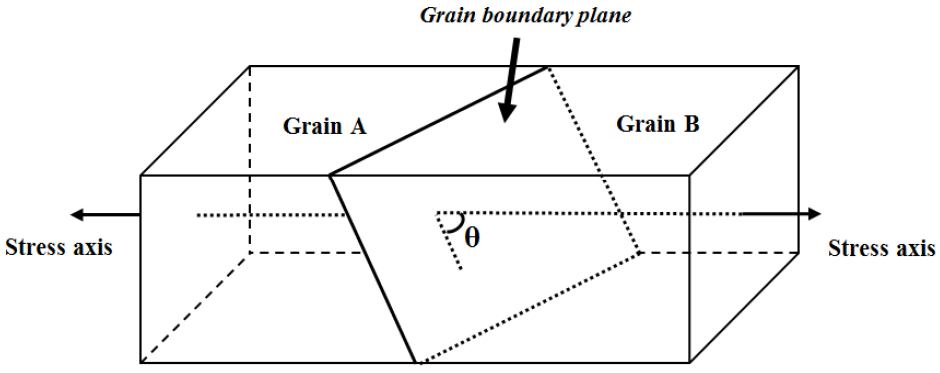

Fig. 2-7 Definition of grain-boundary-plane angle introduced in the present work. The stress axis is parallel to the rolling direction.

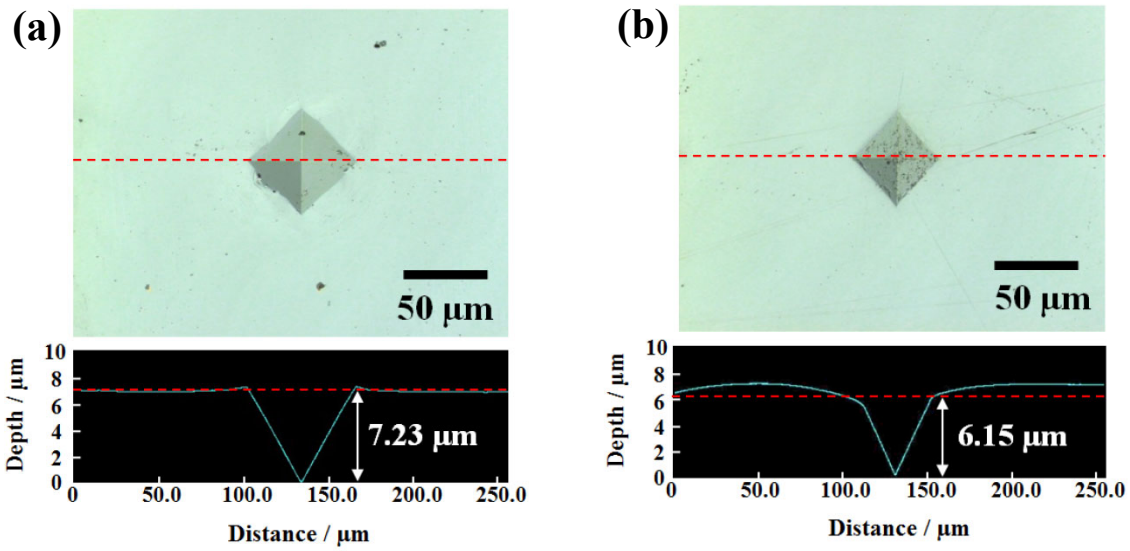

Fig. 2-8 Microscopic images of a triangular pyramidal indentation and depth profiles obtained at the same location (a) before and (b) after gentle polishing.

IPFs obtained at the same location on the specimen surface before and after gentle polishing are presented in **Fig. 2-9**. The grain boundary positions before and after gentle polishing were extracted from the IPFs and are shown to overlap in **Fig. 2-9(c)**. **Figure 2-9(d)** presents a magnified image of the site indicated by the square in **Fig. 2-9(c)**. The black and red lines in the images indicate the grain boundaries before and after gentle polishing, respectively. As can be seen, some red lines coincide with the black lines, whereas the other red lines deviate from the corresponding black lines. The distance between the lines reflects the displacement of the grain boundary.

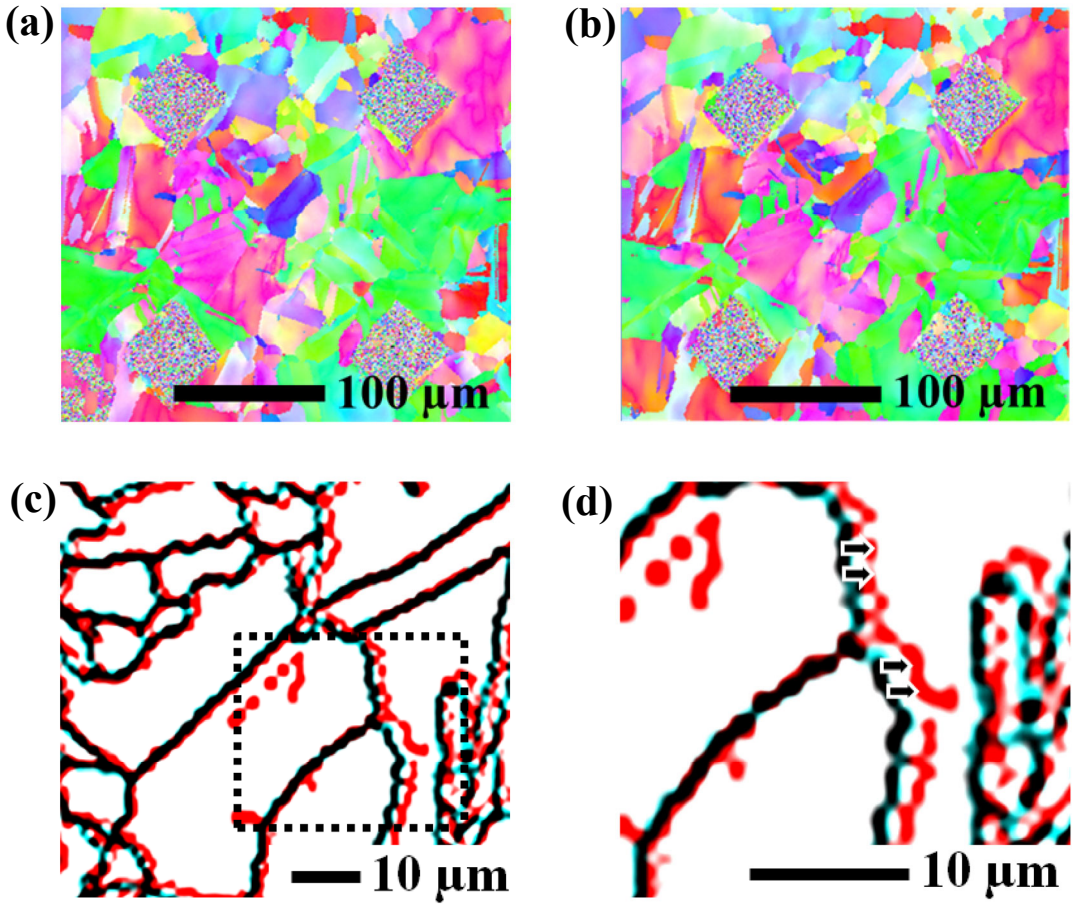

Fig. 2-9 IPF maps and grain boundary maps obtained at an identical location on the specimen (a) before and (b) after the gentle polishing. The overlapped IPFs present as (c) grain boundary image and (d) magnified image of the site indicated by the square of (c).

Using the displacement at each boundary and the removed thickness, the author calculated the grain-boundary-plane angle, which is summarized in **Fig. 2-10**. Since it was polished by 1 μm to 2 μm from top surface of specimens, it is possible to determine the crack depth for cracks initiated at grain boundaries. In the figures, the number of cracks with a depth of approximately 1 μm significantly decreased after gentle polishing, indicating that the depths of most of the cracks were less than 1 μm. Cracking did not occur at the grain angle corresponding to the grain-boundary-plane angle of 0 ˚ and 90 ˚.

More cracks were recognized at the random boundary than at the CSL boundary. Lehockey et al. reported a similar result in which a crack appeared exclusively confined to the random boundary rather than at the CSL boundary[32]. Around the misorientation angle of 40º for the random boundary, cracks initiated with a wide range of grain-boundary-plane angle. For other misorientation angle ranges, the grain-boundary-plane angles were approximately 40°. A similar trend was observed for the CSL boundary as shown in **Fig. 2-10(b)**. Although further analysis is required to discuss in more detail the mechanism of SCC crack initiation in terms of the crystallography of the grain boundary, the results of the present study indicate that the proposed approaches can facilitate the initiation of IGSCC and provide crystallographic information of grain boundaries on the surface as well as inside the alloy.

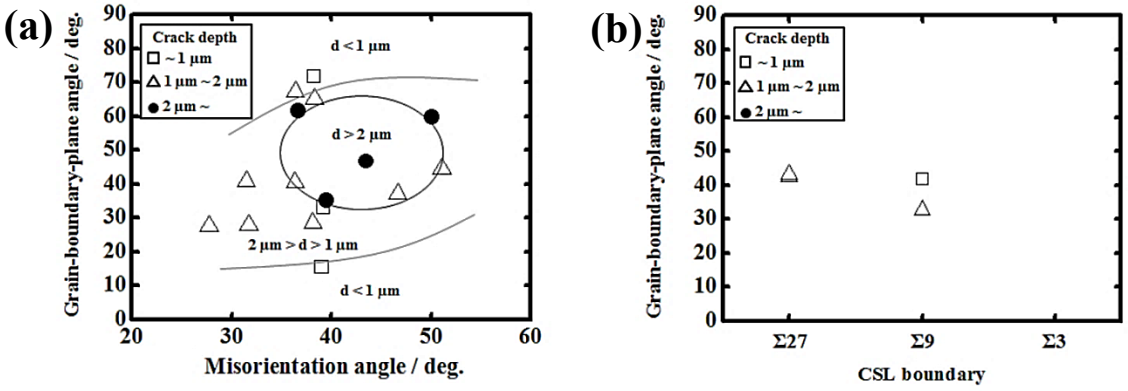

Fig. 2-10 Grain-boundary-plane angle derived for (a) random and (b) CSL boundaries.

2.4 Conclusion

In this chapter, the author described the crystallographic characterization of IGSCC cracks initiated on Alloy 600 in a simulated PWR primary environment. Mechano-chemical polishing with colloidal silica suspension facilitated crack initiation. A thick oxide film and many corrosion products were formed on the alloy surface during an

SSRT, which prevented EBSD measurement. However, sputtering of the oxide film and corrosion products enabled us to obtain clear IPFs and to analyze the IGSCC cracks crystallographically. The probability of crack initiation was higher at the random than at the CSL boundary, although the probability of crack initiation for the Σ27 boundary was similar to that for the random boundary. Furthermore, grain-boundary-plane angles were calculated from EBSD measurements at different depths, which were achieved by the repeated gentle polishing of the specimen. The grain-boundary-plane angle centered around a specific angle of 40°, independent of the misorientation angle as well as the type of grain boundary (random or CSL). However, at the misorientation angle of approximately 40°, cracks initiated with a wide range of grain-boundary-plane angles.

References

1) R.A. Page, Corrosion 39 (1983) 507–507.

2) R. Bandy, D. Vanrooyen, J. Mater. Energy Syst. 7 (1985) 237–245.

3) J.R. Crum, Corrosion 42 (1986) 368–372.

4) S.M. Bruemmer, Jr. C Henager. Scr. Metall. 20 (1986) 909–914.

5) G. Economy, R.J. Jacko, F.W. Pement, Corrosion 43 (1987) 727–734.

6) S.M. Payne, P. McIntyre, Corrosion 44 (1988) 314–319.

7) C.H. Shen, P.G. Shewmon, Metall. Trans. A (1990) 1261–1272.

8) R.B. Rebak, Z. Szklarska-Smialowska, Corros. Sci. 38 (1996) 971–988.

9) T.M. Holden, R.A. Holt, A.P. Clarke, Mater. Sci. Eng. A 246 (1998) 180–198.

10) L.E. Thomas, Corrosion 56 (2000) 572–587.

11) G.A. Young, W.W. Wilkening, D.S. Morton, E. Richey, M. Lewis, Proceedings of the 12th International Conference on Environmental Degradation of Materials in Nuclear Power Systems – Water Reactor – (2005) 913-922.

12) J.B. Ferguson, H.F. Lopez, Phys. Metall. Mater. Sci. 37 (2006) 2471–2479.

13) J. Panter, B. Viguier, M. Foucault, P. Combrade, E. Andrieu, 348 (2006) 213–221.

14) J. Hou, Q.J. Peng, T. Shoji, J.Q. Wang, E.H. Han, W. Ke, Corros. Sci. 53 (2011) 2956–2962.

15) Z. Lu, T. Shoji, S. Yamazaki, K. Ogawa, Corros. Sci. 58 (2012) 211–228.

16) K. Arioka, T. Yamada, T. Miyamoto, M. Aoki, Corrosion 70 (2014) 695–707.

17) A. Telang, A.S. Gill, D. Tammana, X. Wen, M. Kumar, S. Teysseyre, S.R. Mannava, D. Qian, V.K. Vasudevan, Mater. Sci. Eng. A. 648 (2015) 280–288.

18) D.K. Schreiber, M.J. Olszta, D.W. Saxey, K. Kruska, K.L. Moore, S. Lozano-Perez, S.M. Bruemmer, Microsc. Microanal. 19 (2013) 676–687.

19) M. Kamaya, A.J. Wilkinson, J.M. Titchmarsh, Acta Mater. 54 (2006) 539–548.

20) L.N. Brewer, M.A. Othon, L.M. Young, T.M. Angeliu, Microsc. Microanal. 38 (2002) 684–685.

21) A. Sáez-Maderuelo, L. Castro, G. De Diego, J. Nucl. Mater. 416 (2011) 75–79.

22) Q. Peng, J. Hou, K. Sakaguchi, Y. Takeda, T. Shoji, Electrochim. Acta 56 (2011) 8375–8386.

23) S. Fujimoto, W.S. Kim, M. Sato, J.Y. Son, M. Machida, K.T. Jung, H. Tsuchiya, J. Solid State Electrochem. 19 (2015) 3521–3531.

24) K.T. Jung, T. Ogawa, Y. Morita, S. Fujimoto, Proceedings of 17th International Conference on Environmental Degradation of Materials in Nuclear Power Systems – Water Reactor – 2 (2015) 895-903.

25) J.E. Spowart, Scr. Mater. 55 (2006) 5–10.

26) A.C. Lewis, J.F. Bingert, D.J. Rowenhorst, A. Gupta, A.B. Geltmacher, G. Spanos, Mater. Sci. Eng. A. 418 (2006) 11–18.

27) S. Zaefferer, S.I. Wright, D. Raabe, Metall. Mater. Trans. A Phys. Metall. Mater. Sci. 39 (2008) 374–389.

28) N. Totsuka, E. Lunarska, G. Cragnolino, Natl. Assoc. Corros. Eng. 43 (1987) 505–514.

29) S. Lozano-Perez, K. Kruska, I. Iyengar, T. Terachi, T. Yamada, Corr. Sci. 56 (2012) 78-85.

30) S. Fujimoto, H. Masaki, T. Saito, Proceedings of the 15th International Conference on Environmental Degradation of Materials in Nuclear Power Systems—Water Reactors. Springer, Cham, 2011.

31) J.J. Gray, B.S. El Dasher, C.A. Orme, Surf. Sci. 600 (2006) 2488–2494.

32) E.M. Lehockey, G. Palumbo, P. Lin, Metall. Mater. Trans. A 29 (1998)3069–3079.

Chapter 3 Micro-crystallographical Characterization of Initiation of Intergranular Stress Corrosion Cracking on Alloy 600 in Terms of Local Stress at Grain Boundary Induced by Slip Deformation

3.1 Introduction

Alloy 600 has been widely employed as component materials in pressurized water reactor (PWR), including steam generator (SG) tubes, control rod drive mechanism (CRDM), safe ends, and various instrumentation ports. Intergranular stress corrosion cracking (IGSCC) occurred on Alloy 600 in PWR primary water environments[1-3], resulting in a drastic reduction in the lifetime of components made from the alloy. This has been one of the critical issues faced by the nuclear industry[1,4,5]. Although most applications have replaced Alloy 600 with thermally-treated Alloy 600 (Alloy 600 TT) [6, 7] or more Cr containing Alloy 690, there are still some facilities using Alloy 600[6-10]. Therefore, extensive efforts have been dedicated to understanding and preventing IGSCC of high nickel alloys including Alloy 600 in the PWR primary water environment. Several mechanisms such as internal oxidation[11, 12], hydrogen embrittlement[13-17], and slip dissolution[18-20] have been proposed for IGSCC of nickel-based alloys. In addition, it has been reported that stress[7, 21, 22], grain boundary characteristics[23, 24], cold work (CW)[25-27], temperature, and dissolved hydrogen (DH) concentration[18,28-30] affect IGSCC. Although IGSCC occurs at the grain boundary, cracks do not necessarily initiate at all grain boundaries[31, 32], implying that grain boundary characteristics affect the IGSCC susceptibility of high nickel alloys.

Grain boundaries can be classified as random or coincidence site lattice (CSL) boundaries. It is well known that Σ3 boundaries exhibit superior resistance to IGSCC[33-35].

Gertsman and Bruemmer examined the grain boundary characteristics of austenitic alloys and concluded that only coherent twin Σ3 boundaries can be considered as special grain boundaries, and twin interactions with random boundaries may suppress crack propagation[36]. Crawford and Was demonstrated that CSL boundaries in Alloy 600 are more resistant to cracks than other boundaries in argon or highly deaerated pure water[37]. Moreover, Alexandreanu *et al*. reported that grain boundary deformation behaved as a precursor of IGSCC on a Ni-based alloy in high temperature water[35]. Hou et al. showed that the grain boundary deformation and crack growth rate increased on a 20% CW specimen owing to the non-uniform strain concentration induced by the slip deformation and high dislocation density[27]. In addition to the above-mentioned results and discussion, mechanisms such as intergranular oxidation that have been developed from the internal oxidation model proposed by Scott et al.[11, 12], and hydrogen embrittlement have been related to the grain boundary characteristics. Bertali et al. reported that variations in morphology of the oxidized surface of Alloy 600 were observed at triple points of grain boundaries and at the intersection of twin and high angle grain boundary, indicating that the grain boundary characteristics are important in the oxidation susceptibility[38]. Furthermore, the preferential intergranular oxide penetration was reported to occur along newly migrated and solute-depleted grain boundary rather than the original grain boundary[39]. In contrast, the grain boundary characteristics have been reported to affect hydrogen segregation, leading to the crack initiation. The molecular dynamics and Monte Carlo simulation for Ni indicated that boundaries vicinal to the coherent twin exhibited significant changes in the structure of the boundary as well as the amount of segregated hydrogen[40]. The effect of hydrogen on the resistance of CSL boundaries against crack initiation was controversial. Seita et al. indicated that coherent twin boundaries were most susceptible to crack initiation[41]. In contrast, Bechlte et al. reported that the increase in the

fraction of twin boundary enhanced the tensile ductility and fracture toughness when the hydrogen concentration in a commercially pure nickel was ranged from 1200 and 3400 ppm[42]. Seita et al. further examined crack initiation at coherent twin boundaries in hydrogen-charged Alloy 725 crytstallographically, focusing on the angle between the coherent twin boundary plane normal and the tensile axis as well as the smallest angle between a <110>-type direction in the coherent twin boundary plane and the steepest direction along the coherent twin boundary plane. They analyzed data using the Kullback-Leibler divergence and proposed probabilistic failure criteria[43]. Conversely, grain boundary fracture is known to be triggered by the stress operating at grain boundary. Therefore, both the grain boundary characteristics as well as stress operating at grain boundary may affect the crack initiation on Alloy 600.

The author of this thesis also studied IGSCC of Alloy 600 in a simulated PWR primary environment to correlate IGSCC initiation with the grain boundary characteristics. The author reported for the first time that IGSCC initiated on a flat tensile specimen of mill-annealed Alloy 600 in less than 50 hours in a simulated PWR primary water environment by a slow strain rate testing (SSRT), if the specimen surface was finished with colloidal silica suspension [44, 45]. Then many crack initiations were characterized by a field emission scanning electron microscope (FE-SEM) equipped with an electron backscatter diffraction (EBSD) apparatus. The results were statistically analyzed to reveal that the crack initiation probability exhibited a maximum for grain boundaries with misorientation angle of 30-40°[44, 45]. Furthermore, the angle between tensile-axis and grain-boundary plane was determined by FE-SEM and EBSD measurements at successive depths which were achieved by repeated gentle polishing and FE-SEM / EBSD observations. Through the above-mentioned experiments, the author found that IGSCC tends to occur at grain boundaries with an approximate 40° grain-boundary plane angle, regardless of the

misorientation angle as well as the type of grain boundary (random or CSL)[45]. However, in polycrystalline alloys, homogeneously loaded remote stress induces slip deformation in grains owing to shear stresses acting on a slip plane along a slip direction determined by the Schmid law in each grain. Therefore, the stress at grain boundary is generated by the shear stresses in adjacent grains; that is, the stress generated at each grain boundary depends on the slip deformations of adjacent grains. To the best of the author's knowledge, IGSCC initiation, not limited on Alloy 600, has not been characterized experimentally in terms of the stress operating at the grain boundary.

The purpose of this study is to evaluate the effects of grain boundary characteristics and stress operating at grain boundaries on the IGSCC susceptibility of Alloy 600 in a simulated PWR primary water environment. The author characterized the crystal orientation of many grains by using an EBSD, then determined the slip deformation direction of each grain and estimated the stress generated at the common grain boundary adjacent to the two grains. The results were statistically analyzed to discuss the IGSCC initiation mechanism.

3.2 Experimental

Flat tensile Alloy 600 specimens of 2 mm thickness with a gauge section of 4 mm width and 10 mm length were fabricated from alloy sheets which were subjected to mill-annealing and subsequent cold work with the reduction rates of 10% and 20%. The chemical composition of the alloy was as follows (mass%) ; C: 0.01, Si: 0.31, Mn: 0.36, Ni: 75.01, Cr: 15.71, Fe: 7.35, P: 0.009, S: < 0.001. The surface of the specimens was ground using SiC abrasive papers up to #2000, and then polished with 9 μm and 1/4 μm diamond pastes, followed by mirror-finishing using a colloidal silica suspension for 20 min. This surface treatment could result in crack initiation on the Alloy 600 flat tensile

specimens in a considerably short time through SSRT as previously reported[44-46]. After polishing, the tensile specimens were ultrasonically cleaned using acetone, ethanol, and deionized water for 5 min, successively. Then, SSRT was carried out to examine the IGSCC of Alloy 600 tensile specimens in a simulated PWR primary water environment. The simulated primary water comprised 500 ppm of B and 2 ppm of Li in the form of H_3BO_3 and LiOH, respectively. The dissolved hydrogen concentration was controlled at 2.75 ppm, whereas the dissolved oxygen concentration was limited to less than 1 ppb. This condition is typical of the simulated PWR primary water environment employed for laboratory tests, because this condition is located near the Ni/NiO equilibrium, where Ni based alloys are known to exhibit maximum IGSCC susceptibility[47-50]. The SSRTs were performed at a temperature of 633 K and at a pressure of 20 MPa. During the SSRT, the tensile specimens were elongated up to 10% of a strain with the strain rate of 5×10^{-7} s^{-1}. Then, the strain was maintained for 50 h and the SCC test was terminated. Oxide films, typically 20-50 nm in thickness, were formed on the surface of the specimens in the simulated PWR primary water environments as previously reported[51]. The oxide films were removed by Ar^+ ion beam sputtering before FE-SEM/EBSD characterizations. The sputtering was operated at 400 eV and 500 μA/cm^2 for typically 90 s. This sputtering condition was determined by preliminary tests to completely remove the oxide films formed in the high temperature aqueous solution. The EBSD measurements were performed at five different locations on the specimen surfaces for an area of 250 x 250 μm^2 with a step size of 1 μm at an accelerating voltage of 25 kV. SEM images of identical locations were also obtained at the same accelerating voltage.

3.3 Results

Figure 3-1 presents the distribution of the grain boundary characteristics in the tensile specimens with respect to the misorientation angle. In the figure, the random and CSL boundaries were counted separately for 10% CW and 20% CW specimens. The distributions indicate that in both specimens, a considerably large number of Σ3 grain boundaries was present. The number of CSL boundaries was in the order of Σ3 boundary > Σ9 boundary > Σ27 boundary in both specimens.

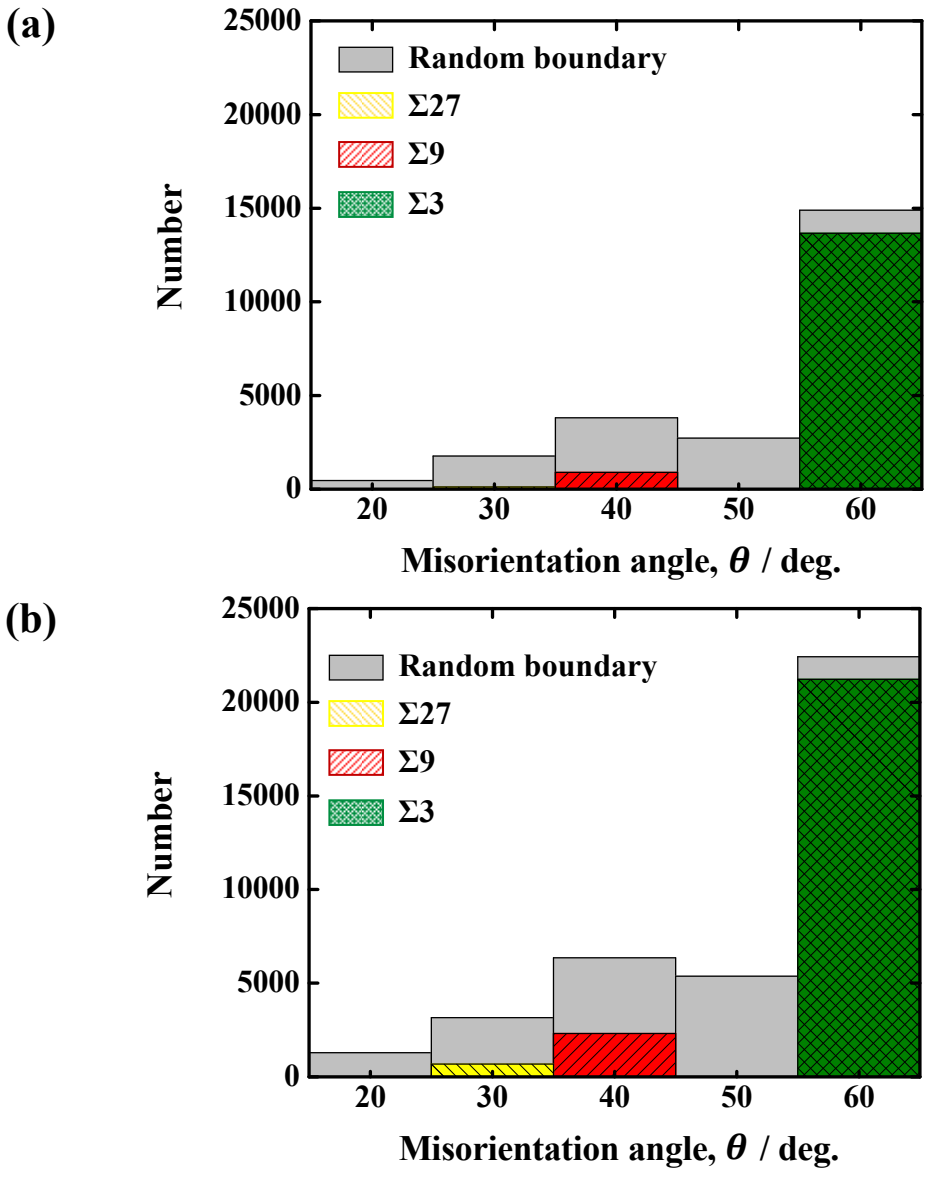

Fig. 3-1 Number of grain boundaries with respect to their misorientation angles; (a) 10%CW specimen and (b) 20%CW specimen.

Figure 3-2(a) represent the locations of the cracks, whereas the white arrows in **Fig. 3-2(b)** represent identical locations in their black counterparts. This comparison indicates that cracks initiated along the grain boundaries. Similar results were also obtained for the 20% CW specimen.

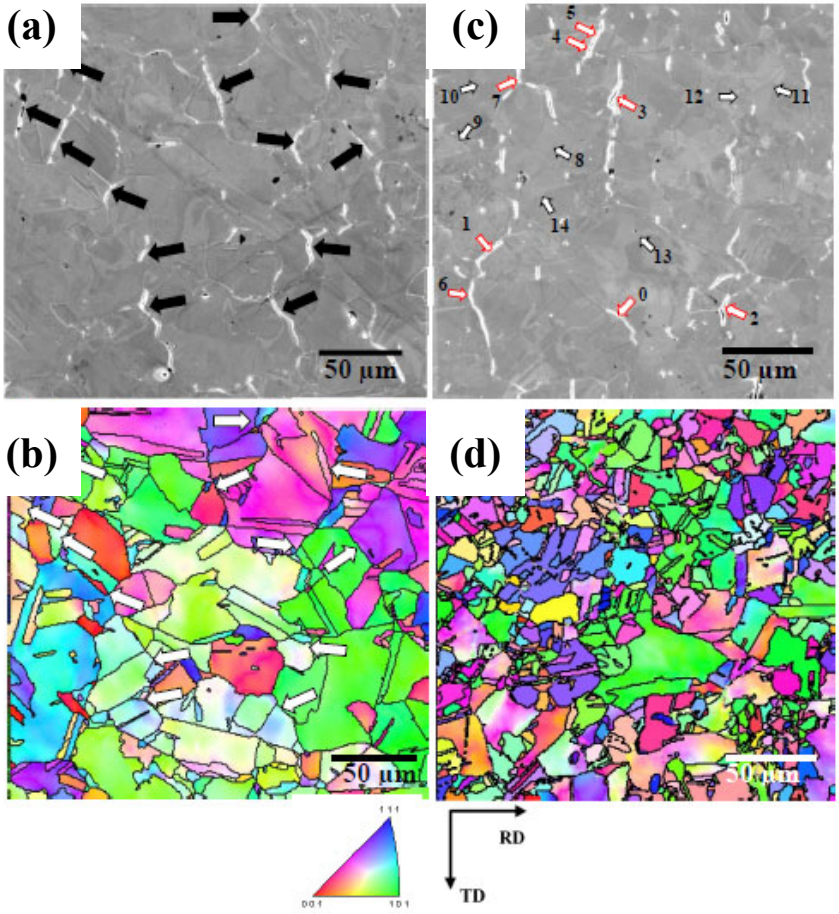

Fig. 3-2 SEM image and the corresponding IPF map of (a), (b)10% CW specimen and (c), (d) 20% CW specimen, after the SSRT. The arrows in (a) and (b) indicate corresponding cracked boundaries. The numbers in (c) correspond to the numbers in Figs. 3-5(b) and 3-8.

The observed cracks were crystallographically analyzed based on the EBSD analysis. To ensure the reliability of the analysis, the EBSD measurements were performed at five different sites on each specimen. All the grain boundaries present within these sites were analyzed; however, grain boundaries of less than 5 μm were excluded from the analysis. In the present study the author consider the stress generated at grain boundary. This can be analyzed based on the crystal plasticity theory proposed by Taylor[52], considering elastic deformation until the yield point, shear strain rate, and strain hardening that exhibit anisotropy for each grain. The author of the present study previously reported on the stress generated at the grain boundaries of an Alloy 600, which caused IGSCC in a PWR primary water environment using a multi-scale finite element method (FEM). In the analysis the geometry and crystallographic orientation of all grains in a 100×100 μm^2 area were determined using a FE-SEM/EBSD, then the stress and strain generated at all grain boundaries were evaluated by FEM. The results correlated with IGSCC occurrences. In the FEM analysis, to minimize geometry noise, small grains were excluded, and grain boundaries were revised to be smooth lines. This approach is not straightforward and requires significant efforts in pre-processing for the analysis. Additionally, a certain level of computational resources is required for the FEM. Therefore, in the present study the author introduced a simplified stress evaluation method for a large number of grain boundaries without considering elastic deformation and yielding.

Generally, when a polycrystalline metal or alloy is elongated beyond its elastic limit, slip deformation occurs along the slip plane and slip direction; these are, in turn, determined by the crystal orientation and stress direction for each grain. Therefore, the slip deformations along different directions in two adjacent grains can induce local stress at the grain boundary between these grains. In the present study, the initiation of IGSCC is discussed considering the stress generated at the grain boundary.

First, crystal orientations of all grains were identified using an EBSD. Subsequently, a slip system, including slip planes and slip directions, was determined for each grain. As Ni based alloys with a face centered cubic structure possess 12 equivalent slip systems, slip deformation basically occurs in the most deformable slip system, that is, the primary slip system. This can be identified as the one having the maximum Schmid factor. The shear stress acting on a slip plane in a slip direction within a grain is the product of the tensile stress applied to the specimen and the Schmid factor of the grain (Schmid law). For simplifying, assuming that the applied remote tensile stress is common for all grains in a specimen, the magnitude of the shear stress vector is proportional to the maximum Schmid factor in each grain when the primary slip system is active. In the deformation of polycrystalline metal, the rotation of grains as well as that of lattice within a grain will occur due to the restraint by adjacent grains, resulting in the deformation with multi slip systems within a grain as well as in the grain subdivision. This causes this stress analysis more complicated. Therefore the author assumes further that the rotation of grain is ignored, and a single slip system is considered to be operative. Local stresses operating to grain boundaries were estimated under these assumptions as follows.

The shear stress on a slip plane in a grain is assumed to cause certain stress to grain boundary, which is in proportion to the magnitude of the shear stress. Although the stress generated at the grain boundary plane may induce IGSCC, the angle between the grain boundary plane and the shear stress direction was unknown because in the present study the grain boundary plane under the surface of the specimen was not observed. Therefore, the stress operating at grain boundary plane could not be evaluated. In the present work, instead, the shear stress vector determined for each grain was projected onto the surface, as illustrated in **Fig. 3-3(a)**. The stress acting on a grain boundary at the surface may induce cleavage or slip of grain boundary, resulting in IGSCC. For these reasons, the shear stress

vector projected on the surface is analyzed in the following. **Figure 3-3(b)** presents examples of the distribution of the projected shear stress direction on the surface of the 10% and 20% CW specimens after SSRT. In these figures, the direction is described not as a shear stress vector but as a scalar. Noted that the shear stress induced on a slip plane of a grain will act in opposite directions for two grain boundaries surrounding one grain based on the continuum mechanics, as illustrated in Grain 2 of **Fig. 3-3(c)**. As shown in **Fig. 3-3(c)**, the projected shear stress vector, $\vec{d}$, was decomposed into mutually perpendicular components, *i.e.*, one is parallel to the grain boundary, whereas the other is vertical to the grain boundary. In the figure, the parallel component of a decomposed vector is expressed as $\vec{a}$, and the vertical one is expressed as $\vec{b}$. The stress operating at a grain boundary differs depending on the type of decomposed vectors (parallel or vertical) and their directions.

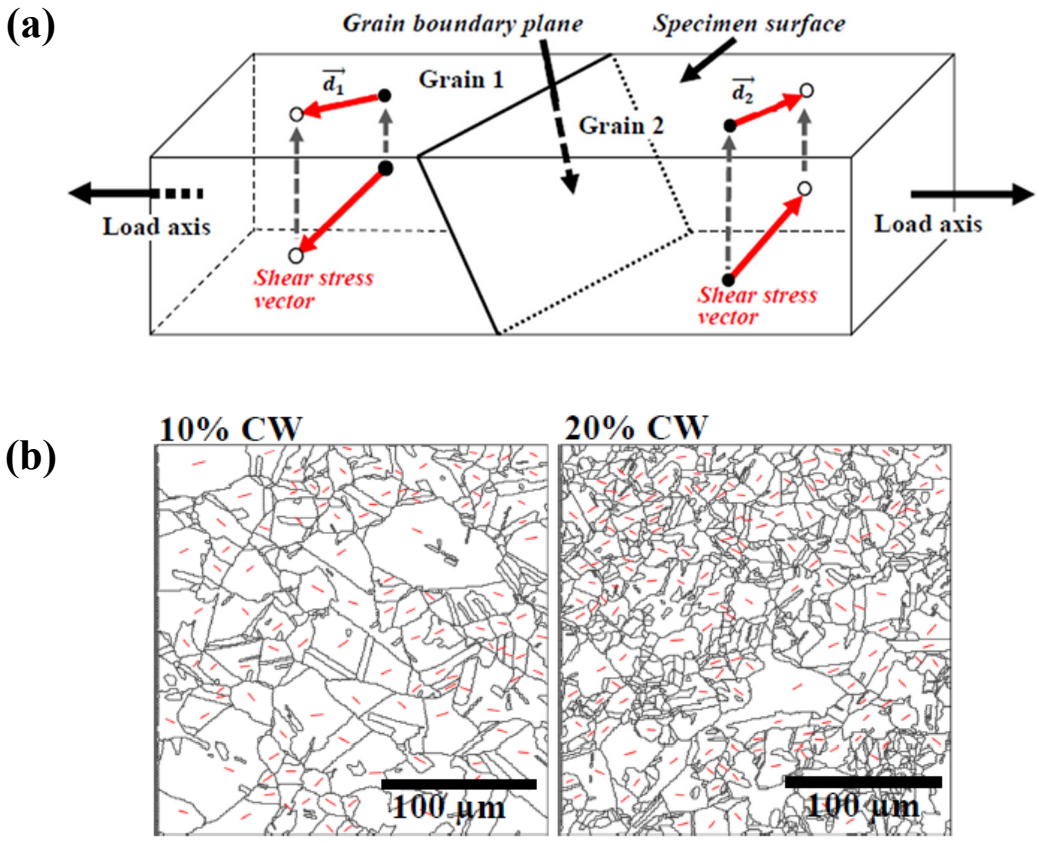

(c)

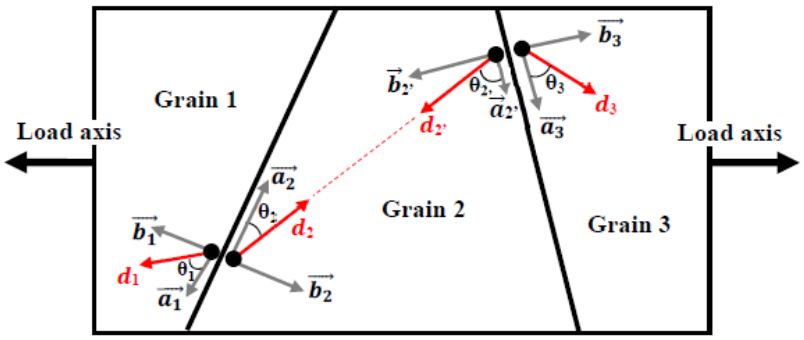

Fig. 3-3 (a) Schematic illustration on the analysis of crack initiation in terms of stress operating at a grain boundary. (b) Examples of shear stress scalars projected on the surfaces of the specimens. (c) Schematic illustration on an example of the decomposition of the projected shear stress vectors. Note that the shear stress vectors operating in Grain 2 adjacent to Grain 1 and Grain 3 are in an identical magnitude but in opposite directions.

Figure 3-4 illustrates four cases whereby the decomposed vectors generated in two grains act differently at the common grain boundary. Regarding the parallel vectors shown in **Fig. 3-4(a)**, a large shear stress operates at the grain boundary between adjacent grains when the directions of the two vectors are opposite. This can induce a crack initiation. However, the shear stress operating at the grain boundary is small when the directions are the same, as illustrated in the lower case of **Fig. 3-4(a)**. In particular, if the two vectors are the same, no shear stress occurs at the grain boundary. In the case of vertical vectors, their combinations are complicated as illustrated in **Fig. 3-4 (b)-(d)**. For the case shown in **Fig. 3-4(b)**, the directions of the vectors are opposite to each other, similar to those in **Fig. 3(c)**. This causes a tensile stress at the grain boundary between the grains. A cleavage of the grain boundary may then result, that is, crack initiation. By contrast, for the case shown in **Fig. 3-4(c)**, although the directions of the vectors are opposite, the vectors face each other

across the grain boundary. This causes a compressive stress at the grain boundary. Cracks may scarcely initiate in this case. Furthermore, for the case shown in **Fig. 3-4(d)**, where the directions of the vertical vectors are the same, the type of stress operating at the grain boundary differs depending on the magnitude of each vertical vector. For simplicity, only the situations where both vectors point to the right are considered, as illustrated in **Fig. 3-4(d)**. When the vertical vector on Grain 2 is smaller than that on Grain 1, a compressive stress operates at the grain boundary. However, in the opposite case, a tensile stress operates at the grain boundary, leading to crack initiation. The stress at grain boundaries is analyzed according to the aforementioned scenario.

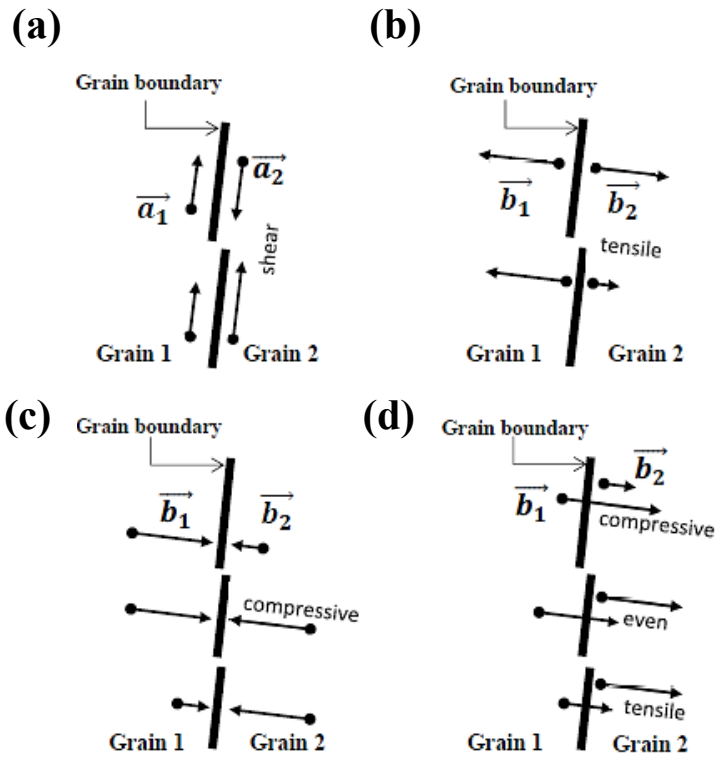

Fig. 3-4 Schematic illustration on the combinations of decomposed stress vectors; (a) parallel to grain boundary, (b)–(d) perpendicular to grain boundary.

Figures 3-5 (a) and **(b)** summarize the distribution of the type of stress operating at grain boundaries in the 10% and 20% CW specimens, respectively. This is evaluated after the SSRT in the simulated PWR environment with DH concentration of 2.75 ppm and at 633 K. The values indicated in the horizontal and vertical axes are the resolved stress intensities, assuming that the remote tensile stress loaded on the specimen is unity. The solid marks in the figures indicate cracked grain boundaries. The figures were obtained using data based on the analysis at one site shown in **Fig. 3-3(b)**. As many cracked grain boundaries are present in the figures, crack initiation is statistically discussed. It is clear that in both specimens, cracks initiated at the grain boundaries where a large tensile stress operated, whereas no cracks initiated at the grain boundaries where compressive stress operated. This is rational because the tensile stress contributes to the cleaving of the grain boundary, whereas the compressive one does not.

To quantitatively assess the crack susceptibility, the probability of crack initiation was evaluated with respect to each stress factor; the results are presented in **Fig. 3-6**. As expected from **Fig. 3-5**, the probability of crack initiation is 0 when compressive stress operates on grain boundaries (not described in **Fig. 3-6**), i.e., the cleaving of the grain boundary is not triggered by the compressive stress. The probability tends to increase with increasing tensile factor, whereas the probability of crack initiation induced by the shear stress decreases for shear factor ranging from 0.6 to 1. These analyses indicate that crack initiation can be triggered mainly by the tensile stress.

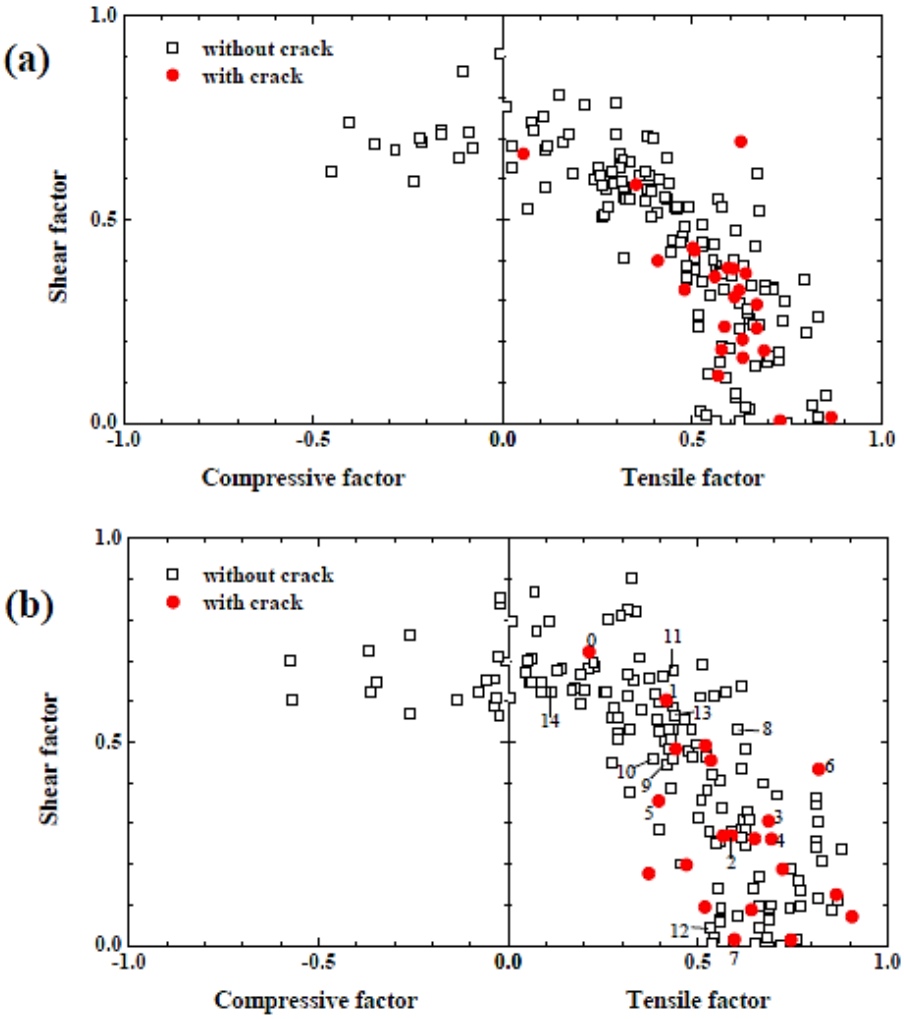

Fig. 3-5 Correlation of various stresses operating at the grain boundary; (a) 10%CW specimen, (b) 20%CW specimen. Solid marks indicate the grain boundaries where crack initiated. The numbers indicated in (b) correspond the ones in Figs. 3-2 (c) and 8 ; 0 – 7 are cracked, and 8 – 14 are not cracked.

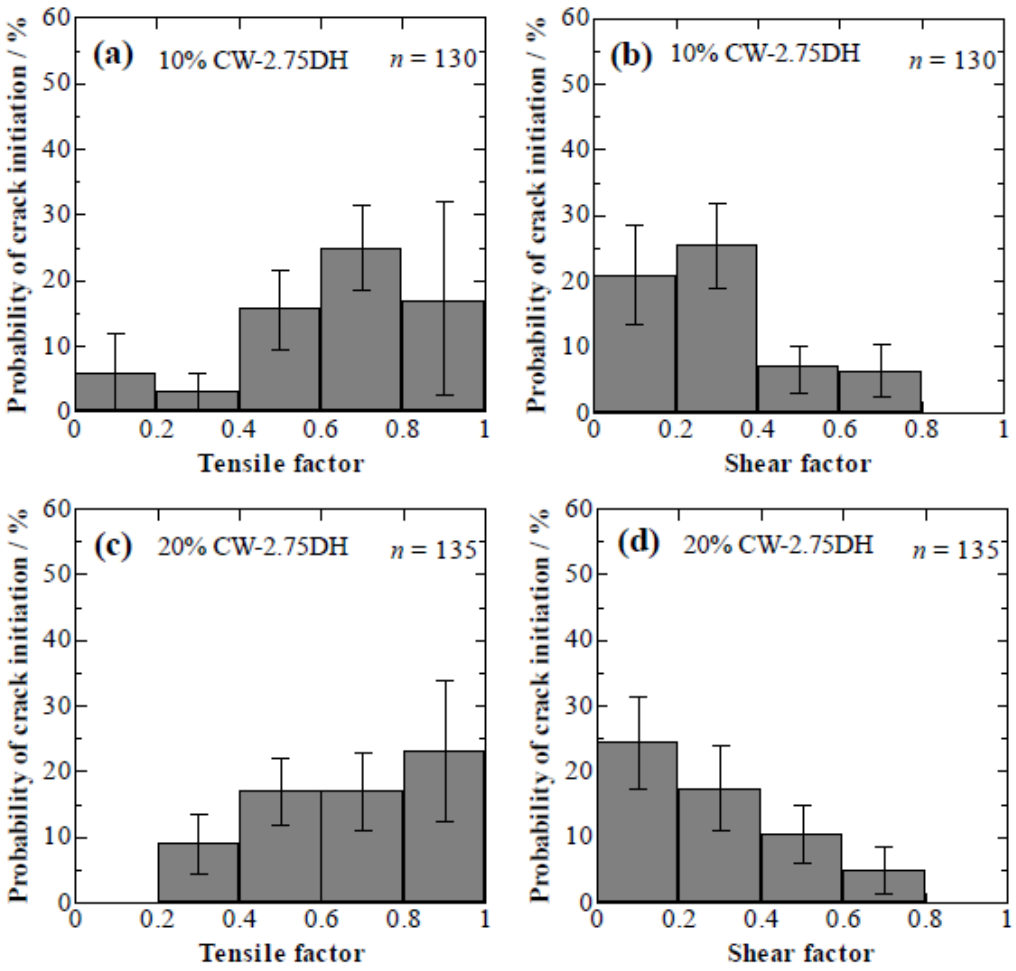

Fig. 3-6 Distributions on the probability of crack initiation against different factors operating at grain boundary for (a), (b) 10%CW specimen and (c), (d) 20%CW specimen. Error bars indicate the width of standard deviation.

3.4 Discussion

In the present study, the initiation of IGSCC on Alloy 600 in a simulated PWR water environment with a DH of 2.75 ppm and at 633 K is characterized. It is assumed that the tensile plastic deformation during the SSRT induces stress at the grain boundary, resulting in its cleavage. The induced stress at a grain boundary is resolved into local tensile, compressive, or shear stresses. It is confirmed that among these types of stresses, the

tensile stress mainly contributes to the cleaving of grain boundary, whereas the compressive stress never cause cleaving as described in **Fig. 3-5**. Furthermore, as shown in **Fig. 3-6**, the probability of crack initiation increases with increasing tensile stress. However, the relation between shear stress at grain boundary and the probability of crack initiation is not clear. These results indicate that tensile stress is more effective than shear stress in the cleaving of grain boundary. Conversely, the decreased probability at a higher range of shear factors might be attributed to the small tensile stresses operating at the grain boundaries. This is because shear stress tends to decrease with increasing tensile stress, as shown in **Fig. 3-5**. In order to discuss the grain boundary cleavage under shear deformation in grains, the motion of dislocations should be considered. Dislocation pile-up and annihilation at grain boundary due to shear deformation induce defects that might initiate grain boundary cracking. Therefore, micro-characterizations of slip deformation are required for further discussion. However, slip bands were not always visible at all grains examined: therefore, the actual slip deformation cannot be discussed in the present study.

The distributions of the tensile and shear stresses described in **Fig. 3-5** were summarized for one location of each specimen. The cracked boundaries obtained from 5 different locations for each specimen are plotted as stress distributions in **Fig. 3-7**. It was clarified that some Σ3 boundaries cracked when a relatively large tensile stress was operating. As apparent from **Fig. 3-7 (a)** and **(b)**, more Σ3 boundaries cracked than the other CSL boundaries although the probability of crack initiation on Σ3 boundaries was reported to be low compared with the other CSL boundaries[45, 53, 54]. This is attributed to the aforementioned findings that the number of CSL boundaries differs. As presented in Figure 3-1, most grain boundaries of specimens used in the present study were characterized as Σ3 boundary. Therefore, it may be rational to conclude that some Σ3

boundaries cracked only when a larger tensile stress was operated.

In the case of random boundaries, the number of crack initiation exhibits different trends depending on the degree of CW as shown in **Fig. 3-7(c)** and **(d)**. The number of cracks for the 10% CW specimen was the largest at around 40° and the number deceased with decreasing the misorientation angle to 20°, as well as increasing the angle to 60°. Chen et al. described that the grain boundary energy of the extended Read-Shockley model reached a maximum at a misorientation angle of 45°[55]. They reported that cracks mainly occurred at grain boundaries with a misorientation angle ranging from 30° to 45° because the grain boundaries with large grain boundary energy are more likely to crack. This is approximately in accordance with the present results obtained for the 10% CW specimen. In addition, **Fig. 3-7(c)** indicates that the crack initiation occurs even at grain boundaries out of the misorientation angle range indicated by Chen et al. when a larger tensile stress operates at the boundary. Conversely, as presented in **Fig. 3-7(d)**, the number of crack initiation for the 20% CW specimen was the largest at 50°. Although this sounds similar to the case of the 10% CW specimen, the misorientation angle dependence does not necessarily seem obvious for the 20% CW specimen. In general, CW introduces residual stress and strain in materials; therefore more strains are introduced in 20% CW specimens than in 10% CW specimens. **Figure 8** shows a kernel average misorientation (KAM) map for the 20% CW specimen, the corresponding SEM image of which was presented in **Fig. 3-2(c)**. In the figure, the arrows numbered 1 to 7 represent the locations of the cracked random boundaries, whereas those from 8 to 14 represent the locations of random boundaries without cracking (The numbers are also indicated in **Fig. 3-5(b)**).

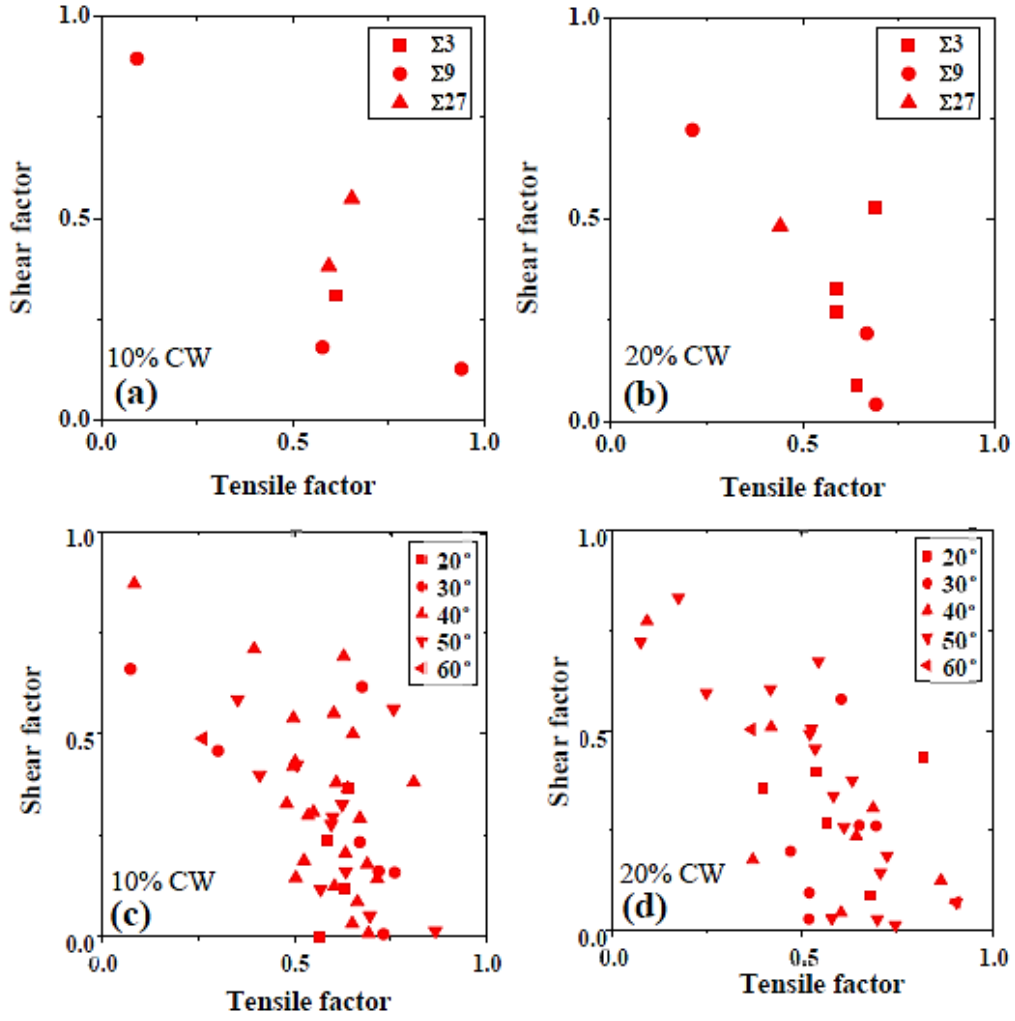

Fig. 3-7 Stress distribution at cracked (a), (b) CSL boundaries and (c), (d) random boundaries obtained for (a), (c) 10% CW and (b), (d) 20% CW specimens.

Figure 3-8 further show the locally concentrated strain along the grain boundaries and demonstrate that cracks initiate at the grain boundaries where a strong strain is present. This may imply that the strains introduced by CW induced crack initiation, whereas no cracks were observed at the grain boundaries without the concentrated strains, even if a large tensile or shear stress was operating. Therefore, it is confirmed that the crack initiation in 20% CW specimens is triggered not only by the stress operating at grain boundary but also by the strain concentrated at the grain boundary. It is well-known that

the local strains observed in the KAM map are directly linked to the local flow stress. Therefore, according to the aforementioned discussion, the grain boundaries where strong flow stress was generated roughly correspond to those where the calculated stresses are large. This indicates that the stress analysis proposed in the present work reflects the deformation behavior of the alloy examined although the calculations were carried out under several assumptions including homogeneous stress distribution within a single grain. As these assumptions might cause the result that the stresses operating at grain boundaries do not necessarily result in the crack initiation.

It has been widely accepted that IGSCC of Alloy 600 in the PWR primary water environment proceeds as internal oxidation along the grain boundary[8, 10, 11, 18, 56, 57]. A stress operating at a grain boundary can break the oxide at the grain boundary, resulting in the subsequent exposure of the underlying grain boundary to the environment. This induces crack initiation along the grain boundary. Furthermore, the grain boundary characteristics are reported to affect intergranular oxidation; oxidation proceeded at random grain boundaries, whereas it was suppressed at the CSL boundaries[58]. This difference in the degree of oxidation may be one reason for the probability distribution of crack initiation among various grain boundary characteristics other than the variation in stress operating at grain boundaries.

Based on the simple stress analysis introduced for the first time in this study, intergranular cracking can be categorized into two groups. In one group, the crack initiation depends on the stress distribution as well as the misorientation angle around the grain boundary; in the other case the crack initiation depended not only on the stress distribution but also on the strain concentrated around the grain boundary.

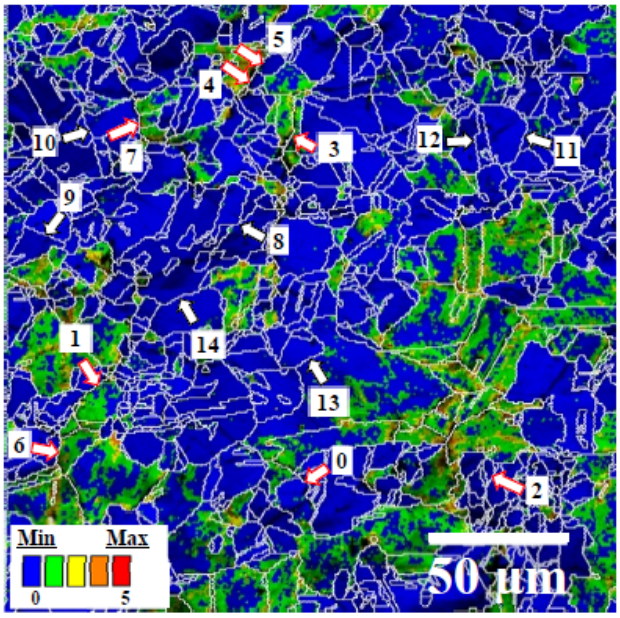

Fig. 3-8 Kernel Average Misorientation (KAM) obtained for 20%CW specimen after performing SSRT with the DH of 2.75 ppm, corresponding to the identical area shown in Figs. 2(d) and (d). The numbers correspond to the numbers in Figs. 2 (c) and 5 (b). Note that locations numbered as 0 – 7 cracked, and 8 – 14 not cracked.

3.5 Conclusion

In the present study, the author examined the crack initiation of Alloy 600 in a simulated PWR primary water environment with a DH concentration of 2.75 ppm and at 633 K. Tensile specimens subjected to CW with the reduction rates of 10% or 20% in advance were elongated up to a tensile strain of 10% in a slow strain rate testing (SSRT), and the strain was maintained for 50 h. The surface of the specimen was micro-crystallographically examined.

Many IGSCCs were observed on the surface of the specimen after SSRT and were characterized using a FE-SEM / EBSD. The stresses operating at the grain boundaries between two adjacent grains during the SSRTs were analyzed to resolve tensile,

compressive, and shear stresses, assuming that the primary slip system was active, and that slip deformation in two adjacent grains generated stress at their common grain boundary. It is confirmed that IGSCC preferentially occurred at the grain boundary with a larger tensile stress, which contributed to the cleaving of the grain boundary. No cracks were observed at the grain boundaries with compressive stress. Furthermore, crack initiation also depends on the degree of strain concentration, which was characterized by kernel average misorientation at the grain boundary for the 20% CW specimen.

References

1) F. Cattant, D. Crusset, D. Féron, Mater. Today. 11 (2008) 32–37.

2) S.S. Hwang, Y.S. Lim, S.W. Kim, D.J. Kim, H.P. Kim, Nucl. Eng. Technol. 45 (2013) 73–80.

3) F. Scenini, R.C. Newman, R.A. Cottis, R.J. Jacko, Corrosion. 64 (2008) 824–835.

4) T. Allen, J. Busby, M. Meyer, D. Petti, Mater. Today. 13 (2010) 14–23.

5) S.J. Zinkle, G.S. Was, Materials challenges in nuclear energy, Acta Mater. 61 (2013) 735–758.

6) G.P. Airey, "Optimization of Metallurgical Variables to Improve the Stress Corrosion Resistance of Inconel 600" EPRI report, NP-1354 (1980).

7) S.M. Bruemmer, G.S. Was, J. Nucl. Mater. 216 (1994) 348–363.

8) K. Arioka, Corrosion 71 (2015) 403-419.

9) Z. Zhai, M.B. Toloczko, M. J. Olszta, S.M. Bruemmer, Corros. Sci. 123 (2017) 76-87.

10) P.M. Scott, P. Combrade, J. Nucl. Mater. 524 (2019) 340-375.

11) P.M. Scott, "An Overview of Internal Oxidation as a Possible Explanation of Intergranular Stress Corrosion Cracking of Alloy 600 in PWRS," in Proc. 9th Int. Conf. on Environmental Degradation of Materials in Nuclear Power Systems–Water Reactors, eds. F.P. Ford, S.M. Bruemmer, G.S. Was (Pittsburgh, PA: The Minerals, Metals, and Materials Society, 1999), p. 3–14.

12) T.S. Gendron, P.M. Scott, S.M. Bruemmer, L.E. Thomas, "Internal Oxidation as a Mechanism for Steam Generator Tube Degradation", in Proc. Third Int. Steam Gener. Heat Exch. Conf. (1998) 389–406.

13) F. Lecoester, J. Chêne, D. Noel, Mater. Sci. Eng. A 262 (1999) 173–183.

14) J. Chêne, A.M. Brass, Metall. Mater. Trans. A 35 (2004) 457–464.

15) P.D. Hicks, C.J. Altstetter, Metall. Trans. A 21 (1990) 365–372.

16) P.D. Hicks,C.J. Altstetter, Metall. Trans. A 23 (1992) 237–249.

17) L.L iu, C. Zhai, C. Lu, W. Ding, A. Hirose, K.F. Kobayashi, Corros. Sci. 47 (2005) 355–367.

18) P.L. Andresen, F. Peter Ford, Mater. Sci. Eng. 103 (1988) 167–184.

19) M.M. Hall, Corros. Sci. 51 (2009) 1103–1106.

20) M.M. Hall, Corros. Sci. 51 (2009) 225–233.

21) W.L. Clarke, G.M. Gordon, Corrosion. 29 (1973) 1–12.

22) S.M. Bruemmer, L.A. Charlot, C.H. Henager, Corrosion. 44 (1988) 782–788.

23) Y.S. Lim, H.P. Kim, S.S. Hwang, J. Nucl. Mater. 440 (2013) 46–54.

24) T. Magnin, D. Noël, R. Rios, Mater. Sci. Eng. A. 177 (1994) 11–14.

25) W.C. Moshier, C.M. Brown, Corrosion. 56 (2000) 307–320.

26) S. Yamazaki, Z. Lu, Y. Ito, Y. Takeda, T. Shoji, Corros. Sci. 50 (2008) 835–846.

27) J. Hou, Q.J. Peng, Z.P. Lu, T. Shoji, J.Q. Wang, E.H. Han, W. Ke, Corros. Sci. 53 (2011) 1137–1142.

28) H. Takiguchi, M. Ullberg, S. Uchida, J. Nucl. Sci. Technol. 41 (2004) 601–609.

29) T. Nakagawa, N. Totsuka, T. Terachi, N. Nakajima, J. Nucl. Sci. Technol. 40 (2003) 39–43.

30) D.S. Morton, S.A. Attanasio, E. Richey, G.A. Young, Proceedings of the 12th International Conference on Environmental Degradation of Materials in Nuclear Power System – Water Reactor – (2005).

31) R.N. Parkins, Jom. 44 (1992) 12–19.

32) T. Shibata, Iron Steel Inst. Japan. 31 (1991) 115–121.

33) G. Palumbo, P.J. King, K.T. Aust, U. Erb, P.C. Lichtenberger, Scr. Metall. Mater. 25 (1991) 1775–1780.

34) K.T. Aust, U. Erb, G. Palumbo, Mater. Sci. Eng. A. 176 (1994) 329–334.

35) B. Alexandreanu, G.S. Was, Corrosion. 59 (2003) 705–720.

36) V.Y. Gertsman, S.M. Bruemmer, Acta Mater. 49 (2001) 1589–1598.

37) D.C. Crawford, G.S. Was, Metall. Trans. A 23 (1992) 1195–1206.

38) G. Bertali, F. Scenini, M.G. Burke, Corros. Sci. 111 (2016) 494-507.

39) G. Bertali, F. Scenini, M.G. Burke, Corros. Sci. 100 (2015) 474-483.

40) C.J. O'Brien, S.M. Foiles, Philos. Mag. 96 (2016) 1463-1484.

41) M. Seita, J.P. Hanson, S. Gradečak, M.J. Demkowicz, Nat. Commun. 6 (2015) 6164.

42) S. Bechtle, M. Kumar, B.P. Somerday, M.E. Launey, R.O. Ritchie, Acta Mater. 57 (2009) 4148-4157.

43) M. Seita, J.P. Hanson, S. Gradečak, M.J. Demkowicz, J. Mater. Sci. 52 (2017) 2763-2779.

44) S. Fujimoto, M. Mochizuki, Y. Morita, Y. Mikami, H. Tsuchiya, and K. Nishimoto, "Crystallographical Characterization of Initiation of Intergranular Stress Corrosion Cracking of Alloy 600 in PWR Environment", in Proc. Fifteenth Int. Conf. Environ. Degrad. Mater. Nucl. Power Syst. - Water React., (2011) 1685-1696.

45) K.T. Jung, H. Tsuchiya, S. Fujimoto, Mater. Trans. 61 (2020) 1339-1345.

46) K.-T. Jung, T. Ogawa, Y. Morita, S. Fujimoto, "Grain Boundary Characterization for Initial Stage of IGSCC of Alloy 600 in PWR Primary Water Environment", in Proc. Seventeenth Int. Conf. Environ. Degrad. Mater. Nucl. Power Syst. - Water React., (2015) 895-903.

47) P.L. Andresen, J. Hickling, A. Ahluwalia, J. Wilson, Corrosion 64 (2008) 707-720.

48) R.A. Etien, E. Richey, D. S. Morton, J. Eager, "SCC Initiation Testing of Alloy 600 in High Temperature Water", in Proc. 15th Int. Conf. Environ. Degrad. Mater. Nucl. Power Syst. - Water React., (2011) 2274-2284.

49) T. Moss, G.S. Was, J. Electrochem. Soc. 162 (2015) C35-C41.

50) E. Rickey, D.S. Morton, R.A. Etien, “SCC Initiation Testing of Alloy 600in High Temperature Water”, in Proc. 13rd Int. Conf. Environ. Degrad. Mater. Nucl. Power Syst. - Water React., (2007) 831-850.

51) S. Fujimoto, W.-S. Kim, M. Sato, J.-S. Son, M. Machida, K.-T. Jung, H. Tsuchiya, J. Solid State Electrochem. 19 (2015) 3521–3531.

52) G.I. Tylor, J. Inst. Met. 62 (1938) 307-324.

53) Z.-P. Lu, T. Shoji, S. Yamazaki, K. Ogawa, Corros. Sci. (2013) 211-228.

54) N. Sakaguchi, Y. Ohguchi, T. Shibayama, S. Watanabe, H. Kinoshita, J. Nucl. Mater. 432 (2013) 23-27.

55) J.Q. Chen, H. Lu, W. Cui, J.M. Chen, Y.F. Huang, Mater. Sci. Technol. 30 (2014) 1189–1196.

56) K. Arioka, T. Yamada, T. Miyamoto, M. Aoki, Corrosion 70 (2014) 695–707.

57) P.M. Scott, M. Le Calvar, “Some Possible Mechanisms of Intergranular Stress Corrosion Cracking of Alloy 600 in PWR Primary Water,” Proc. 6th Int. Conf. on Environmental Degradation of Materials in Nuclear Power Systems–Water Reactors, ed. E.P. Simonen, held 1993 (Warrendale, PA: The Minerals, Metals, and Materials Society, 1993) 657–665.

58) Y.-S. Lim, S.-W. Kim, S.-S. Hwang, H.P. Kim, C. Jang, Corros. Sci. 108 (2016): 125-133.

Chapter 4 Three-dimensional crystallographic characterization of IGSCC crack of Alloy 600 in simulated PWR environment

4.1 Introduction

One of the most important issues in nuclear industry is to prevent degradation of the materials composing nuclear reactors. Since Coriou reported that the intergranular stress corrosion cracking (IGSCC) occurred on Alloy 600 in caustic environment, extensive studies have been conducted to clarify the IGSCC mechanism on Ni-Cr alloys used as structural components and steam generator tubes in primary water environments of pressurized water reactor (PWR)[1-8]. Despite of the efforts, the mechanism remains still unclear. It is recognized that the IGSCC in PWR primary water environment is affected by various factors such as dissolved hydrogen concentration, cold work, temperature of the environment, stress and grain boundary characteristic[5, 7, 9-18]. Among these factors, the grain boundary characteristics are in IGSCC as cracks initiate and propagate along on grain boundary. Therefore, a variety of analytical techniques such as scanning electron microscopy (SEM), transmission electron microscopy (TEM), Auger electron spectroscopy (AES), energy-dispersive X-ray spectroscopy (EDS) and secondary ion mass spectrometry (SIMS) have been used to understand the crack initiation and propagation in IGSCC on Alloy 600 from metallic structure view[1, 2, 4-6, 10-12, 19-25].

Grain boundary is categorized as high angle grain boundary with the misorientation angle more than 15 º or low angle grain boundary with the misorientation angle less than 15 º. Furthermore, the high angle grain boundary is also categorized as random boundary or coincidence site lattice (CSL) boundary. It is well-known that CSL boundary exhibits higher resistance to IGSCC due to high fraction of atomic sites common to both crystal lattice orientations of adjacent grains[26-29]. That is, the crack susceptibility is lower on CSL

boundary than random boundary as the author also previously presented[30]. Furthermore, the crack susceptibility was affected by the misorientation angle. These results clearly demonstrate that the grain boundary characteristics are one of the important factors to govern IGSCC. Although IGSCC cracks initiate and propagate along grain boundary, abovementioned analysis does not include a characterization on grain boundary plane. In order to consider grain boundary characteristics, angles between the direction of stress applied to tensile specimen and the direction of grain boundary are required at the surface and of at the cross-section.

In the present chapter, the author performed a top-view and cross-sectional EBSD characterization of Alloy 600 subjected to IGSCC and examined the effects of characteristics of grain boundary plane along the crack initiation.

4.2 Experimental

A mill-annealed Alloy 600 sheet was cold-worked with the reduction ratio of 10% or 20%. Tensile specimens were cut from the sheet by an electric discharge machine. The tensile specimens were ground by SiC waterproof abrasive papers up to #2000 and then polished with diamond paste of 9 -μm and 1/4 -μm. Finally, the surface of the specimens was polished with a colloidal silica suspension for 20 min. Following the polishing processes, the specimens were ultrasonically cleaned with acetone, ethanol and deionized water for 5 min. successively. A slow strain rate test (SSRT) was performed for the tensile specimens in a simulated PWR primary water environment. H_3BO_3 and LiOH were used to prepare the simulated PWR primary water containing B of 500 ppm and Li of 2 ppm. The simulated primary water was deaerated before the SSRT for 48 hours to control the dissolved oxygen concentration less than 1 ppb and then the dissolved hydrogen concentration was set at 0.5 ppm or 2.75 ppm. An SSRT were performed at the

temperatures of 593 K and 633 K under the pressure of 20 MPa. In the environments, the specimens were elongated up to 10 % with the strain rate of 5×10^{-7} s^{-1}, and then the strain was maintained for 50 hours. Specimens examined and SSRT conditions are summarized in **Table 4-1**. Hereafter, specimens are abbreviated by using variables in this study, that is, the ratio of cold work, the temperature and dissolved hydrogen concentration in an SSRT as listed in **Table 4-1**.

Table 4-1 Conditions of experimental specimens and SSRT

Cold work, %	SSRT				Sample abbreviation
	Dissolved hydrogen, ppm	Temperature, K	Elongation, %	Holding time, h	
10	0.5	593	10	50	10CW-0.5DH-593K
20					20CW-0.5DH-593K
10	2.75				10CW-2.75DH-593K
20					20CW-2.75DH-593K
10	0.5	633			10CW-0.5DH-633K
20					20CW-0.5DH-633K
10	2.75				10CW-2.75DH-633K
20					10CW-2.75DH-633K

Following the SSRT, oxide films and corrosion products formed on the surface of the specimens during the SSRT were removed by Ar^+ ion sputtering. In order to carry out the three-dimensional characterization of the specimens, the gauge section of the specimen was cut along the dotted lines as shown in **Fig. 4-1**. Cross-sections of the specimen after the cutting were polished with the same procedure previously mentioned. The

cross-sections were observed with SEM and some locations within the identical area to the SEM observation were characterized with EBSD.

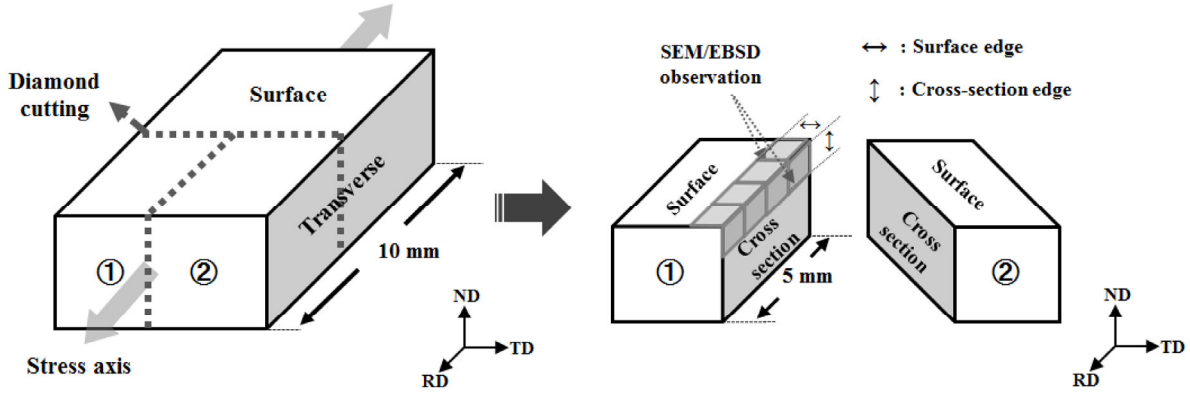

Fig. 4-1 Sample preparations for crystallographic analysis by EBSD on the cracks during IGSCC initiation.

4.3 Results

Figure 4-2 shows SEM images of the specimen surfaces after SSRT performed under the various conditions listed in **Table 4-1**. As apparent, cracks initiated on the all specimens, but the number of initiated crack was considerably small on the specimens subjected to the SSRT at 593 K. As previously mentioned, in this study, initiated cracks were also observed and characterized at the cross-section of gauge section of tensile specimens. A typical result of the cross-sectional observation of a crack is presented in **Fig. 4-3(a)**. In the image, one crack is visible not only at the cross-section but also at the surface of the gauge section, that is, one can see how the crack propagated into the specimen along a grain boundary. Similar observations were conducted for 5 mm of the side edge of all the prepared specimens as illustrated in **Fig. 4-1**.

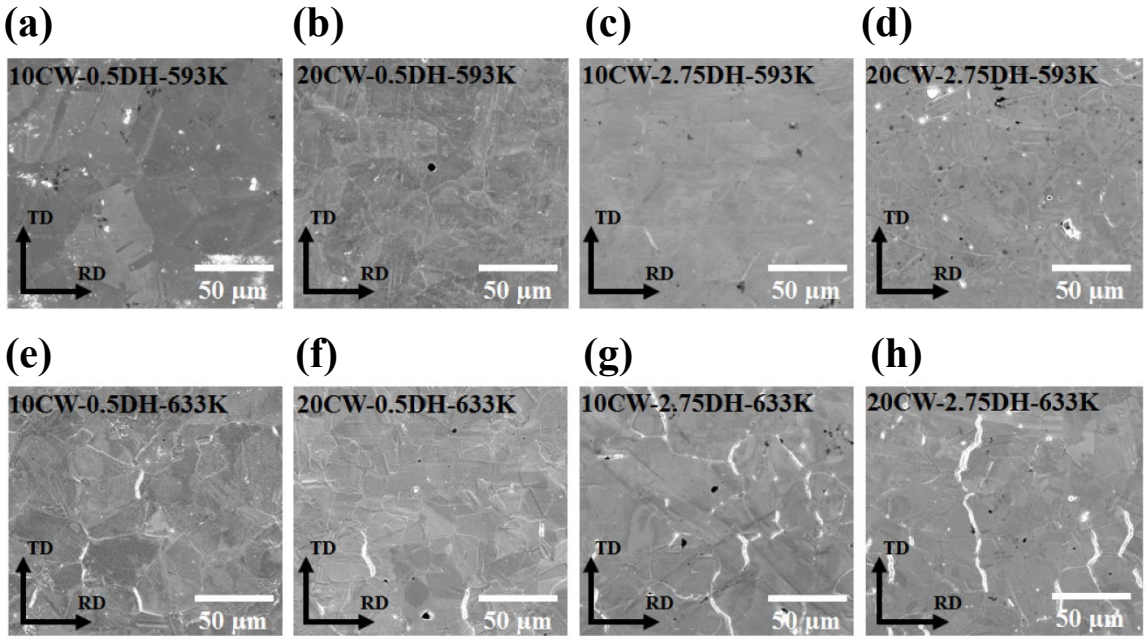

Fig. 4-2 SEM images of the Alloy 600 surface after the SSRT in the simulated PWR environment at (a-d) 593 K and (e-h) 633 K ; (a, e) 10CW-0.5DH, (b, f) 20CW-0.5DH, (c, g) 10CW-2.75DH and (d, h) 20CW-2.75DH. The stress axis is parallel to the rolling direction (RD).

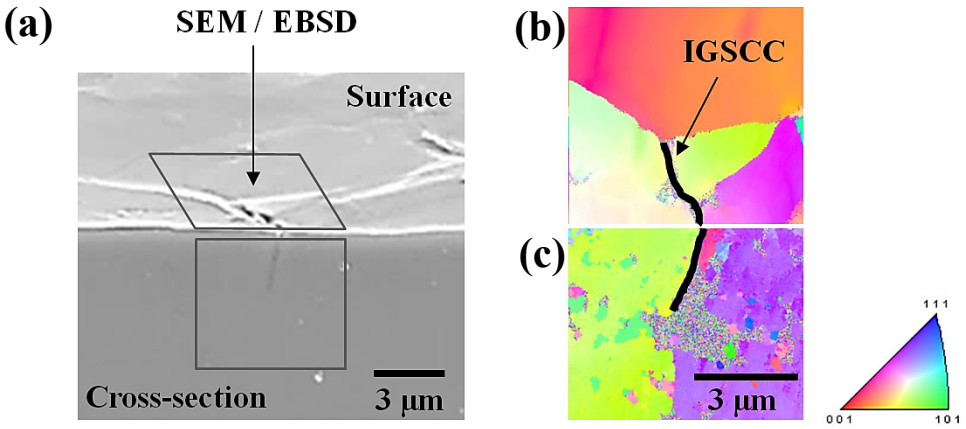

Fig. 4-3 (a) SEM image of the 10CW-2.75DH-633K after the SSRT and (b), (c) IPF map obtained with EBSD on specimen surface and cross-section as identical locations of (a).

From cross-sectional views of crack, the length of crack in the depth direction as well as the number of crack were evaluated and summarized in **Fig. 4-4**. The images clearly show that less crack formed at 593 K compared to those at 633 K and the cracks formed at 593 K were shorter. Furthermore, the dissolved hydrogen concentration affected the number and length of cracks. In the case of the dissolved hydrogen concentration of 0.5 ppm, cracks were relatively fewer compared to the case of the hydrogen concentration of 2.75 ppm as apparent from **Fig. 4-4**. As the author found that the probability of crack initiation in IGSCC depended on grain boundary characteristics[30], the crystallographic characterization of crack was conducted. As Parkins and Shibata pointed out[31, 32], the crack initiation and propagation are stochastic event. Therefore, a large number of cracks should be discussed. In the present study, cracks formed during an SSRT at 633 K in the simulated PWR environment with the hydrogen concentration of 2.75 ppm were analyzed, because cracks on the specimens subjected to the SSRT at 593 K and/or with the hydrogen concentration of 0.5 ppm were significantly few.

Figures 4-3(b) and **(c)** show an inverse pole figure (IPF) maps obtained around the crack shown in **Fig. 4-3(a)**. By overlapping the SEM image to the IPF maps, one can confirm that the crack initiated along a grain boundary. Based on the EBSD observation, cracked grains were characterized. In this study, the probability of crack initiation was defined as the ratio of the number of cracked grains to the total number of grains within certain range of analysis.

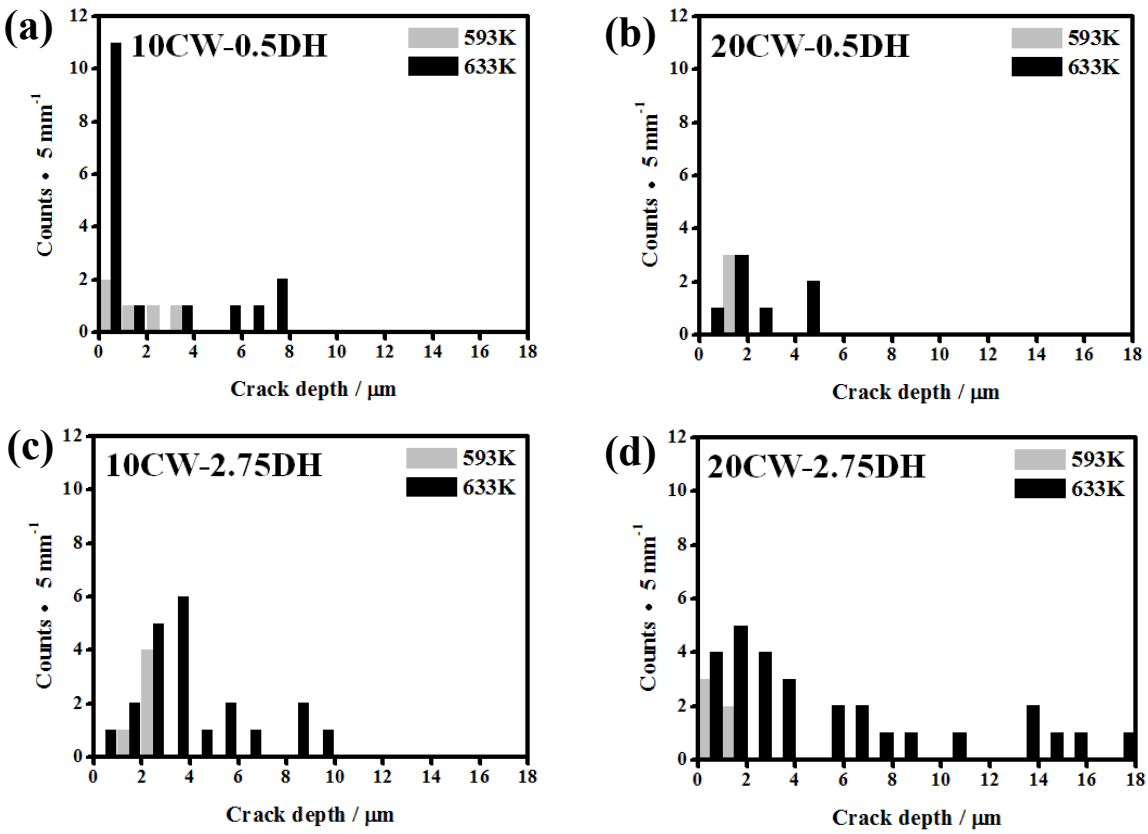

Fig. 4-4 Crack depth profile observed at cross-section of Alloy 600 after the SSRT in the simulated PWR environment at 593 K and 633 K; (a) 10CW-0.5DH, (b) 20CW-0.5DH, (c) 10CW-2.75DH and (d) 20CW-2.75DH.

Figure 4-5(a) shows the probability of crack initiation analyzed on the cross-sections of the 10% and 20% CW specimens that were subjected to an SSRT at 633 K with dissolved hydrogen concentrations of 2.75 ppm. The probability was evaluated with respect to misorientation angle between two adjacent grains. The probability distribution obtained from the corresponding positions of the top surfaces is also presented in **Fig. 4-5(b)**. The probability of crack initiation was higher at the misorientation angle ranging from 30 º to 40 º and equaled zero near the misorientation angle of 60 º on 10% CW specimen as well as 20% CW specimen, indicating that no cracks initiated on grain

boundaries with misorientation angle close to 60 º on both specimens. The probability distributions were similar for the 10% CW and the 20% CW specimens. Furthermore, a similar trend was obtained in the distribution of the probability between analysis conducted on the cross-section and on the top surface at identical locations. These results indicate that the crystallographic characterization of crack can be performed properly on cross-sections of gauge section of tensile specimen.

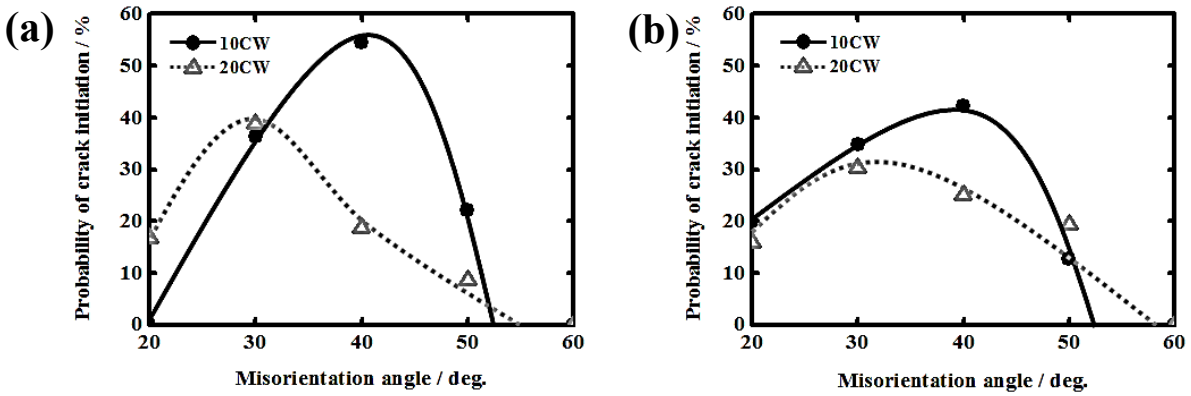

Fig. 4-5 Probability of crack initiation obtained at (a) cross-section and (b) surface of specimens calculated for grain boundary against various misorientation angle ranges estimated with EBSD; Dissolved hydrogen concentration was 2.75 ppm.

The crack initiation of IGSCC on Alloy 600 in simulated PWR primary water environments has been examined in terms of misorientation angle for two adjacent grains. In the following, the crack initiation is discussed, based on the inclination on a grain boundary plane. The inclination on a grain boundary plane was calculated through the following steps. For the calculation, a grain boundary plane tilted between two grains is considered as illustrated in **Fig. 4-6**. In the model, α presents the angle between the grain boundary plane and stress axis at the specimen surface while the corresponding angle at the

cross-section is defined as β.

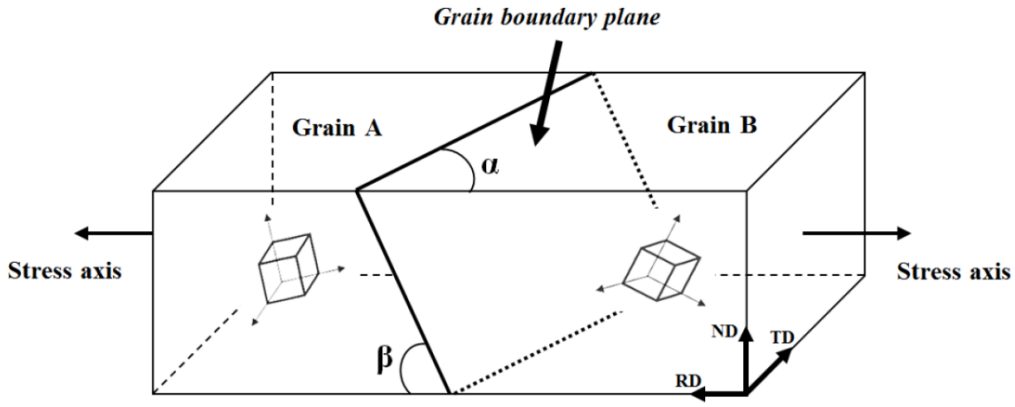

Fig. 4-6 Schematic illustrations for the inclination angle of the grain boundary plane.

The Euler angles for each grain are denoted by (φ, θ, ψ) from EBSD[33]. Assuming that the principal axes of the crystal coordinate system are arranged (φ, θ, ψ), the rotation matrix, R_i, can be expressed in the following equation (4-1) [34-36].

$$R_i = \begin{pmatrix} \cos\varphi\cos\psi - \sin\varphi\sin\psi\cos\theta & \sin\psi\cos\varphi + \cos\theta\sin\varphi\sin\psi & \sin\varphi\sin\theta \\ -\cos\psi\sin\varphi - \sin\psi\cos\varphi\cos\theta & -\sin\varphi\sin\psi + \cos\varphi\cos\psi\cos\theta & \cos\varphi\sin\theta \\ \sin\psi\sin\theta & -\cos\psi\sin\theta & \cos\theta \end{pmatrix} \quad i = \text{A or B} \quad (4\text{-}1)$$

Misorientation between the adjacent grains, that are grain A and grain B shown in **Fig. 4-6**, is calculated in the following equation (4-2) by using the rotation matrix of grain A, R_A and the rotation matrix of grain B, R_B.

$$R = R_B \cdot R_A^{-1} \quad (4\text{-}2)$$

Where R_A^{-1} is the inverse matrix of R_A. From components of the matrix R, the rotation angle of the inclination and the direction of the rotation axis are calculated.

However, in order to determine an inclination angle on the grain boundary plane, the difference between the direction of the rotation axis and the normal direction to the grain boundary plane should be calibrated. To calculate the crystallographic inclination angle on the grain boundary plane, it is necessary to calculate the space indices for the grain boundary plane as proposed by Randle[37-39].

$V_\alpha = (\cos\alpha, \sin\alpha, 0), \quad V_\beta = (\cos\beta, 0, \sin\beta)$ (4-3)

The coordinates of direction to the grain boundary plane can be estimated by using the two angles of α and β. The rotation matrix corresponding to the grain boundary plane is expressed in the following equation (4-4).

$$R_c = \begin{pmatrix} \cos\varphi'\cos\psi' - \sin\varphi'\sin\psi'\cos\theta' & \sin\psi'\cos\varphi' + \cos\theta'\sin\varphi'\sin\psi' & \sin\varphi'\sin\theta' \\ -\cos\psi'\sin\varphi' - \sin\psi'\cos\varphi'\cos\theta' & -\sin\varphi'\sin\psi' + \cos\varphi'\cos\psi'\cos\theta' & \cos\varphi'\sin\theta' \\ \sin\psi'\sin\theta' & -\cos\psi'\sin\theta' & \cos\theta' \end{pmatrix}$$ (4-4)

Assuming that the transformation matrix from the direction of the rotation axis to the normal direction on the grain boundary plane is expressed as R_c, the matrix, R_{gbp} between three direction of the modified rotation matrix based on equations (4-1) and (4-4) can be modified to the equation (4-5).

$$R_{gbp} = R_B \cdot R_A^{-1} \cdot R_C = \begin{pmatrix} r_{11} & r_{12} & r_{13} \\ r_{21} & r_{22} & r_{23} \\ r_{31} & r_{32} & r_{33} \end{pmatrix}$$ (4-5)

In order to compute the angle from the R_{gbp} rotation matrix, the rotation formula was used that indicates the sum of the diagonal elements of the rotation matrix[34-36, 40].

$$2\cos\theta + 1 = (r_{11} + r_{22} + r_{33}) \quad (4\text{-}6)$$

The formula is an efficient algorithm which rotates a vector in a space given its axis and rotation angle. By expanding to a three-dimensional space, the vector corresponding to the given axis can be transformed to calculate the angular representation. It is widely cited for obtaining useful information in a rotation matrix of a three-dimensional rotation matrix. Based on the equations (4-5) and (4-6), the inclination angle of grain boundary plane is calculated from the following equation (4-7).

$$\theta_C'' = cos^{-1}(r_{11} + r_{22} + r_{33} - 1)/2 \quad (4\text{-}7)$$

The crack susceptibility is summarized in terms of the inclination angle on grain boundary plane as well as the misorientaiton angle and is presented in **Fig. 4-7**. In the figure, solid squares and open circles present cracked and non-cracked grain boundaries, respectively. Both specimens showed that cracked grain boundaries were located on the range of misorientation angle from 30 º to 50 º as previously shown in **Fig. 4-5**. On the other hand, the influence of the inclination angle on the crack initiation was different, depending on the degree of cold work applied before SSRT. On 10% CW specimen, the cracked grain boundaries are concentrated between 30 º and 50 º. By contrast, in the case of 20% CW specimen, cracks were located on the wide range of the inclination angle from 5 º to 85 º. The distribution of crack depth was also summarized and shown in **Fig. 4-8** in terms of the inclination angle. It was found that deepest crack distributed around the

inclination angle of approximately 40 º for the both specimens.

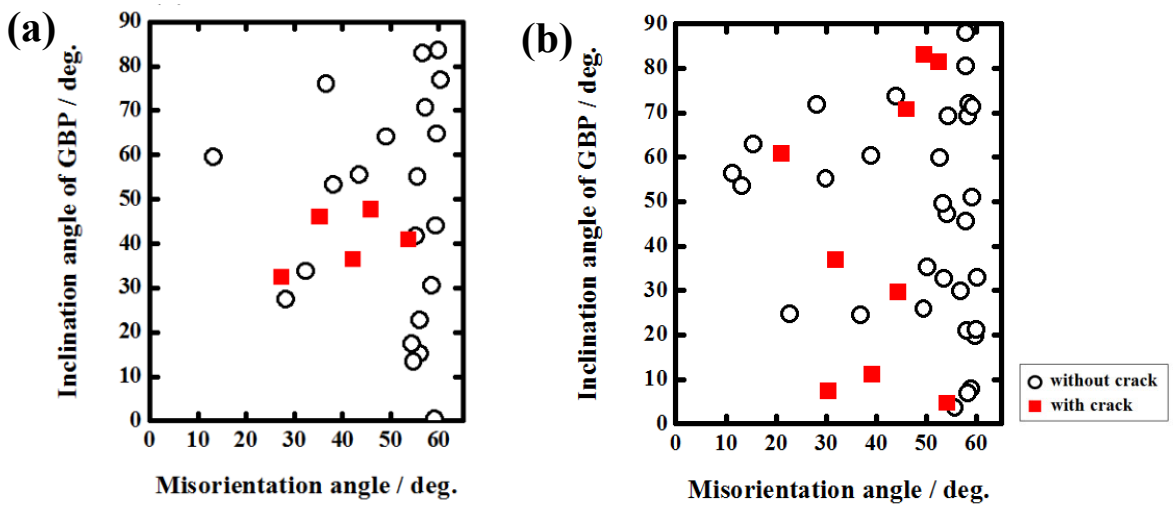

Fig. 4-7 Relationship of crack initiation on the misorientation angle and inclination angle of grain boundary plane with or without crack. The circle represent the grain boundaries without crack and solid mark represent the grain boundaries with crack; (a) 10CW-2.75DH, (b) 20CW-2.75DH specimens.

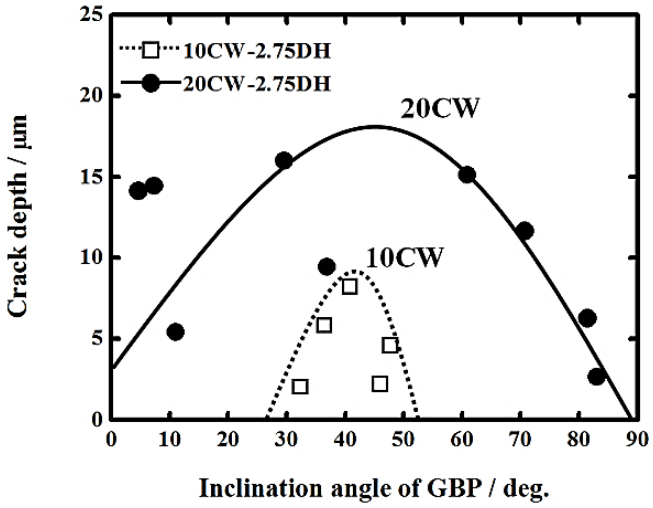

Fig. 4-8 Crack depth as a function of inclination angle of grain boundary plane for the 10%

and 20% cold-worked specimens after SSRT in 2.75 DH.

Stress direction applied to a grain boundary is also one of the important factors that affect crack initiation. **Figure 4-9** shows the schematic illustrations of stress angles, α and β, in the surface and cross section, respectively as represented in **Fig. 4-6**. The stress angle is defined as the angle between the grain boundary and the stress axis. Crack susceptibility is shown in **Fig. 4-10** as a function of the stress angles on grain boundary and also inclination angle and misorientation angle. On 10% CW specimen, cracks initiated at grain boundaries with stress angles over 60 º on the surface as well as on the cross-section. On 20% CW specimen, by contrast, although cracks initiated at grain boundaries with stress angles on the surface, α, over 60 º as similar to 10% CW specimen, cracks were observed at grain boundaries with stress angles from the cross section, β, greater than 40 º. This means that, the crack propagation occurred on 20% CW specimen even at lower stress angle, meaning that cracks are able to grow more easily on 20% CW specimen. This result is in accordance with the findings shown in **Fig. 4-4** where longer cracks were observed on 20% CW specimen compared to 10% CW specimen. **Figure 4-11** shows the schematic illustrations of crack initiation at grain boundary due to tensile or shear stresses. **In Figs. 4-10**, the cracks mainly initiated or propagated by tensile stress as shown in **Fig. 4-11(a)**. However, the crack initiation of 20% CW in which cracks grows easily at even lower stress angle also suggests the possibility of cracking due to shear stress at the grain boundaries as shown in **Fig. 4-11(b)**.

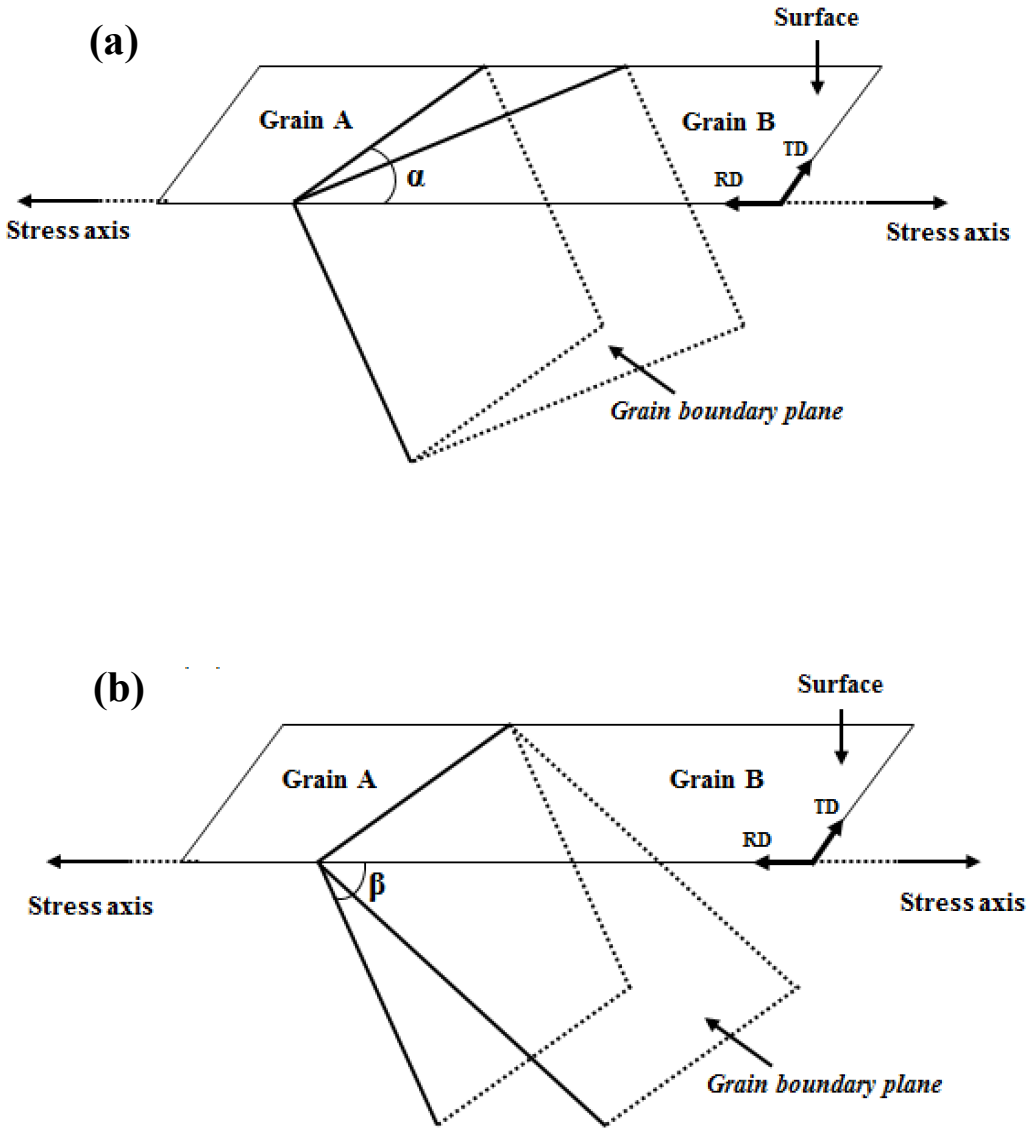

Fig. 4-9 Crack depth as a function of inclination angle of grain boundary plane for the 10% and 20% cold-worked specimens after SSRT in 2.75 DH.

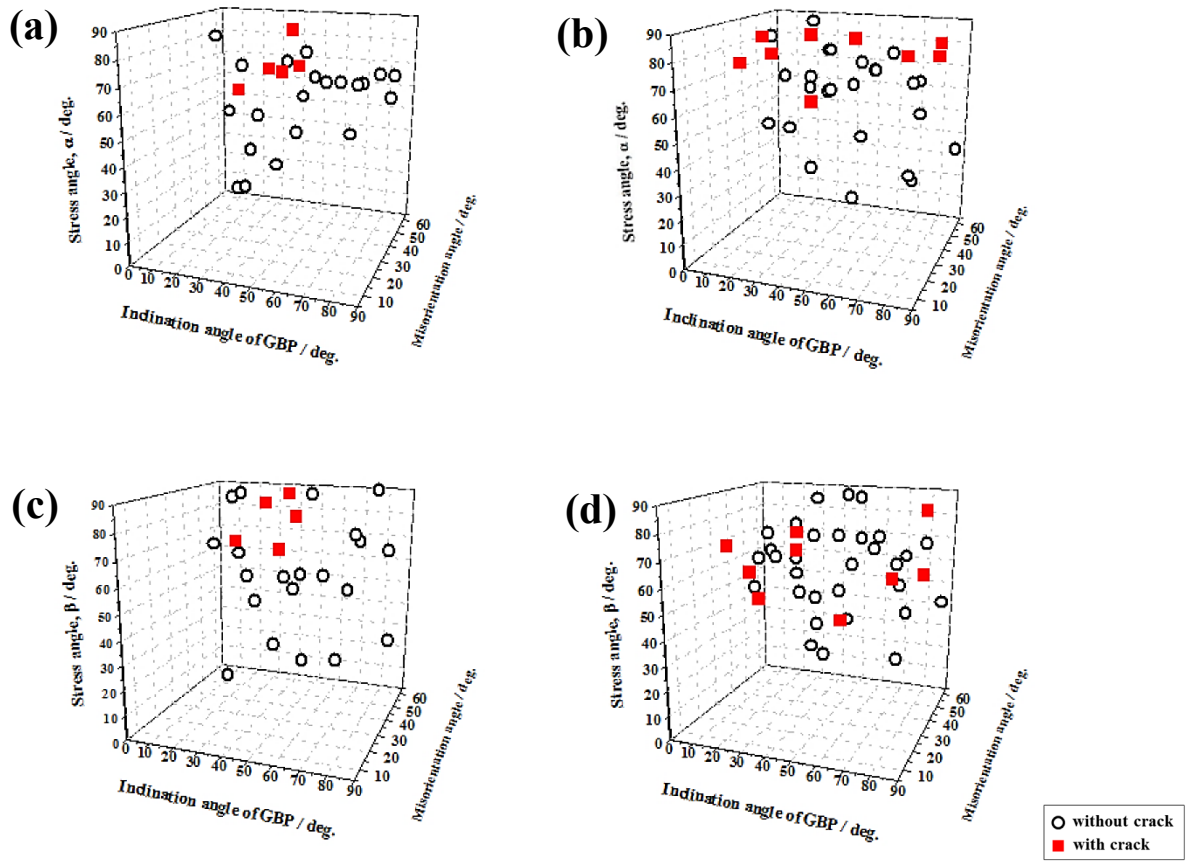

Fig. 4-10 Stress angle as a function of misorienatiaon angle and the inclination angle of the grain boundary plane with or without cracks; the stress angle of (a) 10CW-2.75DH and (b) 20CW-2.75DH was analyzed at surface. And also, the stress angle of (c) 10CW-2.75DH and (d) 20CW-2.75DH was analyzed at cross-section.

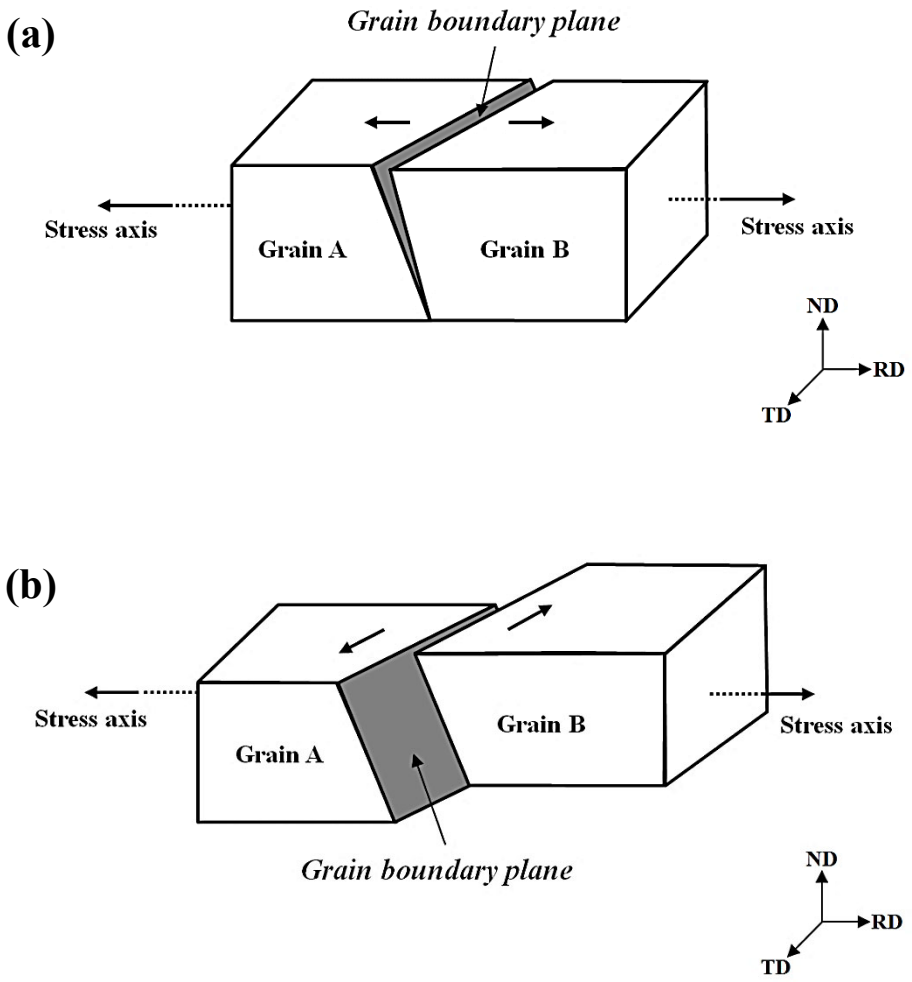

Fig. 4-11 Schematic illustrations of crack initiation at grain boundary plane due to tensile or shear stresses.

4.4 Discussion

4.4.1 Change in depth of cracks induced by dissolved hydrogen and cold work

In this study, as shown in **Fig. 4-4**, it was revealed that the large number of crack and the larger crack length were attained for the larger dissolved hydrogen concentration in the simulated primary side PWR environment at 633 K. In addition, the number and the length

of crack on 20 % CW specimen is larger than that on 10 % CW.

In the followings, effects of the dissolved hydrogen and the cold work on the crack initiation are discussed. The dissolved hydrogen is found to affect the formation of oxide films on Alloy 600 in primary water environment. Fujimoto et al. reported that stable Cr based films did not form on Alloy 600 in the PWR primary water environment with higher dissolved hydrogen concentration[41]. Surface oxide films are known to prevent IGSCC in primary water environment[11, 19, 42]. Therefore, the crack initiation was enhanced by increasing the dissolved hydrogen concentration in the environment. In addition, the enhanced crack initiation can be discussed in terms of the interaction between hydrogen and dislocation. Dissolved hydrogens play a role to decompose accumulated dislocations in Alloy 600[43, 44]. The decomposed dislocations accumulate at certain grain boundaries, contributing to the grain boundary deformation. This may also result in the enhanced crack initiation under the higher dissolved hydrogen condition.

Hou et al. investigated the strain concentration and grain boundary characteristics of cold-worked Alloy 600 in simulated primary water environment[14]. The highest crack growth rate and strain concentration at random boundaries were obtained in 20% cold-worked Alloy 600. The main deformation mode of 20% cold-worked Alloy 600 was reported to be the interaction of dislocation and slip, leading to non-uniform strain concentration. In order to confirm the strain distribution, the kernel average misorientation (KAM) on 10% CW and 20% CW specimens was analyzed after the SSRT, and was shown in **Fig. 4-12**. From the images, the higher and non-uniform strain concentration was confirmed on 20% CW Alloy 600 compared to 10% CW Alloy 600. The higher, non-uniform strain concentration at grain boundary may increase the crack susceptibility.

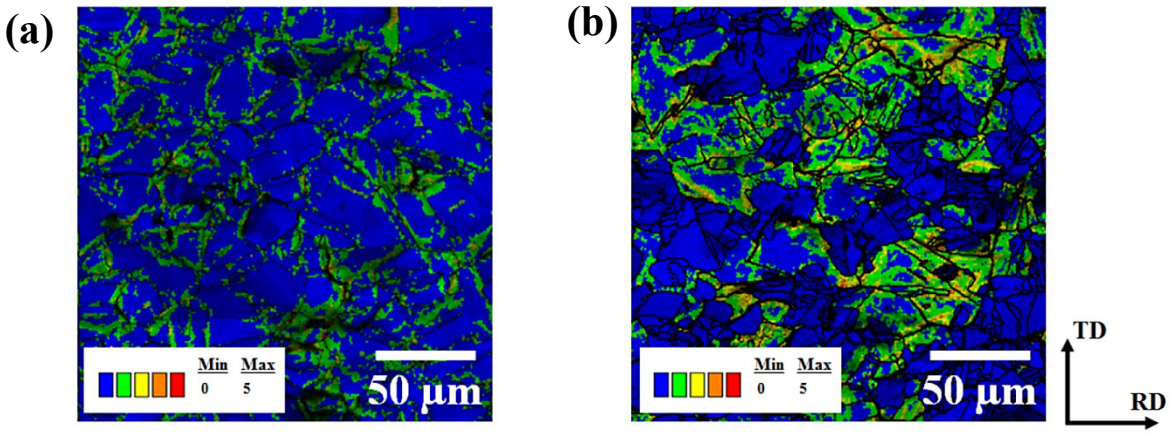

Fig. 4-12 Kernel average misorientation (KAM) maps of (a) 10 % and (b) 20 % cold worked Alloy 600 surface after the SSRT in the simulated PWR primary water environment with dissolved hydrogen concentration of 2.75 ppm. The stress axis is parallel to the rolling direction (RD).

4.4.2 Effects of misorientation angle on crack initiation

It has been reported that IGSCC in PWR primary water environments is affected by grain boundary characteristics both random and CSL boundaries[26-29, 45, 46]. CSL boundary possesses lower crack susceptibility compared to random boundary, especially Σ3 boundary exhibits excellent resistance to IGSCC. In this study, the higher crack susceptibility was observed at the misorientation angle ranging from 30 º to 40 º as shown in **Fig. 4-5**.

IGSCC susceptibility is correlated with grain boundary energy. Chen et al. was found that the grain boundary energy of extended Read-Shockley model reached to a maximum at 45 ˚ grain boundary[47]. For the grain boundaries having larger grain boundary energy

were preferentially separation, and it was expected that IGSCC was mainly initiated on the misorientation angle between 30 ˚ and 45 ˚. These results are clearly consistent with the results of present work on certain misorientation angle of around 40 ˚ which has highest crack susceptibility as shown in **Fig. 4-5**. Grain boundary sliding is also found to be related to the crack initiation. In general, high-angle grain boundary exhibits higher grain boundary mobility compared to low-angle grain boundary[48] Furthermore, the mobility of high-angle grain boundary depends greatly on the misorienation angle of the grain boundary[49, 50]. Titrov demonstrated the mobility of grain boundary is relatively fast in the misorientation angle range from 15 º to 45 º in f.c.c. and b.c.c. metals[51]. They also suggested that grain boundary migration could contribute to the grain boundary deformation which has been reported to correlate to IGSCC. Therefore, higher crack susceptibility was observed around the misorientation angle of certain range in this study.

4.4.3 Inclination angle on grain boundary plane and evaluation of crack susceptibility

The grain boundary characteristics greatly affect the IGSCC crack susceptibility. Although the grain boundaries geometrically possess a three-dimensional structure[34, 51, 52], but most study does not consider the grain boundary plane on IGSCC in Alloy 600. Therefore, three-dimensional crystallographic characterization of IGSCC on grain boundary plane was discussed. Randle notes that it is important to understand the crystallographic properties of fractures or cracks for non-exposed grain boundaries at cross-section[37]. He proposed an investigation methodology for crystallographic properties of non-exposed grain boundary plane using EBSD. Stratulat et al. conducted a study on the IGSCC in 304 austenitic stainless steels in hot water using three-dimensional data on grain boundary plane and crystal orientations[52]. They demonstrated that the intergranular structure and plastic deformation incompatibility combinedly contribute to crack initiation.

In the three-dimensional grain boundary structure, inclination angle of the grain boundary plane is a factor directly involved in the IGSCC. Zhang et al. investigated the crack initiation susceptibility of IGSCC for 316 stainless steels[54]. As the result, they reported that the susceptibility to cracking increased when the angle of α, indicating the angle between the grain boundary plane normal and the stress axis decreased. As the angle of α decrease, the grain boundary plane becomes structurally perpendicular to the stress axis. Therefore, the crack susceptibility increases because the induced vertical stress acting on the grain boundary plane can be increased.

Zadow et al. reported that deep cracks were observed at inclination angles between 37 ˚ and 52 ˚, and most of the cracks were between 21 ˚ and 45 ˚[55]. Moreover, they found the crack tends to deepen when inclination angles increased. These documents show that the crack susceptibility on the grain boundary plane depends on the geometrical structure of the grain boundary. Considering the three-dimensional structure of the grain boundary plane in this study, it is necessary to compare it with the study of crack propagation. Pan et al. examined the crack susceptibility according to the grain boundary orientation, which creates the macroscopic direction of crack propagation[56]. As a result, it found that most of the crack planes showing the angle relative to crack propagation direction of cracked grain boundaries were smaller than 60 ˚. Thus, they reported that the high angle grain boundaries within 60 ˚ are susceptible to IGSCC.

Even grain boundaries having the same misorientation angles, it may have different grain boundary energy depending on the orientation of the grain boundary plane[57, 58]. Therefore, it is necessary to consider the grain boundary energy with respect to the grain boundary plane. Bulatov et al. reported that the highest grain boundary energy was observed around the boundary plane relative to the rotation of about 40 ˚[59]. In **Fig. 4-8** of this chapter, the faster crack propagation around 40 ˚ of inclination angle of grain boundary

plane for both 10% CW and 20% CW specimens is expected to be cause highest relative boundary plane energy. Based on the literature, it is clear that the IGSCC considering the grain boundary plane is caused by the geometrical structure of boundary plane and the energy of grain boundary plane according to the inclination angle.

4.5 Conclusion

Intergranular stress corrosion cracking of Alloy 600 was crystallographically examined by electron backscatter diffraction. A slow strain rate test (SSRT) was conducted for cold-worked tensile specimens of Alloy 600 in different environments with different dissolved hydrogen concentrations at different temperatures of 593 K or 633 K. Although SSRT was terminated at 10% of tensile strain, cracks initiated under all conditions examined, but cracks were less and shorter at 593 K compared to those at 633 K. Cracks on specimens subjected to the cold work with the reduction of either 10 % or 20 % were statistically characterized. EBSD was conducted at several locations on the cutting edges of gauge sections in cross-sectional as well as top-views. Results indicated that the probability of the crack initiation was higher at the misorientation angle of 30 º ~ 40 º. Furthermore, the inclination angle of grain boundary plane was examined by using crystallographic information and angles between the direction of the applied stress and a crack line observed at the surface and the cross-section. The higher crack susceptibility revealed at inclination angle of around 40 ˚ on cracked grain boundary plane in both 10 % and 20 % cold-worked specimens.

References

1) H. Coriou, L. Grall, Y.S. Vettier, Colloque de Metallurgie Corrosion, Centre d'Etudes Nucleaires de Saclay, North Holland Publishing Co., Amsterdam, Holland, 161 (1959).
2) H. Coriou, L. Grall, C. Mahieu, M. Pelas, Corrosion. 22 (1966) 280–290.
3) F. Scenini, R.C. Newman, R.A. Cottis, R.J. Jacko, Corrosion. 64 (2008) 824–835.
4) M. Sennour, P. Laghoutaris, C. Guerre, R. Molins, Nucl. Mater. 393 (2009) 254–266.
5) Y.S. Lim, H.P. Kim, S.S. Hwang, J. Nucl. Mater. 440 (2013) 46–54.
6) B. Ter-Ovanessian, J. Deleume, J.M. Cloué, E. Andrieu, Corros. Sci. 67 (2013) 11–19.
7) T. Magnin, D. Noël, R. Rios, Mater. Sci. Eng. A. 177 (1994) 11–14.
8) R.B. Rebak, Z. Szklarska-Smialowska, Corros. Sci. 38 (1996) 971–988.
9) H. Takiguchi, M. Ullberg, S. Uchida, J. Nucl. Sci. Technol. 41 (2004) 601–609.
10) K. Dozaki, D. Akutagawa, N. Nagata, H. Takiguchi, K. Norring, Society. 2 (2010) 65–76.
11) T. Nakagawa, N. Totsuka, T. Terachi, N. Nakajima, J. Nucl. Sci. Technol. 40 (2003) 39–43.
12) W.C. Moshier, C.M. Brown, Corrosion. 56 (2000) 307–320.
13) S. Yamazaki, Z. Lu, Y. Ito, Y. Takeda, T. Shoji, Corros. Sci. 50 (2008) 835–846.
14) J. Hou, Q.J. Peng, Z.P. Lu, T. Shoji, J.Q. Wang, E.H. Han, W. Ke, Corros. Sci. 53 (2011) 1137–1142.
15) D.S. Morton, S.A. Attanasio, E. Richey, G.A. Young, Proceedings of the 12th International Conference on Environmental Degradation of Materials in Nuclear

Power System – Water Reactor – (2005).

16) W.L. Clarke, G.M. Gordon, Corrosion. 29 (1973) 1–12.

17) S.M. Bruemmer, L.A. Charlot, C.H. Henager, Corrosion. 44 (1988) 782–788.

18) S.M. Bruemmer, G.S. Was, J. Nucl. Mater. 216 (1994) 348–363.

19) J. Panter, B. Viguier, J.M. Cloué, M. Foucault, P. Combrade, E.J. Andrieu, Nucl. Mater. 348 (2006) 213–221.

20) B. Alexandreanu, B. Capell, G.S. Was, Mater. Sci. Eng. A. 300 (2001) 94–104.

21) H.S. Chih, P.G. Shewmon, Metall. Trans. A (Physical Metall. Mater. Sci. 21A (1990) 1261–1272.

22) S. Lozano-Perez, J.M. Titchmarsh, Mater. High Temp. 20 (2003) 573–579.

23) N. Totsuka, E. Lunarska, G. Cragnolino, Natl. Assoc. Corros. Eng. 43 (1987) 505–514.

24) J.H. Suh, J.K. Shin, S.J.L. Kang, Y.S. Lim, I.H. Kuk, J.S. Kim, Mater. Sci. Eng. 254 (1998) 67–75.

25) Y. Yi, S. Eom, H. Kim, J. Kim, J. Nucl. Mater. 347 (2005) 151–160.

26) K.T. Aust, U. Erb, G. Palumbo, Mater. Sci. Eng. A. 176 (1994) 329–334.

27) P. Lin, G. Palumbo, U. Erb, K.T. Aust, Scr. Metall. Mater. 33 (1995) 1387–1392.

28) G.S. Was, V. Thaveeprungsriporn, D.C. Crawford, Jom. 50 (1998) 44–49.

29) V.Y. Gertsman, S.M. Bruemmer, Acta Mater. 49 (2001) 1589–1598.

30) K.T. Jung, T. Ogawa, Y. Morita, S. Fujimoto, Proceedings of 17th International Conference on Environmental Degradation of Materials in Nuclear Power Systems – Water Reactor – 2 (2015) 895-903.

31) R.N. Parkins, Jom. 44 (1992) 12–19.

32) T. Shibata, Iron Steel Inst. Japan. 31 (1991) 115–121.

33) H.-J. Bunge, Texture analysis in materials science — 1Ed, Butterworth, London,

(1993).

34) S.I. Baik, M.J. Olszta, S.M. Bruemmer, D.N. Seidman, Scr. Mater. 66 (2012) 809–812.

35) E. Biyikli, D. Canadinc, H.J. Maier, T. Niendorf, S. Top, Mater. Sci. Eng. A 527 (2010) 5604–5612.

36) G. Zhu, W. Mao, Y. Yu, Scr. Mater. 42 (1999) 37–41.

37) V. Randle, J. Microsc. 195 (1999) 226–232.

38) V. Randle, Acta Mater. 52 (2004) 4067–4081.

39) V. Randle, Mater. Charact. 34 (1995) 29–34.

40) K. Sztwiertnia, J. Pospiech, F. Haessner, Textures Microstruct. 12 (2008) 233–242.

41) S. Fujimoto, W.S. Kim, M. Sato, J.Y. Son, M. Machida, K.T. Jung, H. Tsuchiya, J. Solid State Electrochem. 19 (2015) 3521–3531.

42) H.F. Lopez, MRS Proc. 1276 (2010) 1.

43) B. Alexandreanu, G.S. Was, Corrosion. 59 (2003) 705–720.

44) D.J. Paraventi, T.M. Angeliu, G.S. Was, Corrosion. 58 (2002) 675–686.

45) S. Fujimoto, M. Mochizuki, Y. Morita, Y. Mikami, H. Tsuchiya, K. Nishimoto, Proceedings of 15th International Conference on Environmental Degradation of Materials in Nuclear Power Systems – Water Reactor – (2011) 1685-1698.

46) G. Palumbo, P.J. King, K.T. Aust, U. Erb, P.C. Lichtenberger, Scr. Metall. Mater. 25 (1991) 1775–1780.

47) J.Q. Chen, H. Lu, W. Cui, J.M. Chen, Y.F. Huang, Mater. Sci. Technol. 30 (2014) 1189–1196.

48) T. Tsuchiyama, M. Natori, N. Nakada, S. Takaki, ISIJ Int. 50 (2010) 771–773.

49) R. Viswanathan, C.L. Bauer, Acta Metall. 21 (1973) 1099–1109.

50) P.A. Beck, P.R. Sperry, H. Hu, J. Appl. Phys. 21 (1950) 420–425.

51) D.B. Titorov, Phys. Met. Metallogr. 36 (1973) 82–87.

52) A. Stratulat, J.A. Duff, T.J. Marrow, Corros. Sci. 85 (2014) 428–435.

53) A.P. Jivkov, N.P.C. Stevens, T.J. Marrow, Comput. Mater. Sci. 38 (2006) 442–453.

54) S. Yamazaki, Z. Lu, Y. Ito, Y. Takeda, T. Shoji, Corros. Sci. 50 (2008) 835–846.

55) L. Zadow, E. Gamboa, O. Lavigne, Materials and Corrosion. 66 (2015) 1092–1100.

56) Y. Pan, B.L. Adams, T. Olson, N. Panayotou, Acta Mater. 44 (1996) 4685–4695.

57) G.S. Rohrer, E.A. Holm, A.D. Rollett, S.M. Foiles, J. Li, D.L. Olmsted, Acta Mater. 58 (2010) 5063–5069.

58) D.L. Olmsted, S.M. Foiles, E.A. Holm, Acta Mater. 57 (2009) 3694–3703.

59) V.V. Bulatov, B.W. Reed, M. Kumar, Acta Mater. 65 (2014) 161–175.

Chapter 5 General conclusions

In the present study, the author investigated the effect of three-dimensional crystallographic characterization on initial stage of IGSCC of Alloy 600 under high temperature and high pressure water environment using EBSD. As a result, the following conclusions have been derived.

Chapter 1

The author has introduced the overview on IGSCC, the main mechanisms of IGSCC that has been proposed so far, various factors, particularly focusing on the grain boundary characteristics such as the grain boundary types, misorientaiton angle and the importance of statistical analysis for the crystallographic characterization on grain boundary, followed by the purpose of the present thesis.

Chapter 2

Chapter 2 has shown methodology to examine the direction of crack initiation towards Alloy 600 specimen with EBSD and examined crystallographically IGSCC cracks. SSRT revealed that IGSCC cracks initiated for the first time on a flat tensile specimen of Alloy 600 that was subjected to cold work with the reduction ratio of 10% in a quite short time of the test. This was attributed to the surface asperity induced by mechano-chemical polishing with colloidal silica suspension. After the SSRTs, the specimen surfaces were covered with thick oxide films, which prevented the crystallographic characterization of IGSCC cracks with EBSD. The sputtering of thick oxide films allowed the characterization of cracks with EBSD, thereby providing important information on IGSCC. Furthermore, an approach for three-dimensional characterization of crack initiation based on EBSD was discussed.

Chapter 3

Chapter 3 has reports the crystallographic characterization of crack initiation on grain boundaries of cold-worked Alloy 600 specimens during the slow strain rate test in simulated PWR primary water environments. Many cracks initiated on the Alloy 600 specimens under the high dissolved hydrogen concentration of 2.75 ppm in the environment while initiated cracks were relatively few on the specimens under the low dissolved hydrogen concentration of 0.5 ppm. Cracks were characterized by electron backscatter diffraction (EBSD), revealing that the cracks initiated along grain boundaries. EBSD indicated that the crack susceptibility was strongly affected by the type of grain boundary such as random boundary and coincidence site lattice boundary as well as the misorientation on the boundaries. Furthermore, the crack initiation was investigated in terms of stress loaded on grain boundaries during the slow strain rate test.

Chapter 4

In the chapter 4, crystallographic characterization of crack initiated on cold-worked Alloy 600 in simulated primary water environments of pressurized water reactor was carried out by electron backscatter diffraction (EBSD). EBSD measurements of grain boundaries revealed that the crack initiation was strongly affected by the misorientation angle between adjacent two grains. Furthermore, the crack initiation was examined by the inclination of adjacent grains on the grain boundary plane. The inclination angle was computed from crystallographic data obtained by EBSD and angles between the direction of stress applied to the cold-worked Alloy 600 specimens and the direction of grain boundaries. Cracks on 10% cold-worked specimen initiated more at the specific inclination angle range. On the other hand, cracks on 20% cold-worked specimen were widely

distributed in the inclination angle range from 5 ˚ to 85 ˚. In addition to the misorientation angle and the inclination angle, the direction of stress against grain boundary also affected the crack initiation.

Additionally, the author of the thesis hopes that the knowledge on the effect of grain boundary characteristics on IGSCC initiation obtained in the present study will be useful as a guidance for improving IGSCC resistance of Alloy 600 in PWR primary water environments.

List of Publications

Publications related to this thesis

1. Ki-taek Jung, Takashi Ogawa, Yuya Morita, Shinji Fujimoto.
   "Grain boundary characterization for initial stage of IGSCC of Alloy 600 in PWR primary water environment"
   Proceedings of 17th International Conference on Environmental Degradation of Materials in Nuclear Power Systems – Water Reactor – 2 (2015) 895-903.

2. Ki-taek Jung, Hiroaki Tsuchiya, Shinji Fujimoto.
   "Mechano-chemical polishing of Alloy 600 for accelerated crack initiation in simulated PWR primary water environment and three-dimensional crystallographic characterization"
   Materials Transactions, Vol. 61 [7], p.1339-1345 (2020).

3. Ki-taek Jung, Hiroaki Tsuchiya, Shinji Fujimoto.
   "Micro-crystallographical Characterization of Initiation of Intergranular Stress Corrosion Cracking on Alloy 600 in Terms of Misorientation Angle and Grain Boundary Stress Induced by Slip Deformation"
   Corrosion, Vol. 78, [11], p. 1058-1066 (2022). https://doi.org/10.5006/3923

Other Publications

1. Shinji Fujimoto, Whee-sung Kim, Masugu Sato, Jin-young Son, Masatake Machida, Ki-taek Jung, Hiroaki Tsuchiya.
   Characterization of oxide films formed on Alloy 600 and Alloy 690 in simulated PWR primary water by using hard X-ray photoelectron spectroscopy
   Journal of Solid State Electrochemistry, 19.12 (2015) 3521-3531.

2. Whee-sung Kim, Hiroaki Tsuchiya, Masugu Sato, Jin-young Son, Masatake Machida, Ki-taek Jung, Shinji Fujimoto.
   Electrochemical properties of oxide films formed on cold worked alloy600 and alloy690 in simulated PWR primary water environments
   Zairyo to Kankyo / Corrosion Engineering, 64.11 (2015) 501-507.

3. Ki-taek Jung, Gyu-bong Cho, Ki-won Kim, Tae-hyun Nam, Hyo-min Jeong, Sun-chul Huh, Han-shik Chung, Jung-pil Noh.
   Influence of the substrate texture on the structural and electrochemical properties of sputtered $LiCoO_2$ thin films
   Thin Solid Films, 546 (2013) 414-417.

4. Jung-pil Noh, Ki-taek Jung, Tae-hoon Kwon, Gyu-bong Cho, Sun-chul Huh, Byeong-keun Choi, Ki-won Kim, Tae-hyun Nam.
   Microstructure and electrochemical properties of magnetron-sputtered $LiCoO_2$/$LiNiO_2$ multi-layer thin film electrode
   Materials Research Bulletin, 48 (2013) 4993-4996.

5. Jung-pil Noh, Ki-taek Jung, Min-sun Jang, Tae-hoon Kwon, Gyu-bong Cho, Ki-won Kim, Tae-hyun Nam.
   Protection effect of ZrO_2 coating layer on $LiCoO_2$ thin film fabricated by DC magnetron sputtering
   Nanoscience and Nanotechnology, 13 (2013) 7152-7154.

6. Jae-hyun Kim, Ki-taek Jung, Jung-pil Noh, Gyu-bong Cho, Shuichi Miyazaki, Tae-hyun Nam.
   Martensitic transformation behavior of Ti–Ni–Sn alloys
   Alloys and Compounds, 577S (2013) S200-S204.

7. Jung-pil Noh, Ki-taek Jung, Gyu-bong Cho, Sang-hun Lee, Ki-won Kim, Tae-hyun Nam.
   The Effects of substrate and annealing on structural and electrochemical properties in $LiCoO_2$ thin films prepared by DC magnetron sputtering
   Nanoscience and Nanotechnology, 12 (2012) 5937-5941.

8. Jung-pil Noh, Gyu-bong Cho, Ki-taek Jung, Won-gyeong Kang, Chung-wan Ha, Hyo-jun Ahn, Jou-hyeon Ahn, Tae-hyun Nam, Ki-won Kim.
   Fabrication of $LiCoO_2$ thin film cathodes by DC magnetron sputtering method
   Materials Research Bulletin, 47 (2012) 2823-2826.

9. Gyu-bong Cho, Si-young Choi, Jung-pil Noh, Ki-taek Jung, Tae-hyun Nam.
   Dependence of milling time on electrochemical properties of aano Si electrodes prepared by ball-milling
   Nanoscience and Nanotechnology, 11 (2011) 6262-6265.

Presentations

International conferences

1. Ki-taek Jung, Takashi Ogawa, Yuya Morita, Shinji Fujimoto.
   Grain boundary characterization for initial stage of IGSCC of Alloy600 in PWR primary water environment
   17th International Conference on Environmental Degradation of Materials in Nuclear Power Systems – Water Reactors, Ottawa, Canada, August, 2015.

2. Ki-taek Jung, Hiroaki Tsuchiya, Shinji Fujimoto.
   Crystallographic analysis for intergranular stress corrosion cracking of Alloy600 in Simulated PWR Environment
   Gordon Research Seminar / Conferences – Corrosion Aqueous, New Hampshire, USA, July, 2016.

Acknowledgements

The author would like to express his grateful gratitude to ***Prof. Shinji Fujimoto*** of The Division of Material and Manufacturing Science, Osaka University, for his kind guidance, helpful suggestions, constructive discussion and invaluable encouragements throughout this work and then offering constant assistance during the doctor's course in Osaka University.

The author is greatly indebted to ***Prof. Hiroshi Utsunomiya***, ***Prof. Hiroyuki Yasuda*** and ***Prof. Yuichiro Koizumi*** of The Division of Material and Manufacturing Science, Osaka University, for reviewing this thesis and their valuable comments.

The author is very grateful to ***Associate Prof. Hiroaki Tsuchiya*** of The Division of Material and Manufacturing Science, Osaka University, for his helpful suggestion, discussion and guidance throughout this work.

The author is very grateful to ***Mr. Junji Nakata*** of Osaka University for the technical assistance and also for his kind help and constructive comments. The author also would like to thank all members of Prof. Fujimoto's Group for their helpful suggestions and collaborations during my study in Japan.

The author would like to take this opportunity to thank ***Prof. Tae-Hyun Nam*** at Gyeongsang National University for his hearty encouragement and helps. Furthermore, the author thanks the members in the Prof. Nam's Group for their friendships, encouragement and helps.

Finally, the author would like to thank family members including ***Jae-Jun Park*** in Japan and loved ones for their patience and advice. And his wife ***Min-Jeong Lee*** and lovely daughter ***Yi-Seo Jung*** has assisted the author in innumerable ways, whatever the author might say here cannot do full justice to the extent and the value of her contribution. The period during the study in Japan, will remain associated with the birth of adorable niephlings, ***Ha-Yoon*** *and* ***Chan-Hui***. The author has dedicated this dissertation to them.

Ki-Taek Jung

September 2022